VICTOR CUPOLA GANINO

Análise com Velocimetria por Rastreamento de Partículas de Interações Turbulentas em Sprays de Etanol

São Paulo
2023

VICTOR CUPOLA GANINO

Particle Tracking Velocimetry Analysis of Turbulent Interactions on Ethanol Sprays

Versão Corrigida

Dissertation submitted to the Polytechnic School of the University of Sao Paulo for the fulfillment of requirements for the degree of Master of Science

Area of concentration:

Mechanical Engineering of Energy and Fluids

Advisor:

Antonio Luiz Pacifico

São Paulo
2023

Este exemplar foi revisado e corrigido em relação à versão original, sob responsabilidade única do autor e com a anuência de seu orientador.

São Paulo, _____ de _____ de _____

Assinatura do autor: _____

Assinatura do orientador: _____

Catalogação-na-publicação

Dedication

I dedicate this work to God and His son Jesus for His love. To my parents, Luciano and Sandra. To my sister Thamirez. To my daughter Sofia. And my beloved wife Rafaella. You always supported me in my career and allowed me to complete this work.

Give thanks to the Lord, for he is good. His love endures forever. (Psalm 136:1)

ACKNOWLEDGMENTS

I would like to thank everyone who supported me in this achievement. To all that helped me overcome the challenges in this journey. Their support will always be appreciated.

For my advisor Antonio Luiz Pacifico, I would like to thank you for being helpful and dedicated to teaching me, and for all the kind words of encouragement that made me focus on the job. Also, for providing me with all the tools and required knowledge to complete this work.

To my laboratory colleagues and friends that helped with the experimental results. Especially my colleague Rafael Todaro, his help had an impact on the process to complete this work.

To my parents, my sister, and my daughter. They were always by my side at all times, and your kind support was the providing bases for my academic and professional progress. This work and my career would not be able without them.

To my wife Rafaella, my life partner, for the trust in the process and her belief that God guided us into this journey. Also, her faith that each challenge was an opportunity used by Him for my professional growth and demonstration of His miracles.

And most important to God. Without Him, I would not be capable of doing this. He showed me the opportunity and provided everything to complete this work. Faith in You was the only way to complete every task, and I had always learned about faith with You along this journey. I dedicate this work to You, God. I will always be thankful for Your sacrifice on that cross and for saving me from my sins. Your words will always be in my heart, thank you, Lord.

I am the way, and the truth, and the
life. No one comes to the Father
except through me.
(John 14:6)

For God so loved the world, that he
gave his only Son, that whoever
believes in him should not perish but
have eternal life.
(John 3:16)

But the angel said to the women, 'Do
not be afraid, for I know that you seek
Jesus who was crucified. he is not
here, for he has risen, as he said.
Come, see the place where he lay.
(Matthew 28:5-6)

RESUMO

Motores a combustão interna visando sustentabilidade associada a menores consumos de combustível e diminuição de emissão de poluentes são demandas para as próximas gerações de veículos. O combustível etanol é uma boa alternativa para as demandas do mercado interno quando equipado a sistemas de injeção direta de combustível. No desenvolvimento e formação de *sprays*, a dinâmica do ar admitido é fundamental para estabelecer um conhecimento mais sólido para o ambiente da câmara de combustão. Técnicas de medição da velocidade de fluidos são amplamente usados e as técnicas mais confiáveis ultimamente são as medições ópticas não intrusivas, como o PIV (*Particle Image Velocimetry*) e o PTV (*Particle Image Velocimetry*). Apesar da popularidade do PIV, a técnica de PTV está ganhando atenção devido aos novos algorítimos desenvolvidos para lidar com escoamentos com maiores densidade de partículas, visto que suas demandas eram específicas para avaliação de fluxos com menores densidade de partículas. Este trabalho visa em avançar os estudos sobre o campo de velocidades do ar dentro da câmara de combustão no qual foram conduzidos anteriormente para o desenvolvimento de *sprays* de etanol, usando a IESC (*Isothermal Ethanol Spray Chamber*) do laboratório LETE da Universidade de São Paulo, mas com a perspectiva da técnica de PTV. O objetivo foi ampliar a compreensão do comportamento do ar ao redor do desenvolvimento do spray em motores a combustão interna com injeção direta usando os dados experimentais obtidos para a técnica PIV e comparar com a técnica PTV para as mesmas imagens cruas do ar que circunda o *spray*. A medição PIV apresentou muito ruído em áreas de baixa densidade de partículas ou altos gradientes de velocidade. Através de pré-processamento de imagens, foi possível melhorar em 150% as relações com SNR. Os resultados foram agrupados e aplicadas as médias e a média de detecção dos vetores *outliers* foi por volta de 15%. Além disso, analises foram feitas para garantir a qualidade do vetor resultante com uma amplitude de *peak locking* entre 8 a 18% e um histograma de deslocamento sub-pixel aproximadamente plano. O campo vetorial do PTV mostrou boas informações e sua variação da magnitude da velocidade global, $|U|$, variou entre 2 e 15 m/s. As componentes u e v desses vetores foram encontradas e suas comparações com o estágio do desenvolvimento do *spray* e pressões de injeção foram relacionados. A *shear layer* mostrou ser um desafio e sua componente v do ar nos primeiros instantes do *spray* teve um acréscimo de $52, 4\%$. Estruturas de recirculação, arraste do ar para as cavidades do *spray*, e um arraste global atrás do *spray* puderam ser encontrados usando a técnica de PTV. O escoamento bi-fásico mostrou ser desafiador, porém o PTV proveu informações sobre o ar que circunda o desenvolvimento do *spray* em condições experimentais que motores reais operam, exceto para baixas rotações ou condições de altas demandas.

Palavras-Chave – Campo de velocidades, *Spray* de Etanol, Análise Experimental.

ABSTRACT

Sustainable internal combustion engines associated with lower fuel consumption and low levels of pollutants emission are demands for the next generation of vehicles. Ethanol fuel is a good alternative for domestic market demands when equipped with a direct injection system. In the spray development formation, the inlet surrounding air dynamics is fundamental to establishing more robust knowledge in the internal combustion chamber environment. Fluid velocity measurement techniques are widely used, and the most reliable techniques nowadays are the nonintrusive optical measurement, such as PIV (Particle Image Velocimetry) and PTV (Particle Image Velocimetry). Despite PIV popularity, the PTV technique is getting attention with new algorithms developed to handle higher seeded flows, since its demands were specific for the evaluation of sparsely seeded flows. This work aims to advance the studies over air velocity field inside the internal combustion chamber previously carried out by ethanol spray development, using the IESC (Isothermal Ethanol Spray Chamber) from the LETE laboratory of the Polytechnic School of USP, but with the PTV perspective. The objective was to amplify the comprehension of air behavior movement around spray development inside direct injection spark ignition engines using the experimental data done with the PIV technique and compare it with the PTV technique for the same raw images. The PIV measurement showed too much noise in areas of low seeding segments or high-velocity gradients of the flow. Through image pre-processing, it was possible to enhance 150% better relation in SNR. The results were averaged ensembles and the average outliers detection was about 15%. Also, analyses were made to ensure the quality of the resultant flow field with a peak locking range between 8 to 18% and a near-flat histogram of sub-pixel displacement. The PTV vector field showed good information and its range of global velocity magnitude, U_p, varies between 2 to 15 m/s. The u and v components of these vectors were found and their comparison with the spray development stage and injection pressures were related. The shear layer showed to be a challenge, and the v component of the air in the first instants of the spray had an increase of 52.4%. Recirculation structures, air drag into spray cavities, and global drag behind the spray could be found using the PTV technique. The two-phase flow proved to be challenging, but the PTV provided information about the surrounding air of the spray development in the experimental conditions where the real engine operates, except for low rotational speed and high load conditions.

Keywords – Velocity field, Ethanol *Spray*, Experimental Analysis.

LIST OF FIGURES

LIST OF TABLES

ACRONYMS

3MA – *Three-Frame Minimum Acceleration*

4MA – *Four-Frame Minimum Acceleration*

ASOI – *After Start of Injection*

BCC – *Binary Cross Correlation*

BDC – *Bottom Dead Centre*

BS – *Bright Spots*

CCD – *Charged Couple Device*

CMOS – *Complementary Metal-Oxide Semicondutor*

CVCC – *Constant Volume Combustion Chamber*

DSR – *Dynamic Spatial Range*

DISI – *Direct Injection Spark Ignition*

DoG – *Difference of Gaussian*

HWA – *Hot-Wire Anemometry*

IC – *Intensity Capping*

IESC – *Isothermal Ethanol Spray Chamber*

LDV – *Laser Doppler Velocimetry*

LoG – *Laplace of Gaussian*

Nd:YAG – *Neodymium-doped Yttrium Aluminium Garnet*

Nd:YLF – *Neodymium-doped Yttrium Lithium Fluoride*

OCDE – *Organization for Economic Cooperation and Development*

PIV – *Particle Image Velocimetry*

PTV – *Particle Tracking velocimetry*

RMS – *Root Mean Square*

ROI – *Region Of Interest*

SMD – *Sauter Mean Diameter*

SNR – *Signal to Noise Ration*

SRW – *Step Response Width*

SSM – *Subtract Sliding Minimum*

TDC – *Top Dead Centre*

TKE – *Turbulent Kinect Energy*

TR-PIV – *Time-Resolved Particle Image Velocimetry*

LIST OF SYMBOLS

We – Weber number [Dimensionless]

ρ – Fluid density [kg/m³]

U – Fluid velocity [m/s]

d_g – Droplet diameter [m]

σ_t – Surface tension [N/m]

σ – Standard deviation []

Re – Reynolds number [Dimensionless]

U_R – Droplet velocity [m/s]

μ_l – Droplet viscosity [Pa.s]

Oh – Ohnesorge number [Dimensionless]

t – Time [s]

U_p – Particle velocity [m/s]

μ_f – Fluid dynamic viscosity [Pa.s]

v_f – Fluid kinematic viscosity [m²/s]

ρ_p – Particle density [kg/m³]

d_p – Particle diameter [m]

t_s – Particle relaxation time [s]

f_c – Frequency response [Hz]

s_k – Stokes number [Dimensionless]

X – Transform coordinate [m]

Y – Transform coordinate [m]

x – *Spatial coordinate [m]*

y – *Spatial coordinate [m]*

Z_o – *Distance from the image to effective center of the lens [m]*

z_o – *Distance from the object to the effective center of the lens [m]*

F_t' – *Filtered image [Dimensionless]*

$N_{i,j}$ – *Neighbors particles [Dimensionless]*

U_0 – *Velocity measured at a specific data point [m/s]*

ε_a – *Adaptative tolerance [Dimensionless]*

xi – *Coordinate vector of the first and second frame particles [m]*

y_i – *Coordinate vector of the first and second frame particles [m]*

R_s – *Maximal possible displacement of the particles [m]*

R_n – *Vicinity Radius [m]*

U_i – *Velocity of each of its neighbours [m/s]*

d – *Median of the distances between each of the neighbours and the data point [m]*

v – *Particle kinematic viscosity [m²/s]*

CONTENTS

1   INTRODUCTION

The Brazilian energy matrix is considered one of the cleanest of the world, most of it is based on hydraulic source or sugar cane. However, the global scenario is different from Brazil. The rest of the countries uses approximately 90% of their energy source from combustion, as shown in Figure 1a.

The goal of reducing gas pollutant emission to preserve the environment made the countries seek for alternative solutions for their dependency of fossil fuels and invest in less pollutant alternatives. However, the combustion source of energy is still growing over the world as shown in Figure 1b. The worry of energy security and climate change implies in a transition from a traditional energy consumption to a low carbon emission (YAN et al., 2017)

This transition from combustion to a less environmentally aggressive source will be slow and progressive because they still have problems related to intermittency in energy capture. They depend directly on climate factors, for example, eolic and solar energy. Although the intermittency issue is getting less important due to improvements in energy storage and conversion.

(a)   (b)
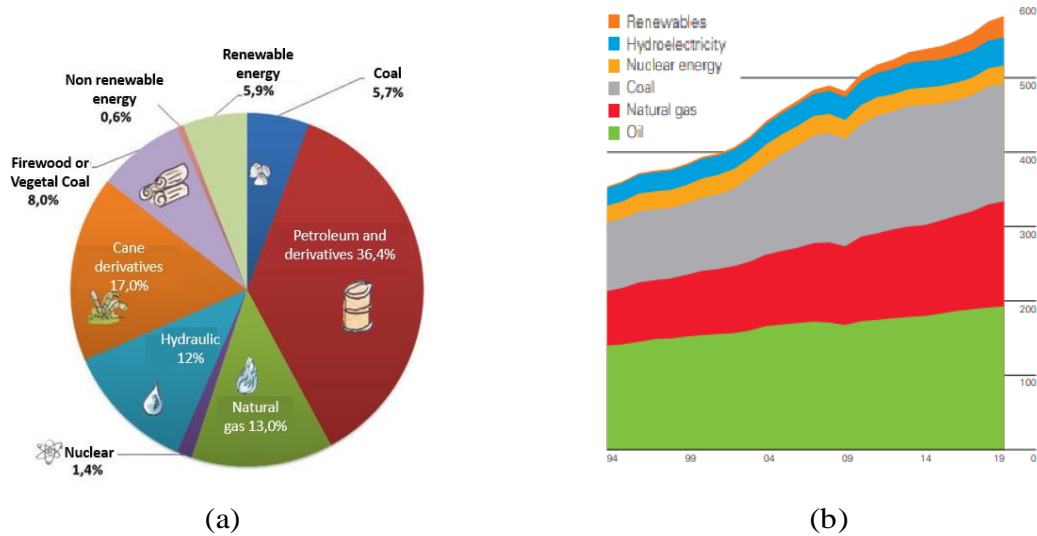
Figure 1: (a)Brazilian energy matrix. Adapted from: epe.gov.br (b) Global energy usage source From: https://www.bp.com/en/global/corporate/energy-economics/statistical-review-of-world-energy.html. Accessed 4 July 2023.

Under this scenario, Brazil has an advantage among other countries, because the National Program of Ethanol Production launched in 1975 (Proálcool) made several encouragements on biofuel consumption aiming to replace on a large scale the dependency on petroleum and its derivatives. It allows the country to have a less abrupt transition of energy that impact the society and the internal market (TEIXEIRA, 2020).

The ethanol usage from flex-fuel technology launched in 2003 allowed automotive consumption of ethanol, which reduced CO_2 emission (SANTOS et al., 2018). To the Brazilian automotive market, an alternative for the next generations is a source of power from electric and ethanol combustion. From this perspective, combustion engines will be on the market for some decades, and a reduction of combustion emissions will be necessary.

Although the effort to solve mobility issues, the Organization for Economic Cooperation and Development (OCDE) shows that individual transport rises over the years. For the next decade, the seek for vehicles tends to grow. In the domestic market, the Brazilian sales of new vehicles is rising over the years, this becomes clear when the number of new registered automobiles, especially with flex-fuel technology, is getting bigger over the years as shown in Figure 2 (ZABEU, 2019).
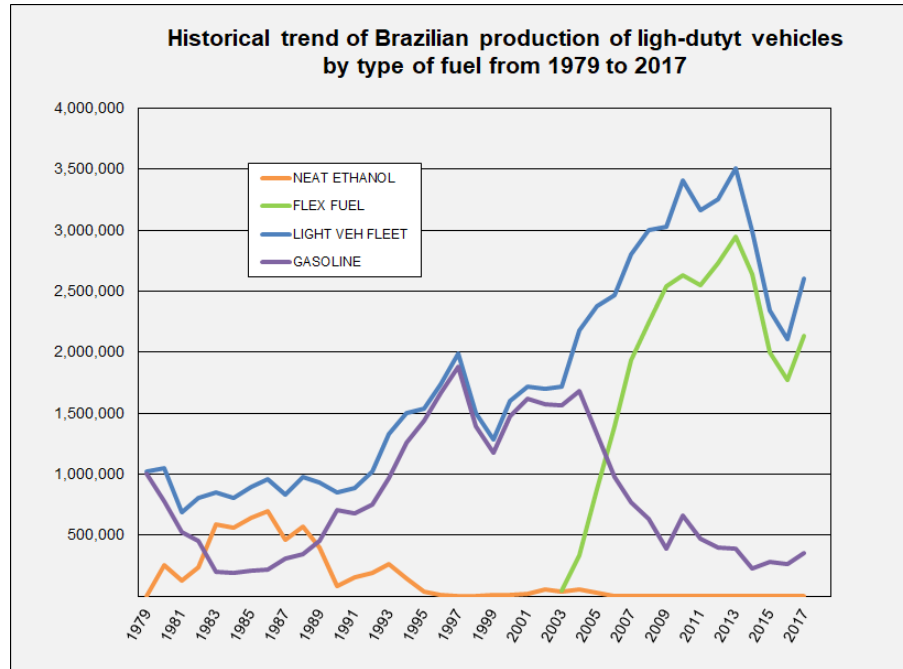
Figure 2: Number of vehicles registered in Brazil. (ANFAVEA, 2018)

Because of this intense usage of ethanol, the need of better knowledge of the qualities and properties of this fuel is necessary. The ethanol fuel has advantages over the gasoline in internal combustion engines as shown (ZABEU, 2019):

- It is a pure component of low molecular mass and shows higher resistance of autoignition on the vapor phase. That allows higher compressure ratio and better engine efficiency;

- It has oxygen on his composition, reducing the non-complete combustion and particle formation;

- Shows higher work efficiency on the expansion;

- Autoignition reduction as consequence of lower temperature at the end of the compression stroke caused by vaporization of the fluid as latent heat transfer;

- Higher combustion velocity in the laminar regime, turning the effect closer to heat exchange with constant volume, making the efficiency higher;

These characteristics make ethanol a good candidate for the next generation of fuel propellants. Their properties, as shown before, have interesting effects on internal combustion engines. Additionally, the bioethanol, which has garnered considerable attention, can be applied without modifying conventional internal combustion engines (KIM et al.,

2022).The Kyoto Protocol effectiveness was limited, and the Paris Agreement was adopted at the United Nations Climate Change Conference in 2015 to correct the problems of the Kyoto Protocol.

For fulfilling the next generation of emission reduction requirements, an internal combustion engine strongly depends on the mixture formation and on combustion process. The usage of direct injection on spark engines plays an essential role for optimization of fuel injection systems, but it depends on knowledge about injection process, spray development and flammable mixture formation. Additionally, the mechanism responsible for spray droplet formation and his interaction with air motion inside the cylinder is an important parameter to design new systems (BERTI, 2018).

The study of spray development is an interaction between spray droplets and the surrounding air, which it is a common interaction in a direct injection spark ignition engines. The progression in this field of fluid dynamics increase the knowledge on two phase flow and their turbulence interactions.

Historically, fluid flow field visualization was the primary technique to get information about fluid behavior. Ludwig Prandtl observed flow separation over an airfoil and other two-dimensional bodies using floating mica particles in a water tunnel, as shown in Figure 3.
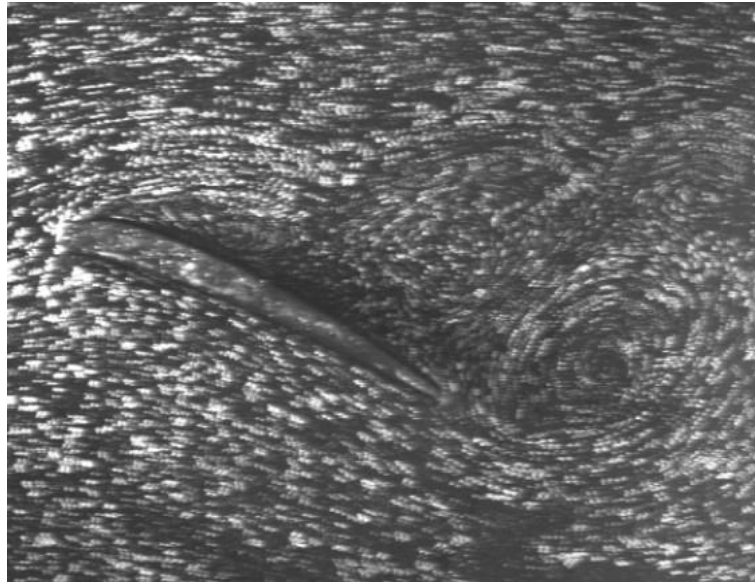
Figure 3: Replica of Ludwing Prandtl experiment visualized with modern equipment (RAFFEL et al., 2007).

Fage and Townend manually measured a sequence of photographs of the fluid flow to quantify the fluid flow movement. The laser speckle photography (LSP) methodologies

introduced laser usage for fluid flow visualization, where the flow was heavily seeded with reflective particles. Individual particles could not be distinguished, but they were able to quantify the kinematic flow field. Recently, the reduction of particle densities allowed particle movement identification with a sequence of images (DABIRI; PECORA, 2019). Individual identification introduced the PTV technique and the PIV technique, where the PTV became prevalent when automatic particle tracking algorithms were first introduced in 1988. The PIV became popular in the fluid flow experiments in the '90s, especially for turbulent fluid flow environments, and shows effectiveness in experimental results. The number of the papers using PIV technique between 1982 and 2008 is shown in the Figure 4. The PIV was used to replace the Hot-Wire Anemometry (HWA) and Laser Doppler Velocimetry (LDV) technique in fluid flow experiments.
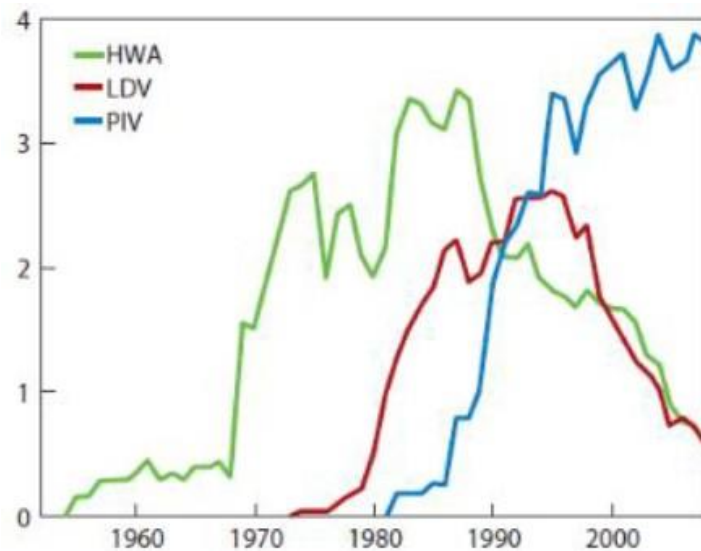
Figure 4: Relative occurrence of fluid flow measurement techniques on turbulent flows using published papers on Google Books platform between the years of 1982 and 2008 (WESTERWEEL et al., 2013).

The PIV technique measurement has been studied in the last decade, and the knowledge of this technique has been in continuous progression. On spray analysis, some recent work had been developed, as it is on (BERTI, 2018) (TODARO et al., 2020) (ZHANG et al., 2014) (ZABEU, 2019).

Due to the importance of ethanol as a fuel, the LETE laboratory of the Polytechnic School of the University of São Paulo worked to understand the air behavior of the surrounding air in direct injectors. The work made by (BERTI, 2018) focused on the image acquisition event of the ethanol spray using the Isothermal Ethanol Spray Chamber (IESC). The IESC is a continuous flow chamber that represents the ambient conditions

of the engine, except for low RPM and high capacities demands. The fluid velocity of the surrounding air and the spray was measured, and the acquired images were analyzed by the PIV technique. However, some irregularities were found in the air velocities due to low particle densities. The low particle densities are shown in the Figure 5, where N_{ppp} is a number of particles per pixel.
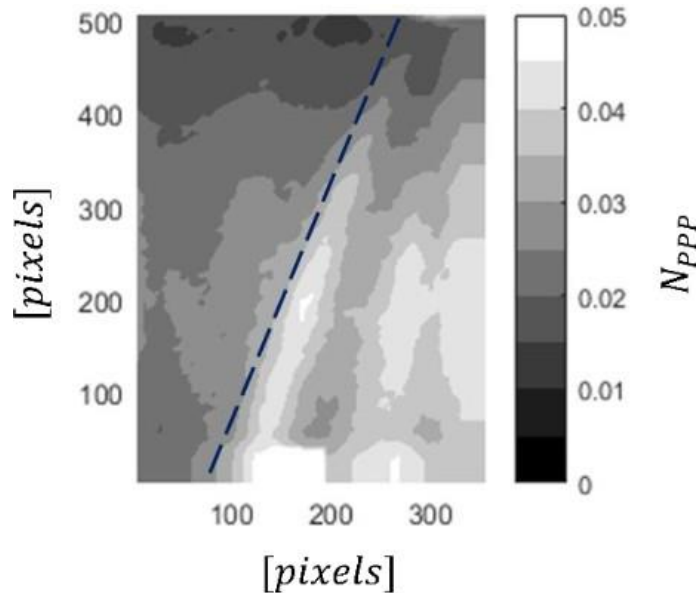
Figure 5: Temporal average of particle concentration per pixel. (TODARO et al., 2020).

As a consequence of the low tracer particle at the airflow and the high image noise from two-phase gas-spray flow, (TODARO et al., 2020) worked to propose a methodology of PIV optimization to present better conclusions between the interaction of the surrounding air and the ethanol spray. The optimization was designed to treat all noise sources presented in PIV images recorded in the IESC to investigate the gas phase flow using the signal-to-noise ratio maximization as objective function. For this purpose, to optimize the effective number of particles, improvements based on good PIV practices were made in the preprocessing, processing and post-processing steps for the air flow (TODARO, 2020).

The effect of noisy sources became larger with the increase of spatial resolution, and an average particle density of 0.025 ppp was observed in the images. The optimization of the Effective Number of Particles, N, defined by Equation 1.1, where N_I is the number of particles sheltered by the interrogation window, F_I and F_O are the factors linked to the correlation losses due to movements inside and outside the light plane, F_Δ refers to the factor that concerns to the influence of particle population motion gradients and F_σ is the term referring to the loss of correlation due to the presence of image noise. (TODARO,

2020). Even with the optimization technique proposed by (TODARO et al., 2020) most of the cases left blank spots compared to the interrogation area because could not achieve a good number of particles densities to this technique, as shown in Figure 6.

$$N = N_I.F_I.F_O.F_\Delta.F_\sigma \qquad (1.1)$$
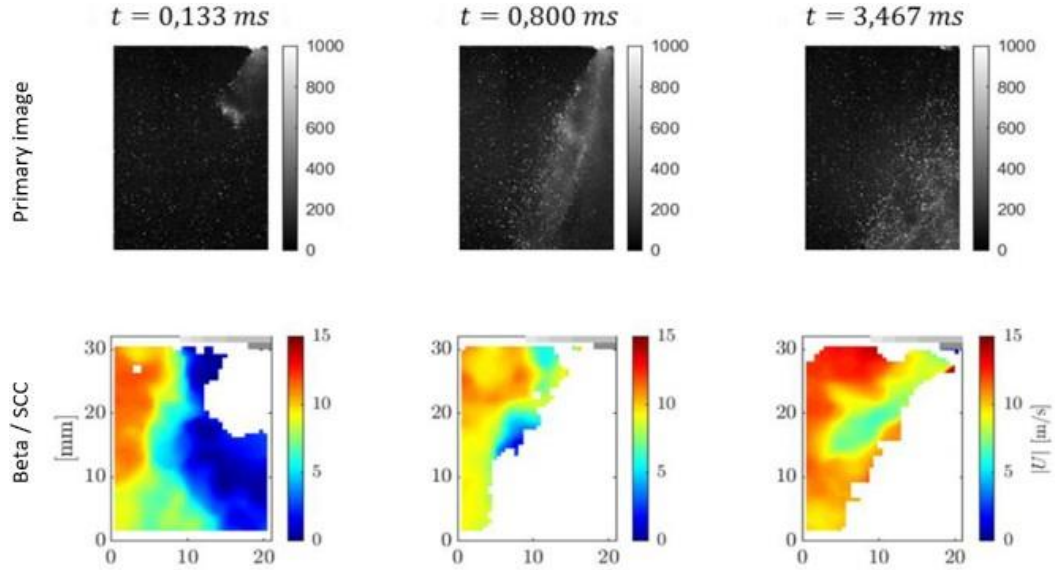
Figure 6: Instant velocity intensity with Beta preprocessing and SCC approach. Adapted from (TODARO et al., 2020).

Two pre-processing techniques were proposed by the work to overcome the issue. The Alpha pre-processing and the Beta pre-processing. The Beta pre-processing presented results of velocity fields with a signal-to-noise ratio (SNR) 150% higher. However, the images presented signal noise associated with low tracers particles during the PIV processing. It showed that the surrounding air fluid flow should be analyzed with lower spatial resolutions to achieve good results.

On the other hand, another technique that until recently did not receive too much attention is becoming popular again, which is the Particle Tracking Velocimetry (PTV). This technique of measurement is very similar to the PIV, especially in image acquisition and light scattering technique. Since those works applied PIV analysis on turbulence sprays regarding fossil fuels, it seems to be an opportunity to apply PTV analysis in ethanol sprays, since ethanol has the potential as a sustainable fuel and PTV is a technique not yet developed in our research group at Polytechnic School of the University of São Paulo. Additionally, the PTV technique is used for lower particle densities and, according

to the (JANKE et al., 2020) work, the algorithm used was able to validate at least 90% of all detected particles in a range of $Nppp = 0.025$ to $N_{ppp} = 0.05$. The Figure 7 shows the results of (JANKE et al., 2020) work with a synthetic image evaluation, and it suggests an optimal seeding of $Nppp = 0.025$ to $N_{ppp} = 0.05$ for the parameters used. Since the images used by (BERTI, 2018) work were between those range of particle concentration, as shown in the Figure 5, it seems to be an opportunity to apply the PTV for those recording images.
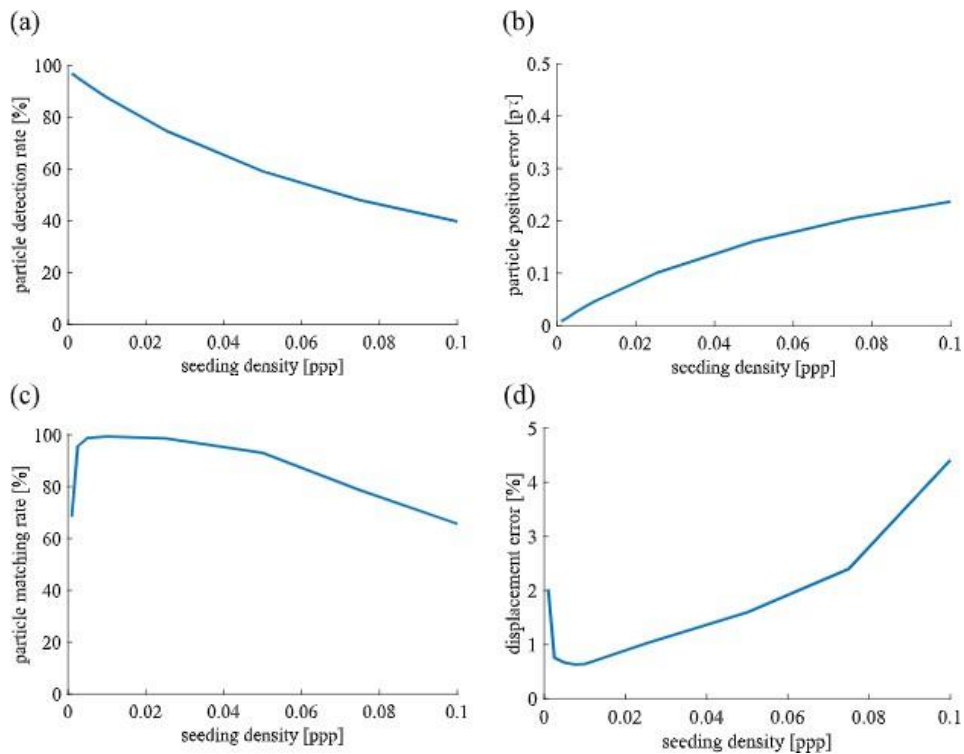
Figure 7: Results of the synthetic image evaluation. a) Particle detection rate. b) Particle position error. c) Particle matching rate. d) Displacement error. (JANKE et al., 2020)

The field of PTV became prevalent when an automatic particle tracking algorithm for low particle densities was introduced. After this, a manual for measurements of particle displacements was founded for PTV. However, modern PTV uses singly-exposed frames with a pulsed laser and matches particle pairs from frame to frame. Recently, the PTV is showing even better spatial resolutions comparable to tomographic PIV for 3D measurements in continuous flows. The technique is known as 'Shake The Box' and it is highly efficient 3D-PTV particle velocity measurement (SCHANZ et al., 2013). It is relevant to highlight that both techniques are important, and they are complementary for the knowledge of a turbulent flow field. It is good to rise the differences between those techniques, but PTV offers the advantage of increased spatial resolution and decrease computational

cost (PECORA, 2018).

As a conclusion of all information proposed previously, the necessity of further information about surrounding air on ethanol spray from Direct Injection engines makes a gap between the interactions analyzed by (TODARO et al., 2020) and (BERTI, 2018). The PTV technique has no direct connection with ethanol spray and could be applied to other fuel flow measurements. However, considering the importance of ethanol fuel for the Brazilian market, it seems to be reasonable to tackle the previous measurements with this technique. Direct injectors and ethanol usage play an important role in the Brazilian market and global industry, especially in CO_2 reduction. Direct Injectors are presented in the downsizing concept used by the automotive market to reduce CO_2 emission, so the next generation of engines are mostly equipped with this technology. Ethanol is one of the most used fuels compared with other energetic alternatives, such as biodiesel. The connection of those works and the necessity to measure surrounding air velocity with low particle densities conducts PTV analysis on the data obtained by (BERTI, 2018) and comparison on implementations as PIV analysis. The present work conducts a further analysis of those previous works under the optics of PTV analysis. And it has the objective to amplify the knowledge using this technique in the continuous phase of the flow (air).

2 OBJECTIVES

The objective of the present work is to amplify the comprehension of air behavior movement around spray development inside direct injection spark ignition engines. The constant flow chamber used in the present work represents most of the spray conditions, except for lower rotations per minute and high demands on power. Consequently, to apply the particle tracking velocimetry technique to the previous air flow image acquisition of (BERTI, 2018), in order to seek better information in addition to those found by (TODARO et al., 2020). Those works found problems in processing images using PIV because they were considered low particle densities for this technique ($N_{ppp} = 0.05$ average). However, the particle density presented in Figure 5 was appropriate for the PTV technique.

Even though the PTV works better with those particle densities, it was relevant to select images that could be used with PTV. The droplets scatter too much light, and with higher pressure the spray becomes a mass of light impossible to select a single particle to measure.

The secondary objective is to study the air velocity field obtained with PTV and their relations with spray development. The images of the velocity field found by (TODARO et al., 2020) will provide a source of comparison between the PTV and PIV analysis of the spray. A sequence of different time intervals would be able to relate the obtained velocity flow field.

3 LITERATURE REVIEW

The literature review of the present work has the objective to highlight the main knowledge that involve spray droplet formation associated with PTV measurement techniques. Also, to emphasize the improving needs for the topic and to summarize a background needed to discuss the topics and evolutions of the work.

3.1 Direct Injection on spark ignition engines

The direct injection system was first used on Diesel engines for a high-pressure ignition mechanism. However, direct injection is being used in Otto engines to reduce consumption and emissions, especially by the downsizing and turbocharging concepts (BOSCH, 2013).

Compared to a similar port-fuel-injected gasoline engine, the direct injection can reduce theoretically fuel consumption from 15% to 25% at part load. It offers more advantages compared to port-fuel injection. The main advantage of direct injection is to reduce pumping losses, and part load throttling is eliminated. Another advantage is that the evaporation of fuel inside the cylinder reduces the average temperature of the in-cylinder charge, this effect may increase volumetric efficiency by up to 10%. Moreover, another advantage of a direct injection system is to have precise control of the amount of fuel injected in the engine cycle (BAUMGARTEN, 2006). The drawbacks related to DI are the expensiveness of the system, the elevated working pressure, the complexity involving direct injection, and the pool fire formation.

3.1.1 Injector types for direct injection spark ignition engines

The injectors play an essential role in the injection of the fuel inside the cylinder, because they operate in high pressure environment. Thus, injectors must be capable of delivering sprays with precision regardless of the ambient pressure (BERTI, 2018). Also, they usually operate in a very short time range, which makes the pressure even higher

and a decrease of the size. A schematic diagram of diesel injector is showed in Figure 8.
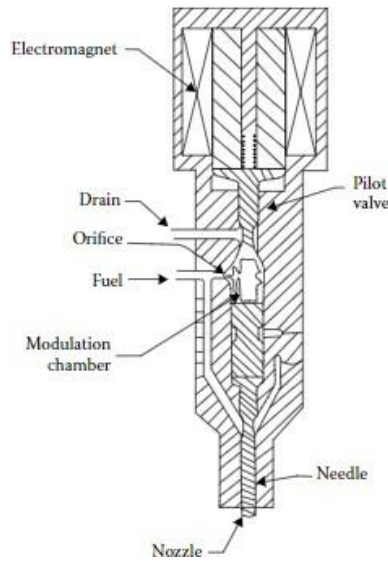
Figure 8: Schematic diagram of electromagnetic diesel injector (LEFEBVRE; MC-DONELL, 2017)

There are several types of atomizers, however, a brief discussion about pressure atomizers is necessary to identify the main characteristics of atomizers, especially on those used in combustion chambers. Generally, atomizers should balance their qualities on the:

- Be able to provide levels of atomization adequate to the specific applications, such as mean droplet diameter in a wide flow rate range;

- Have a fast response to variations of flow rate and do not be associate with bulk flow instabilities;

- Require low power to work;

- Low cost of production and maintenance;

- Have a solid break resistance when produced or in maintenance procedure;

- Low or zero susceptibility to orifice closure caused by contaminants;

- Low or zero susceptibility of gum formation on combustion process (usually diesel engines operating with biodiesel);

- Uniform orifice distribution in the fuel injection.

To go further on atomizers it is necessary to follow a standard classification of the atomization process, these classifications are described by their classes and modes (LIGHTFOOT, 2009). The jets atomizers are divided in *Quiescent environment*, *Coflow*, *Crossflow*, and the ethanol spray is classified as *surface* mode, as showed in Figure 9, where the instability causes are described by *Second wind-induced* mode. The aerodynamic effects are the main factors on the droplet formation and are more relevant than surface tension.
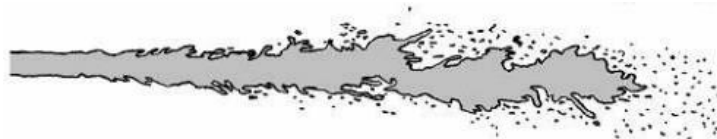
Figure 9: *Second wind-induced* mode (LIGHTFOOT, 2009)

The atomization of a low-viscosity liquid is accomplished by passing it through a small circular hole. The difference of velocities of the ambient fluid and the liquid column makes the instabilities to cause a *break-up* and the droplet formation, the difference of injection pressure can be seen in the Figure 10. Usually when the pressure exceeds the ambient gas pressure by 150 kPa a high-velocity jet is formed and disintegrates into well-atomized spray for low-viscosity liquid (LEFEBVRE; MCDONELL, 2017).
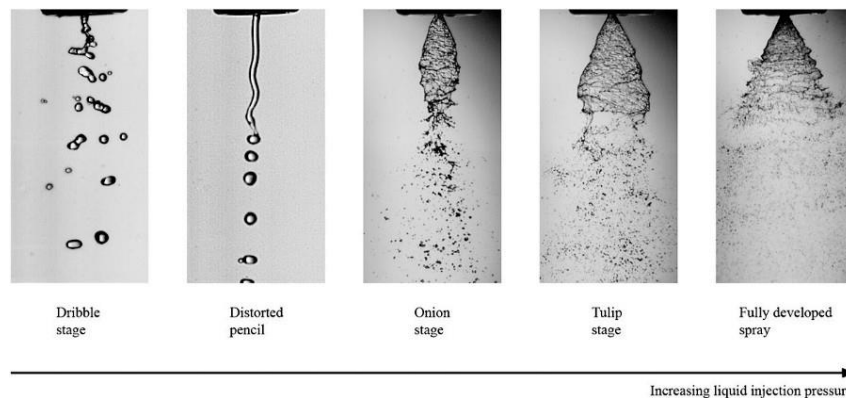
Figure 10: Photographs illustrating spray development in a simplex swirl atomizer (LEFEBVRE; MCDONELL, 2017)

Sprays produce by this type of injector usually lie in a cone angle between 5⁰ and 15⁰, and are slightly affected by the diameter and length-diameter ratio of the orifice and mainly depend on the viscosity and surface tension of the liquid, and a strong dependence on flow turbulence on radial components of velocity, which makes the spray wider. So, the advantage of using this type of injector is that the spray structure and its properties do not change with increasing ambient pressure. An important feature is that these injectors

may modify the spray structure by modifying the quantity and arrangement of the holes in the nozzle (BERTI, 2018). Using this concept to modify spray structure the increase of the number of holes rises the multi-hole injection atomizer, it can be seen in Figure 11 the basic design and the influence of ambient pressure on spray development.
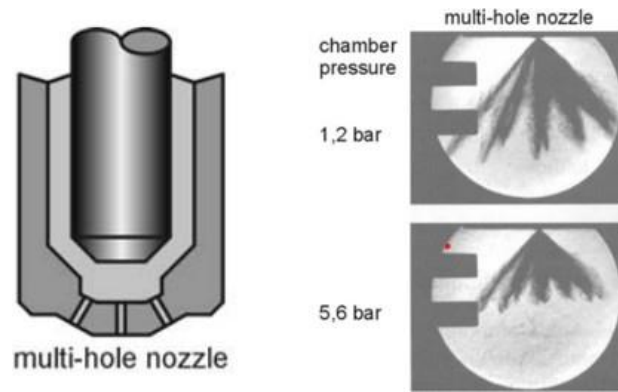
Figure 11: Multi-hole injector design and ambient pressure influence on the spray formation. Adapted from (BAUMGARTEN, 2006).

The simplex atomizers are the other type of atomizers, and they use centrifugal force to produce droplets from *swirl* movement. There are two basic design that are different on the final spray. One of them the spray is distributed equally in a solid cone, and the other concentrate the number of liquid droplets in an outside region, it is a hollow cone format. The difference between them is shown in Figure 12.
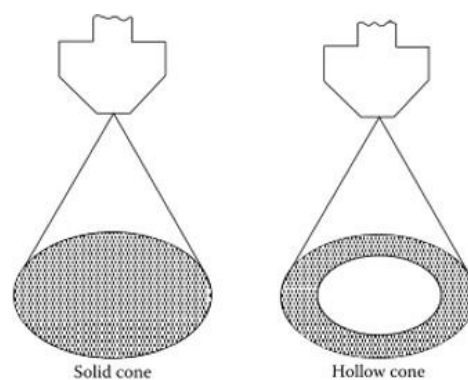
Figure 12: Spray produced by pressure-swirl nozzles. Adapted from (LEFEBVRE; MC-DONELL, 2017).

A great advantage of the hollow cone injectors is the great area-volume ratio, which ensures good atomization at lower penetration lengths. Also, they have a better radial distributions of droplets, which makes a better usage for industrial applications, specially

for combustion. However, the flow rate is a function of the square root of the differential pressure of injection. For the solid cones, it is important to highlight that the principal disadvantage is the coarse atomization in the center of the cone. A schematic view of simplex atomizers and the influence on spray formation of the ambient pressure difference is shown in Figure 13.
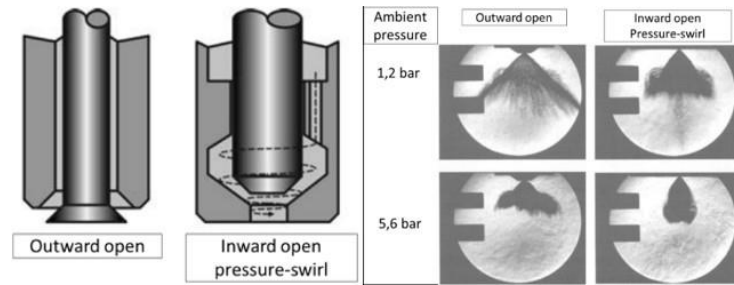
Figure 13: Simplex atomizers and the development of spray on different ambient pressure. Adapted from (BAUMGARTEN, 2006).

3.2   Spray fundamentals

The spray formation is crucial for combustion. The principal parameters are related to the atomizer geometry, the atomized liquid and the environment that surrounds the spray. Laminar jets were studied by (RAYLEIGH, 1879) for droplet formation as consequence of disturbance grow. However, for turbulent cases, which is the most common in practical applications, the radial expansion also contributes with the break-up phenomena. The viscosity of the fluid absorbs and dissipates the energy of the instabilities and mitigates the growing up of the instabilities. This parameter can delay the atomization formation by this effect. So, the atomization formation requires forces that overcome the superficial forces, as surface tension $\sigma_t[N/m\ =\ kg/s^2]$ from spherical form and the viscosity that resist the geometry change, and by that the growing up of the instabilities (LEFEBVRE; MCDONELL, 2017). The Weber number (We) is a very important dimensionless parameter that represents the fluid formation of new surfaces due to inertial forces. It is a ratio of inertial forces and surface tension.

$$We = \frac{\rho.U^2.d_g}{\sigma_t} \tag{3.1}$$

During the spray development, two mechanisms are constantly seen, and they are responsible for the disintegration and subsequent liquid flow break up (BERTI, 2018) (JEDELSKY et al., 2018) (LEFEBVRE; MCDONELL, 2017). The first is called primary

break-up regime, which is responsible for the disintegration of the liquid jet into droplets. The second is called secondary break up, and it is the liquid droplet break up caused by the break-up phenomena of the ligaments resulting from the first regime. The instabilities caused by aerodynamic forces break the droplet even into small droplets. Both are simultaneously seen in the spray formation and related to properties of the fluid and the ambient gas, as showed in the Figure 14.
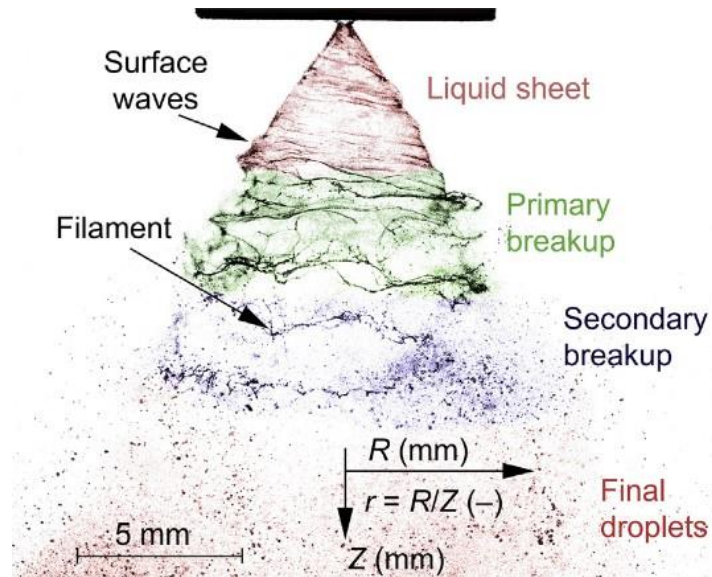
Figure 14: Pressure Swirl atomizer. First and second break-up regimes. (JEDELSKY et al., 2018)

.

The atomization process also depends on Reynolds number, *Re*, and the correlation of Weber number and Reynolds number, which is called Ohnersorge number, *Oh*. These dimensionless numbers are given by:

$$Re = \frac{\rho U_R d_g}{\mu_l} \tag{3.2}$$

$$Oh = \frac{\sqrt{We}}{Re} \tag{3.3}$$

The calculation of these numbers for a multi-component fuel is not trivial, specially at variable temperature/pressure conditions, for constructive analysis (ALEIFERIS et al., 2010).

3.2.1 Liquid jet break up

The Reynolds number and the Ohnersorge number have a relationship that it is possible to define four types of break up mechanisms in the primary regime. They are usually characterized by the break-up length (LIGHTFOOT, 2009) (BERTI, 2018). There are four regimes that can be seen in Figure 15: The Rayleigh regime, the first wind-induced regime, second wind-induced regime and the atomization regime.
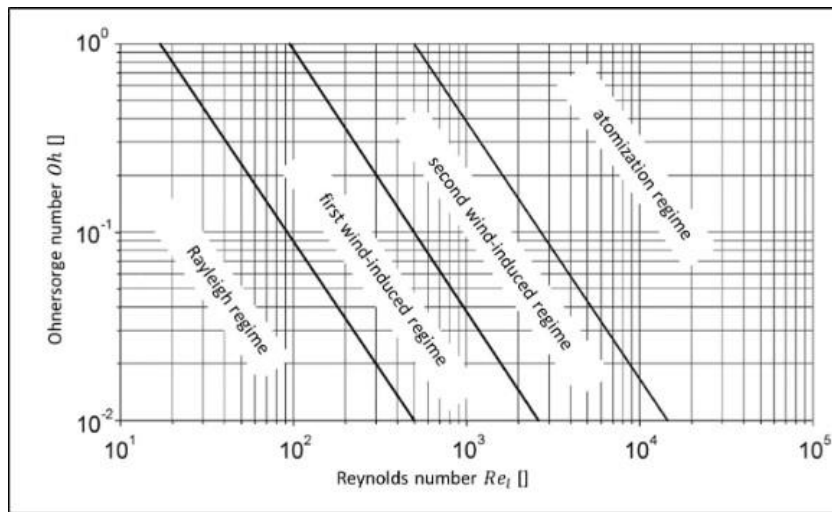
Figure 15: Ohnersorge number for liquid jet break up regimes. Adapted from (BAUM-GARTEN, 2006).

Both Rayleigh mode and the first wind-induced mode are characterized by disturbances on the jet surface that are on the order of the jet diameter. These disturbances grow until the column becomes so narrow that the interface meets, and a droplet is formed. In the Rayleigh regime, the instabilities are purely driven by surface tension forces. Also in the first wind-induced mode aerodynamic effects are important and enhance disturbance growth altering the instabilities (LIGHTFOOT, 2009).

In the second wind-induced regime, the aerodynamic effects dominate over surface tension effects, and numerous small disturbances appear on the surface of the jet. These small disturbances are enhanced due to the relative velocity between the jet and the environment, and break up into small droplets (LIGHTFOOT, 2009).

On the last regime, the jet disintegrates into droplets immediately at exit of the nozzle, with no observable length.

3.2.2   Liquid droplet break up

The droplets formed by the first break-up have aerodynamic effect induced by velocity difference between the droplet and the ambient gas. This effect caused by aerodynamic drag creates instabilities on the surface of the droplet. There is a balance of aerodynamic effect that tries to disintegrate the droplet and surface tension that tries to maintain the droplet as a sphere. A smaller droplet will occur if the velocity increases. Different droplet regimes are identified as shown in Figure 16. With $We < 12$ the droplet formation does not cause disintegration (WIERZBA, 1993).
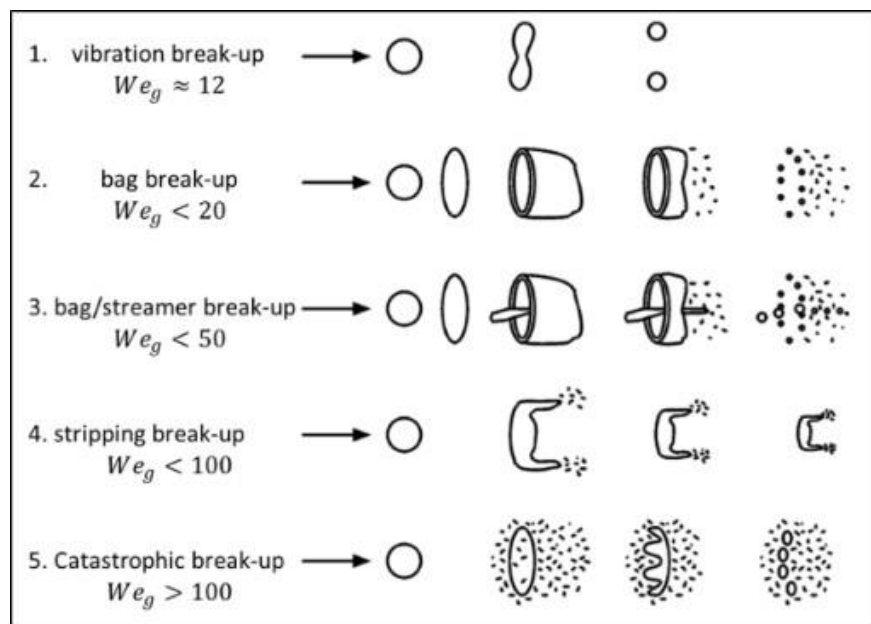
Figure 16: Droplet break up mechanisms. Adapted from (BAUMGARTEN, 2006).

3.2.3   Spray structure - multi-hole injectors

The solid cone spray structure is formed by multi-hole injectors, which has a mechanism of a needle that is opened, and the fluid flows into the holes on the top of the nozzle. In this type of injector each hole is responsible for the formation of one solid cone, the primary break up appears next to the nozzle, and turbulence and cavitation are responsible for collision and coalescence in the center of the spray inside the orifice (TODARO et al., 2020) (LEFEBVRE; MCDONELL, 2017).

The disintegration of the spray begins immediately after the exit from the injection hole. And two break up mechanisms are the most accepted to explain this: turbulence-induced break up and cavitation-induced break up. Both can be seen in the Figure 17,

which is a mechanism of primary break up.
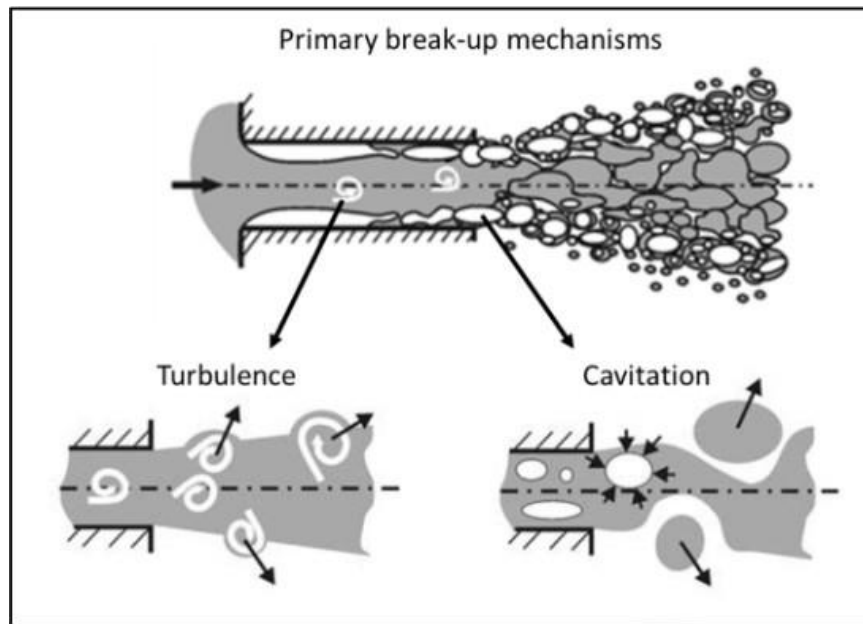
Figure 17: Primary break up mechanisms for multi-hole spray. Adapter from (BAUM-GARTEN, 2006).

The turbulence disintegration mechanism depends on the fluctuation of the radial velocity component. If it overcomes the surface tension, structures are formed by vortices into ligaments and droplets. The turbulence forces within the liquid emerging from the nozzle induces the initial surface perturbations, which grow exponentially due to the aerodynamic forces and are the cause of the formation of new droplets (BAUMGARTEN, 2006) (BERTI, 2018).

On the other hand, the cavitation break up mechanism is formed by the high axial flow velocity, associated with the radial gradient of axial velocity due to the area reduction of the nozzle. This reduction decreases the static pressure of the fluid lower of the vapor pressure at that temperature. When the vapor turns back into liquid the cavitation occurs, and, in association with turbulence, the bubbles can detach and travel with the flow, developing a two-phase flow (BAUMGARTEN, 2006) (BERTI, 2018).

Looking forward to the spray structure, the air-fuel interaction of a direct injection spray is studied by (ZHANG et al., 2014) and it was divided in three regions as shown in Figure 18.
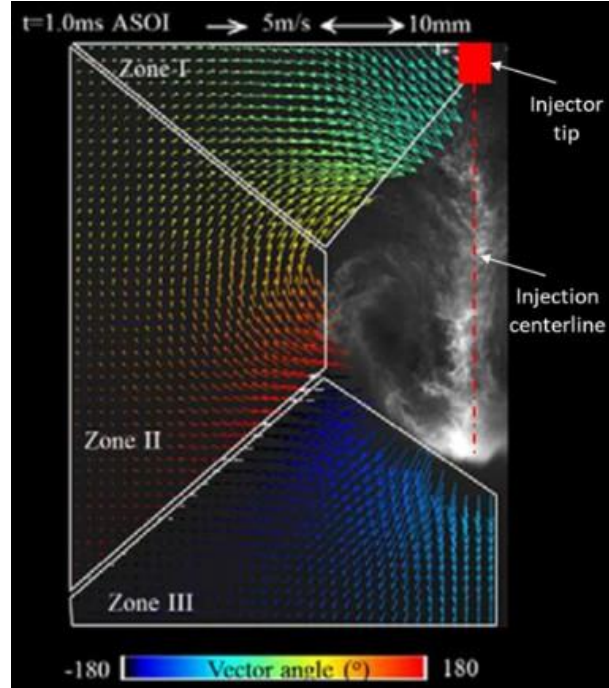
Figure 18: Zones of interaction between spray and ambient air. (ZHANG et al., 2014).

The zone I is called the region of penetration by the air in the lateral surface. The ambient gas is dragged into the spray boundary near the nozzle. The zone II, as intermediate region, is called recirculation region. It is ruled by high recirculation that propagates over the shear layer of the spray as a result of momentum exchange in the zone I. They are intensified over temporal evolution on the shear layer. The zone III, the pulverization region, is the area of mixture between spray droplets and air, where the air is pushed out by the spray. The kinetic energy of the surrounded air increases as a consequence of the momentum transfer of the spray and by the expansion of the interface zone of the two phases. The recirculating structure at the tip of the spray is responsible for the momentum transfer, known as recirculating vortex, which is the momentum transfer over the spray tip and the ambient gas that creates the recirculating structure. The vortex interaction in the structure of the spray cone increases the interaction of the phases. After the injector valve is closed, the kinetic energy still grows because of the recirculating vortex that propagates energy between the spray and air. Also, momentum transfer increases due to the air in zone I being forced into the region behind the spray structure.
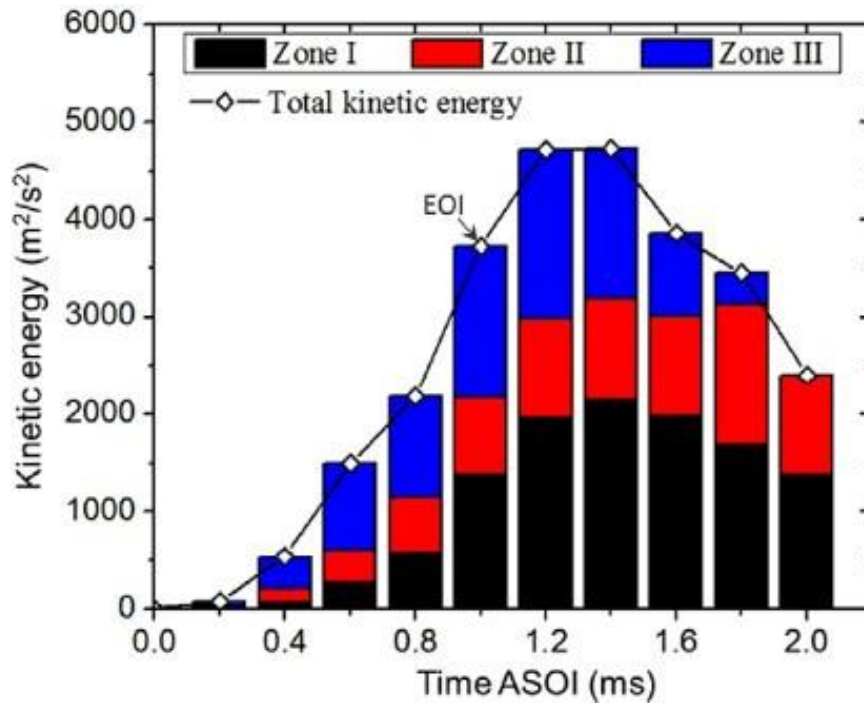
Figure 19: The kinetic energy of the ambient gas surrounding the fuel spray. (ZHANG et al., 2014).

Also, the study of (ZHANG et al., 2014) analyzed that the TKE (*Turbulent Kinetic energy*) in the gas phase grows rapidly by the momentum transfer of the spray to the surrounding air and the progression of the shear layer between the air and spray it can be observed in the Figure 19. The feedback phenomena during the spray development over the recirculation structures influence the momentum transfer, initiating a vortex formation. This happens during the spray propagation.

As concluded by (YEOM, 2008), in the spray structure there exists a large size vortex structure, which is approximately as large as 30% of the length of the spray penetration at the tip region of the evaporative diesel free spray, even though the pressure injection has no effect on the size of the vortex structure.

A comparison between E85 (85% ethanol mixture with 15% gasoline) and gasoline for multi-hole injector in a constant-volume chamber with optical access engine is presented by (ALEIFERIS et al., 2010). The differences between fuel properties can be seen in the Table 1. '

Table 1: Comparison between fuel properties (E85 and gasoline). (ALEIFERIS et al., 2010).

Fuel properties	E85	Gasoline
Density (kg/m^3) (20 °C)	784	735–760
Latent heat (MJ/kg)	0.850	0.34–0.37
Energy density (MJ/kg) (25 °C)	28.94	42–45
Boiling point (°C)	84.8	30–190
Reid vapour pressure (bar)	0.536	0.54–0.6
Research Octane Number (RON)	109.1	95
H:C, O:C	2.657, 0.411	1.86–1.92

The results highlighted the importance of the fuel viscosity on atomization and break-up efficiency. And some discussion is made over the difference between these fuels. The E85 is more insensitive to changes in temperature and pressure, and insensitive to changes in pressures for a determinate temperature. Also, the plumes were thinner and more compact at low temperatures, reflecting in higher spray penetration. Droplet sizes were larger for E85 than gasoline in all conditions. The higher surface tension of ethanol at 20 °C appears to explain this condition. The lower vapor pressure of ethanol indicates in-nozzle cavitation phenomena more severe than gasoline. The *Oh* number for ethanol was more than twice that of gasoline at standard temperature and pressure. However, the combustion performance of E85 at 90 °C was very similar to that of gasoline. For temperatures between 80 to 100 °C, the viscosity of ethanol becomes 40% greater than that of gasoline components. More information between fuels and spray characteristics can be seen in the study of (ALEIFERIS et al., 2010).

3.3 Particle Tracking Velocimetry

The flow visualization is a primary technique used for analyzing turbulence interactions over the years. Advanced techniques developed recently uses flow visualization to understand and measure the flow field. Lately, the most used to characterize fluid flow is the Particle Image Velocimetry (PIV) and Particle Tracking Velocimetry (PTV). The PIV and PTV uses the same experimental procedure, however the PIV uses an interrogation window that sub-samples an image pair, it uses a spatial correlation method resulting in a single velocity vector that represents the average velocity of particles within the interrogation window. On the other hand, the PTV analyzes individual particles to identify the velocity field (DABIRI; PECORA, 2019). An example of 2D layout of the equipment for

applying PIV technique is showed in Figure 20 and compared to the experimental used by (BERTI, 2018) as shown in the Figure 21a and 21b.
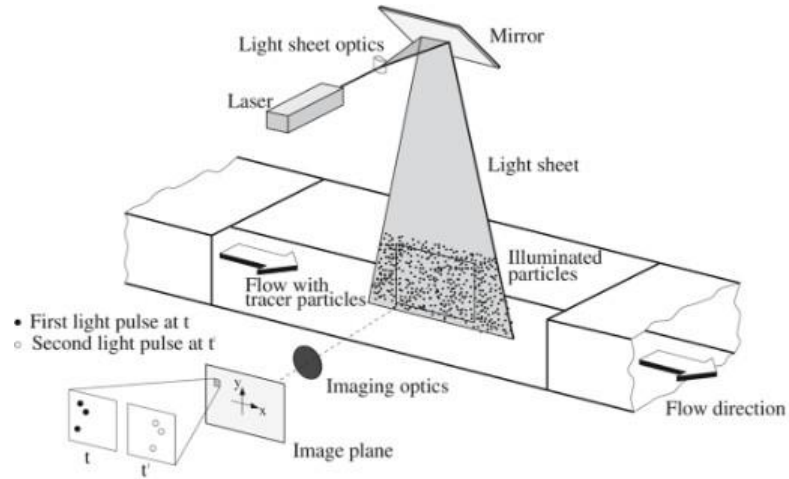
Figure 20: Standard PIV experimental layout. (RAFFEL et al., 2007).
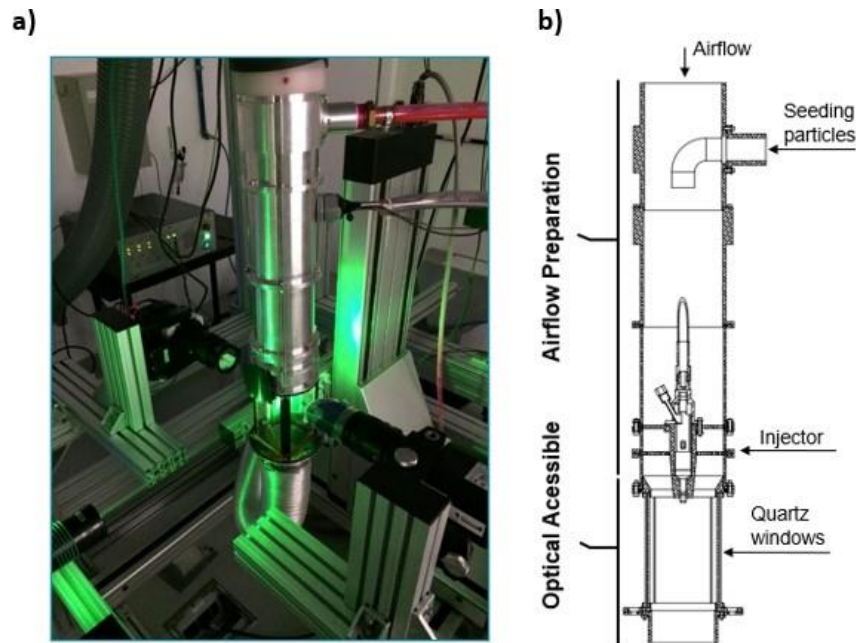
Figure 21: Experimental set-up for two-phase PIV acquisition of (BERTI, 2018).

In both cases, PIV and PTV, the fluid is seeded with particles that act as flow tracers. The particles are immersed in the flow and follow the fluid movement. The technique is an optical visualization technique, which means that the measurement has little influence in the flow. However, an optical access would be necessary to visualize and record the flow. A pulsed light source creates a thin light sheet for 2D and a light volume for 3D. The incidence of light in the particles makes a scattered light that is captured by a

charged couple device (CCD) or a complementary metal-oxide semiconductor (CMOS) video camera positioned perpendicular to the light sheet. The light sheet has a pulsed light with a specific frequency and the camera also have the recording frequencies. The recording device (CCD or CMOS) is synchronized with the pulsed laser to capture the positions of the tracer particles at discrete points in time. An example of an experiment to illustrate the PTV measurement can be seen in Figure 22.
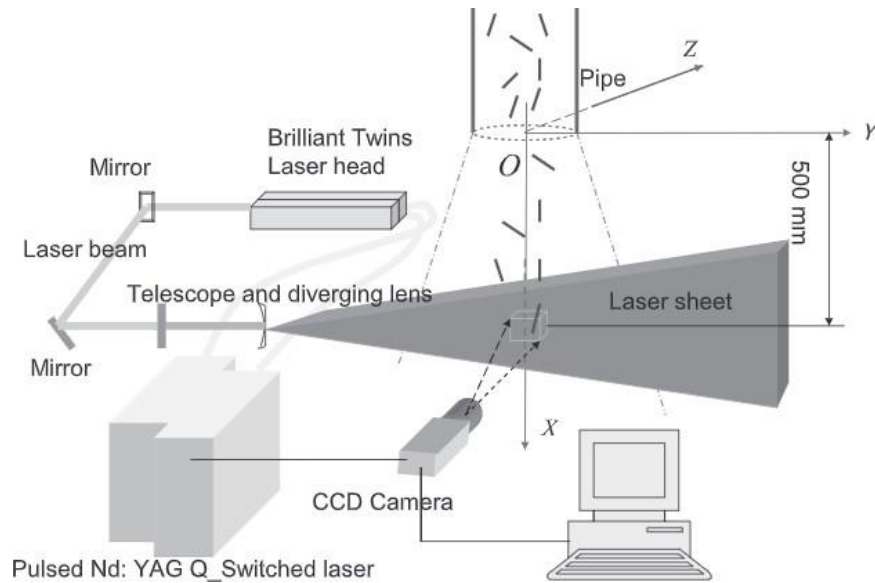
Figure 22: Example of PTV measurement arrangement. (QI et al., 2012).

The displacement and time interval between frames results in the velocity components representing the tracer velocity for PTV or the mean velocity of the group of a particle in that time interval for PIV, as showed in Figure 23a, where ΔS is the displacement between frames and Δt is the time interval. Figure 23b represents the particle location estimation for determination of the velocity using interrogation window for PIV (DABIRI; PECORA, 2019).

(a)　　　　　　　　　　　　　　(b)
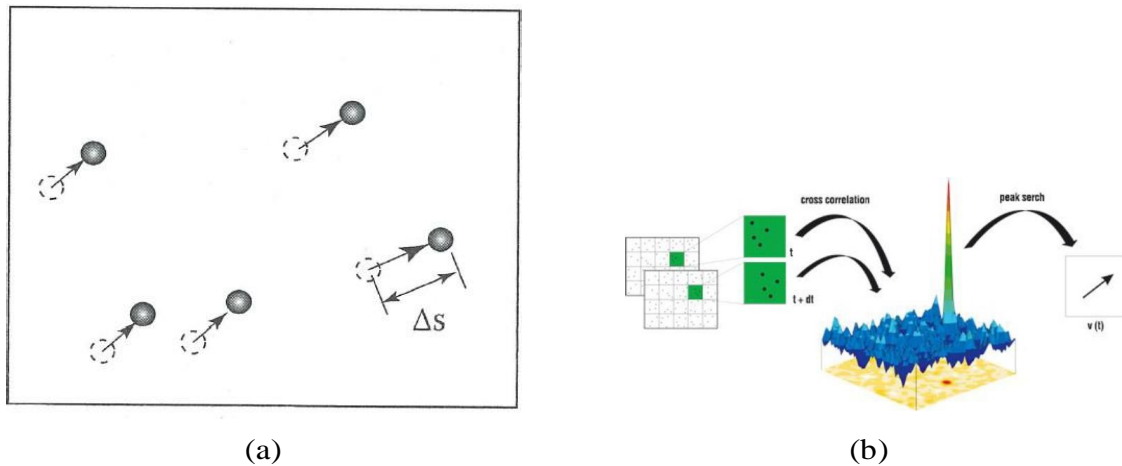
Figure 23: (a) Particle displacement over a Δ*t* time (b) PIV interrogation window for velocity statistical estimation - Dantec Dynamics

Standard CCDs and Nd:YAG lasers have a limited data acquisition to a 30 Hz rate, which is far lower than the frequency at which turbulent flow fluctuations typically occur. But, recent CMOS cameras and Nd:YLF lasers are capable of making measurements up to 400 kHz (BERESH et al., 2017), for Time-Resolved PTV and a small array of only 128 × 120 pixels. In order of magnitude, these frequencies are larger than what hot wires and Laser Doppler Velocimetry (LDV) can provide (DABIRI; PECORA, 2019).

A discussion over the limits of the PIV, especially on the resolution, is a question to be made, and if the PTV supply those limits. A comparison was made by (KAHLER et al., 2012) comparing a 16 × 16 pixel PIV processed windows, single-pixel ensemble-correlations, and PTV, and found that PTV showed a lower magnitude of Step Response Width (SRW) compared to PIV, as shown in the Figure 24. Also, a comparison between the SRW and the particle diameter in the Figure 25 shows that, for PTV, the resolution is independent of the particle image size (KAHLER et al., 2012).
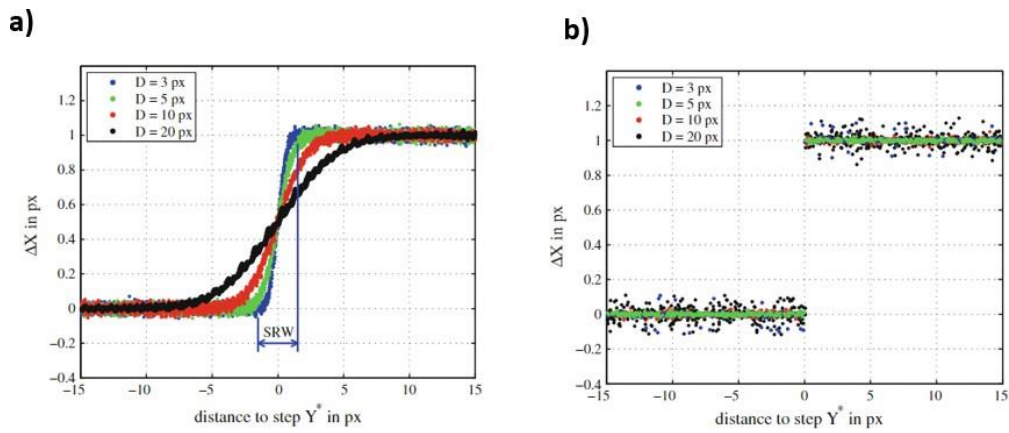
Figure 24: Comparison of response to a step-like displacement profile for different digital particle image sizes computed with a) PIV and b) PTV. (KAHLER et al., 2012).
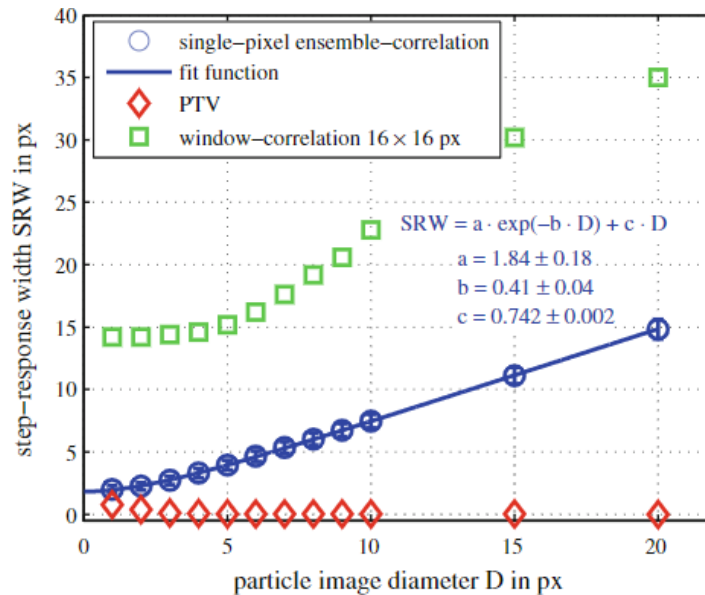
Figure 25: Step response width of the estimated displacement with respect to the digital particle image diameter. (KAHLER et al., 2012).

(KAHLER et al., 2012) also showed that the Dynamic Spatial Range (DSR) was almost three orders of magnitude larger than PIV processed with 8×8 pixel window. But some recommendations can be found, such as a high signal-to-noise ratio and a relatively low seeding concentration to avoid overlapping particle images. Thus, the PTV is a good way to substantially increase the spatial resolution and measurement accuracies.

3.3.1 Tracer particles

The tracer particle is extremely important for the measurement of the velocity of fluid flow, because the image analysis of the fluid depends directly on the behavior of the particle inside it. A good tracer particle achieves two goals: it follows the local fluid and scatters properly the light for imaging. Larger tracers have inertial error that influence and scatters more light, while smaller tracers easily follows the fluid and the fluctuations in turbulence, but scatters less light, so it is a trade-off situation. Therefore, the choice of the fluid tracer is a key parameter for any experimental measurement technique based particle imaging (MELLING, 1997) (DABIRI; PECORA, 2019).

In general, the main parameters are the particle size, shape, orientation and ratio of the refractive index of the medium to the particle itself. If the particle is spherical and with a diameter greater than the wavelength of incident light, then the Mie theory is applicable. Independent of the diameter of the tracer particle, the directions with the highest scattered intensity of light are observed between 0° and 180°, and the intensity of light scattering, in general, increases with the diameter of the particle as shown in Figure 26 (BERTI, 2018) (MELLING, 1997) (RAFFEL et al., 2007).
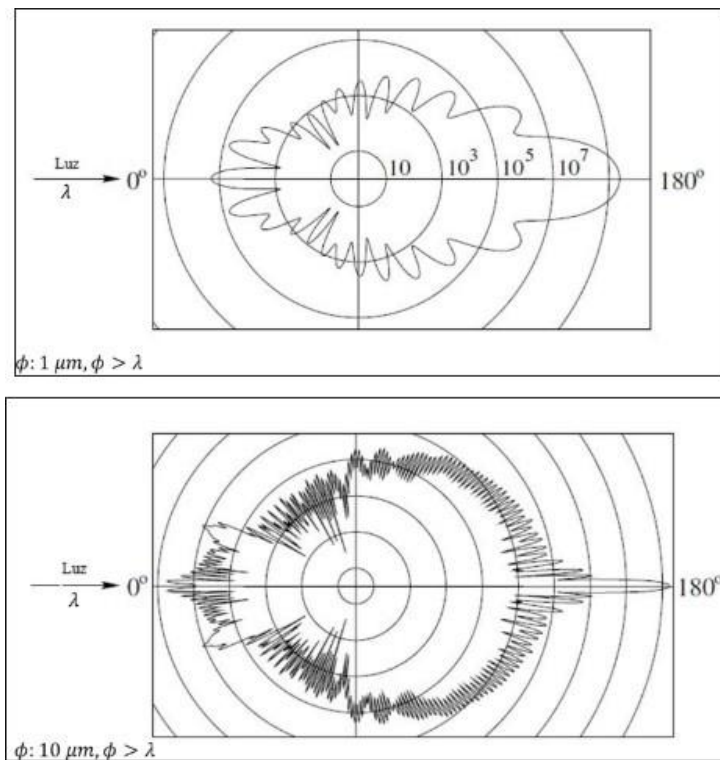
Figure 26: Light scattering according to Mie theory for particles of oil in air with diameters of 1μm (superior image) and 10μm (inferior image). Adapted from (RAFFEL et al., 2007).

To characterize a particle response time it is assumed that the velocity lag to velocity changes and the particle slip are small, so the Reynolds number of the particle (Re_p) is a small number, therefore the drag is given by viscous forces and the particle motion equation is

$$\frac{dU_p}{dt} = K(U - U_p) \tag{3.4}$$

$$Re_p = \frac{(U - U_p)d_p}{v_f} \tag{3.5}$$

Where $K = \frac{3C_D Re_p \mu_f}{4\rho_p d_p^2}$, is the entrainment coefficient. From Stokes's law, it is given by $18\mu_f / \rho_p d_p^2$. Here, μ_f and v_f are the fluid dynamic and kinematic viscosity, respectively, and ρ_p and d_p are the particle density and diameter, respectively. Since the particle is not in motion at $t = 0$ the equation integrates to

$$U_p(t) = U[1 - e^{-(t/t_s)}] \tag{3.6}$$

where t_s is the particle relaxation time and is given by

$$t_s = \frac{\rho_p d_p^2}{18\mu_f}$$

The particle relaxation time should be less than the smallest timescale of the flow in order to accurately represent the local fluid velocity (DABIRI; PECORA, 2019).

These particles can be used in liquid flows and gas flows, but they have different parameters to achieve a better measurement. An overview over tracers in subsonic gas flows can be found in (DABIRI; PECORA, 2019) (RAFFEL et al., 2007) (MELLING, 1997).

For evaluations of the particle response to isotropic turbulence, turbulence energy and Taylor microscale structures, the particle inertia parameter, which is the inverse of the particle response time, is defined as

$$\beta = \frac{9}{2} \frac{v}{(\rho + 1/2)a^2} \tag{3.7}$$

So particles should be large for solid particles in gas flows, and also large with $\rho \approx 1$ for solid particles in liquids (DABIRI; PECORA, 2019) (MEI, 1994).

Tracers particles in gas flows typically have a density ratio much greater than 1. The particle diameter should be selected to achieve a sufficiently relaxation time. For 1 kHz

response, $2 - 3$ μm diameter tracer particle is necessary, while a 10 kHz response requires less than 1 μm diameter particle. These frequency limits were calculated using Equation 3.7. These response frequencies and diameter of particles are show in Table 2 (MELLING, 1997) (DABIRI; PECORA, 2019).

Table 2: A maximum particle diameter according to the flow characteristic frequency and η = 0.99. Adapted from (MELLING, 1997).

Particle	ρ_p $(kg.m^{-3})$	Gas $(10^5 Pa)$	Density ratio s	Viscosity $v(m^2.s^{-1})$	f_c (kHz)	s_k	d_p (μm)
T_iO_2	3500	Air (100 K)	2950	1.50×10^{-5}	1 / 10	0.0295	1.44 / 0.45
$A\ell_2O_3$	3970	Flame (1800 K)	2025	3.00×10^{-5}	1 / 10	0.0113	2.46 / 0.78
Glass	2600	Air (300 K)	2190	1.50×10^{-5}	1 / 10	0.0342	1.67 / 0.53
Olive Oil	970	Air (220 K)	617	1.45×10^{-5}	1 / 10	0.0645	3.09 / 0.98
Micro Baloons	100	Air (300 K)	84.5	1.50×10^{-5}	1 / 10	0.1742	8.50 / 2.69

3.3.2 Illumination

The source of light responsible for particle illumination are lasers. They are capable of generating a monochromatic coherent light of elevated energy density, and with lenses converted into a sheet of light, since it is produced by light beam with low divergence. The most commonly used are Nd:YAG, which emit infrared radiation at 1064 nm and that are doubled to 532 nm, allowing for pulsed visible illumination (12 and 1000 mJ per pulse at 10 to 30 Hz).

The laser pulse frequencies are synchronized with the video camera frame rate to ensure unique exposed images. The 'frame-straddling' is a process that uses the pulse of light to expose the first image of the pair at the end of its frame, and exposing the second image of the pair at the beginning of its frame.

Recent technology developed the Nd:YLF laser, which is a laser beam generated by Nd^{3+} ions embedded in yttrium and lithium fluoride crystals, and it outputs for $10 - 20$

mJ per pulse at 527 nm at rates up to 10 kHz. Is has a dual-cavity where their beams are overlapped and combined into a single beam, as shown in Figure 28.
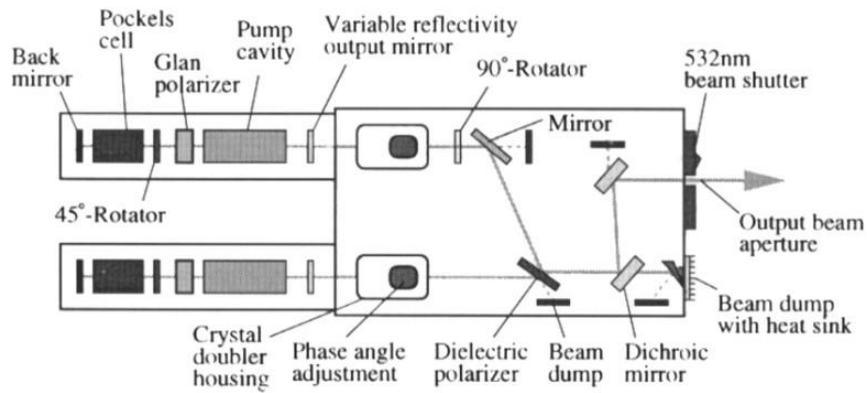
Figure 27: Dual-cavity Nd:YAG laser. (DABIRI; PECORA, 2019).

3.3.3   Camera

The image acquisition system is used with cameras that have an $m \times n$ light-sensitive pixel array to capture the scattered light from the particles. The most common, recently, are the CCD and CMOS video cameras. The first incorporate interlace frame-transfer chips that allow to incorporate circuitry for each pixel that performs signal processing, with a very fast readout. The CMOS cameras, associated with Nd:YLF, are suitable for high-speed image acquisition as high as 5 kHz, a simplified model of a CMOS sensor can be seen at Figure 28. Each individual pixel contains an electronic circuit. Additionally, the number of pixels to be active can be chosen by the definition of a subdomain, the region of interest (ROI). When associated with Nd:YLF they can achieve time-resolved PTV that record 1024×1024 - pixel images at framing rates up to 5000 frames per second. TR-PIV can measure temporal evolution of turbulent velocity fields. The rapid succession of double images offers new possibilities for the improved analysis of PIV, also PTV, images (DABIRI; PECORA, 2019) (WESTERWEEL et al., 2013).
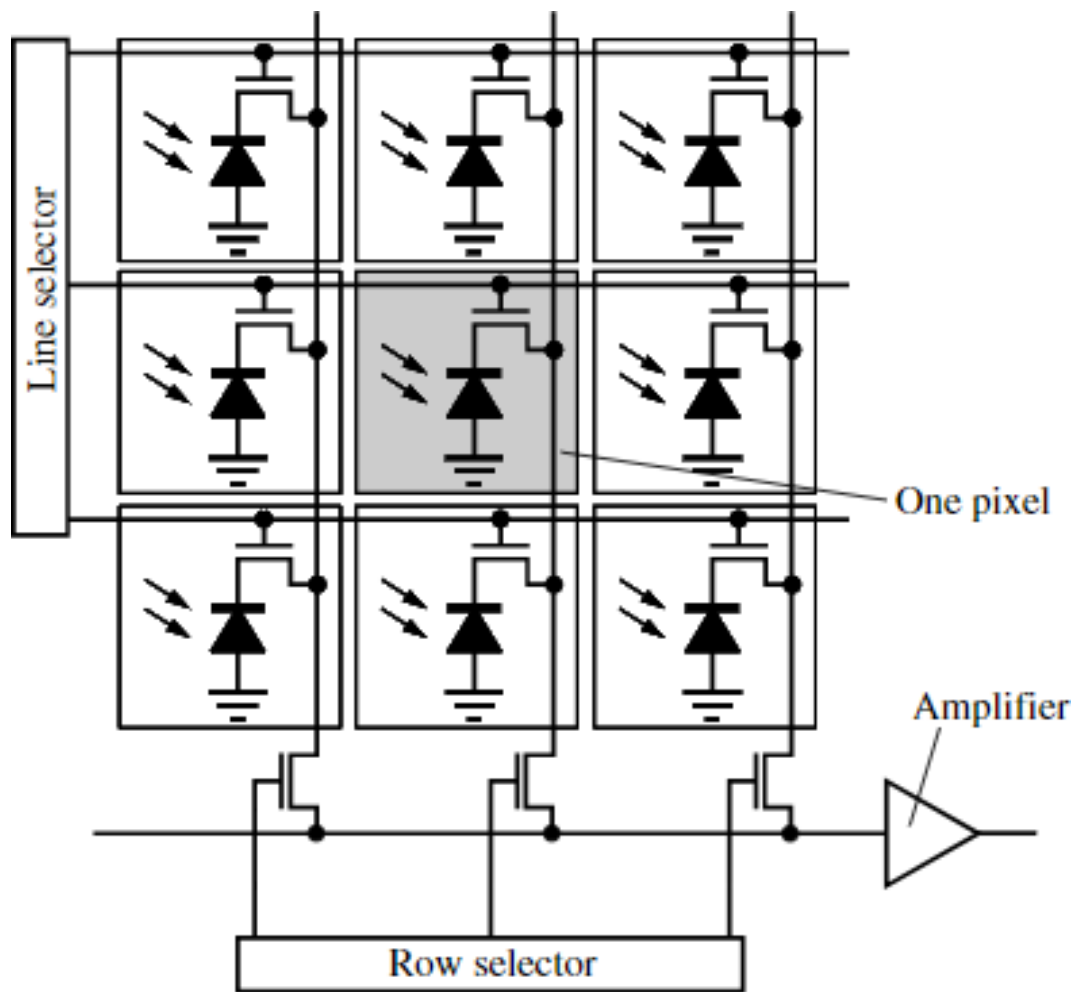
Figure 28: Simplified model of a CMOS sensor. (RAFFEL et al., 2007).

For the recording camera devices, the noise is inherent in each pixel. It introduces error on the measurement for particle identification. There are three most commons: Background noise, shot noise and device noise. The background noise is referred to camera output even in the absence of light, known as dark noise or dark current noise, which also increases with temperature and has a value of approximately the square root of the dark current. The rate of generation doubles for every $6 \sim 7^{o}C$ increase in temperature, which is a motivation for the use of cooled sensors. For a 256 in grayscale for 8-bit camera, it is about 30 counts and a random component characterized by Poisson distribution. Shot noise is the random fluctuation of conversion of light energy to electron flow. And device noise are the internal electronics, such as thermal, semiconductor surface and switching noise. These sources of noise adhere to a Gaussian distribution, and for PTV a high signal-to-noise ratio (SNR) is desirable, commonly designed by parametric optimization of these sources of noise (DABIRI; PECORA, 2019) (WESTERWEEL et al., 2013) (RAFFEL et

al., 2007).

3.3.4 Particle identification

There are two steps in particle identification. First, an algorithm must determine a group of pixels that are considered as a particle. Second, the location of this particle must be accurately determined. Accuracy in this step has an utmost significance, since the random errors in image position estimates propagate to both spatial position and velocity estimation (DABIRI; PECORA, 2019). A pre-processing process should contain bright particles in a black background. The use of segmentation for particle identification is done by threshold binarization, which is set to 1 if the gray level exceeds a set threshold and to 0 otherwise. This can be seen in Figure 29.
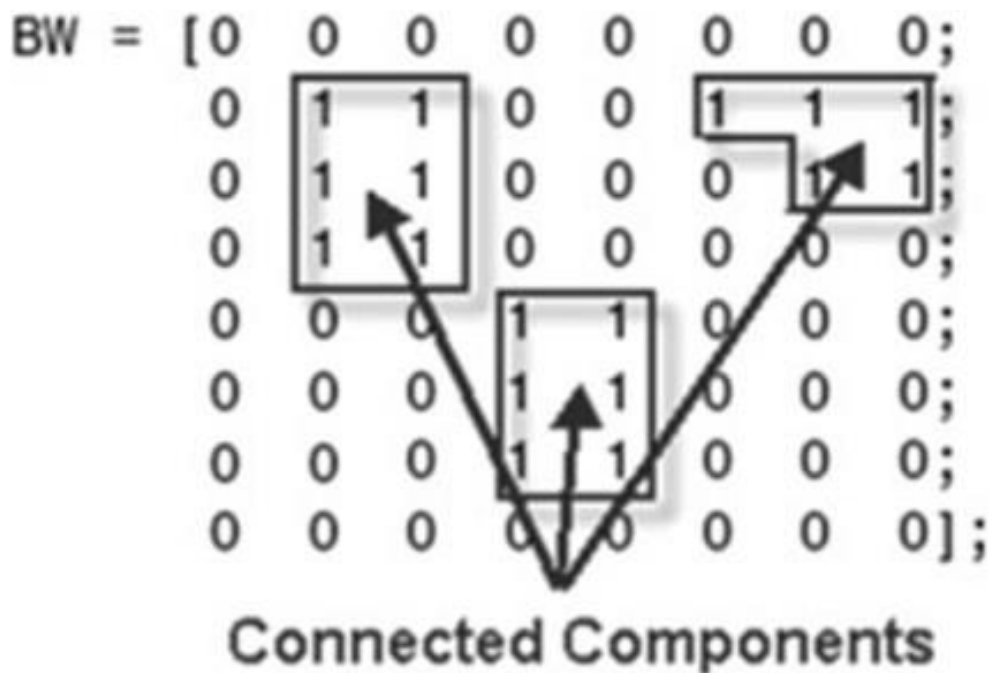
Figure 29: Binary matrix showing different identified particles. (LEI et al., 2012).

However, in real image analysis illumination inconsistency can exceed the global threshold, so a dynamic threshold binarization can be used by using local average and variance of pixel intensity. Both methods can be summarized by the Figure 30.
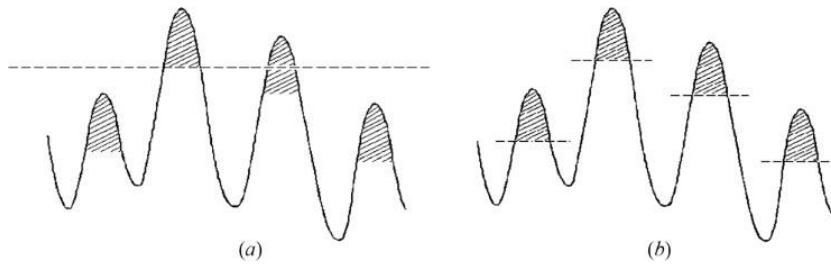
Figure 30: (a)Single threshold binarization (b)Dynamic threshold binarization. (OHMI; LI, 2000).

PTV methods are able to resolve sharp velocity gradients as well as out-of-plane velocity gradients so that background subtraction may not be always necessary. Objects are then identified in the foreground image by so-called "blob detection" method (HEYMAN, 2019). Once particle image blobs have been identified and separated from the background, the position in pixel domain need to be determined in order to accurately measure the flow velocities. Particles are determined in pixel level, however particle positions can be determined in a sub-pixel level. For non-overlapped particle images the three-point Gaussian and a least-square Gaussian estimator were studied, both comparable, but recommending the three-point Gaussian estimator for faster results (100 times faster) (DABIRI; PECORA, 2019). These algorithms are based in the assumption of spherical particles and the sub-pixel accurate detection of the tracer particle is achieved by a Laplacian of Gaussian image filtering technique followed by a Gaussian interpolation of the particle peak intensities (HEYMAN, 2019).

In a planar analysis, the spatial location in 2D can be geometrically determined in spatial coordinated from the camera plane. Assuming a pinhole camera model, the Equation 3.8 can be used to transform the image coordinates, X and Y, to spatial coordinates x and y, respectively. As Z_o is the distance from the image to effective center of the lens and z_o is the distance from the object to the effective center of the lens, as shown in Figure 31.

$$\frac{X}{Y} = \frac{Z_o}{z_o} \frac{x}{y} \tag{3.8}$$
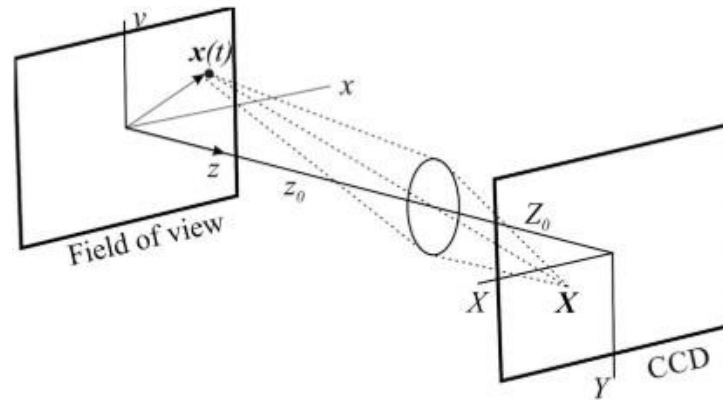
Figure 31: The geometry used in the pinhole model for determining 2D spatial coordinates of particles. (DABIRI; PECORA, 2019).

The "blob detection" method mentioned integrates two state-of-art detectors: Difference of Gaussians (DoG) and Laplace of Gaussian (LoG). They depend on exclusively from a single parameter, δ, which is the bandwidth for filtering. The DoG convolves the image with a filter constructed from the subtraction of two Gaussian of bandwidth 0.8δ and 1.2δ. It acts as a band-pass filter, selecting blobs in the 20% scale range around $\delta\sqrt{2}$. The LoG first convolves the image with a Gaussian filter of bandwidth δ, then applying the Laplacian operator on the convoluted image. Both approachs yield a filtered image (F_t') with a strong positive response in the presence of objects of scale δ. Positions of the object centroids are obtained by searching for local maximum in F_t', and to minimize false detections, an intensity threshold ϵ is fixed under which maxima are ignored (HEYMAN, 2019). The sub-pixel resolution of object position is achieved by fitting a quadratic or a Gaussian function to the pixel intensity values around the centroid position. The sub-pixel position of an object for a quadratic function will be

$$x = j + \frac{F_{i,j+1}' - F_{i,j-1}'}{2(F_{i,j+1}' - 2F_{i,j}' + F_{i,j-1}')} \tag{3.9}$$

$$y = i + \frac{F_{i+1,j}' - F_{i-1,j}'}{2(F_{i+1,j}' - 2F_{i,j}' + F_{i-1,j}')} \tag{3.10}$$

The equations are the same for a Gaussian function, replacing F' by $ln(F')$. The ensemble of points made of the sub-pixel centroid positions are then tracked through time (HEYMAN, 2019).

3.3.5 Particle Tracking techniques

The next step for PTV algorithms is to determine the velocity field from particle spatial locations. There are several algorithms developed over the last decade and used in both two- and three-dimensional problems. The extension of the algorithms requires a simply addition of a z-coordinate to position vectors in many cases. Over the last year, some algorithms are summarized below. If the reader need more information about the specific tracking technique, it is strongly recommended to study the Chapter 5 of (DABIRI; PECORA, 2019). This section is divided into the most common tracking algorithms: multi-frame approach using time-resolved PTV data; Cross-correlation method; Relaxation methods for iteratively selecting probable matches based on nearby particles and a Statistical approach which was the method used for the present work.

3.3.5.1 Multi-frame approach using time-resolved PTV

The multi-frame tracking technique is used as temporal information to identify a particle's trajectory over recording time steps. It can be used between two and four frames, in a regular time interval. Some requirements for this approach are the low-speed flows or high frame-rate cameras. As described in (DABIRI; PECORA, 2019) a first and simplest approach is the use of nearest neighbor tracking, as shown in the Figure 32, but this method makes no assumptions about the movement of neighboring particles, and does not exclude particles sharing a match in a frame (HASSAN; CANAAN, 1991).
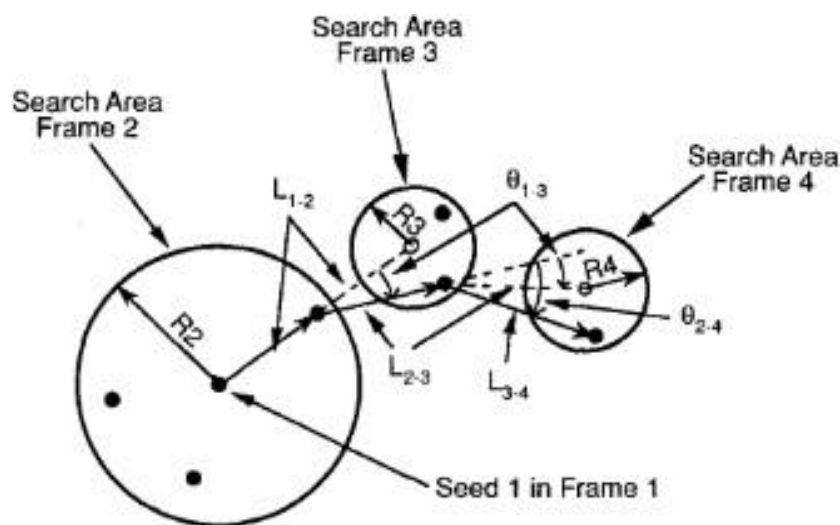
Figure 32: Figurative description of the nearest neighbor tracking algorithm. (HASSAN; CANAAN, 1991).

A second approach is introduced considering the acceleration of the particle in the previous three frames, the three-frame minimum acceleration (3MA) uses the most likely path based on a minimizing acceleration, this acceleration is calculated for each three-point track where Δt is the time elapsed between frames. Additionally, the four-frame minimum acceleration (4MA) approach is based on minimizing the change in acceleration along a particle path, used for 3D tracking. Another technique was introduced as a modification called four-frame best estimate (4BE), which does not minimize the change in acceleration. Instead of minimizing the difference between the projected fourth particle position, it assumes a constant acceleration, which is based on the known positions and velocities at the first three points. However, this approach has outcomes when the best match for two reference particles in the most recent frame are the same, in this way this technique need to use an algorithm for the cost minimization or start a new track with a new particle. A good representation of those techniques is summarized in the Figure 33.
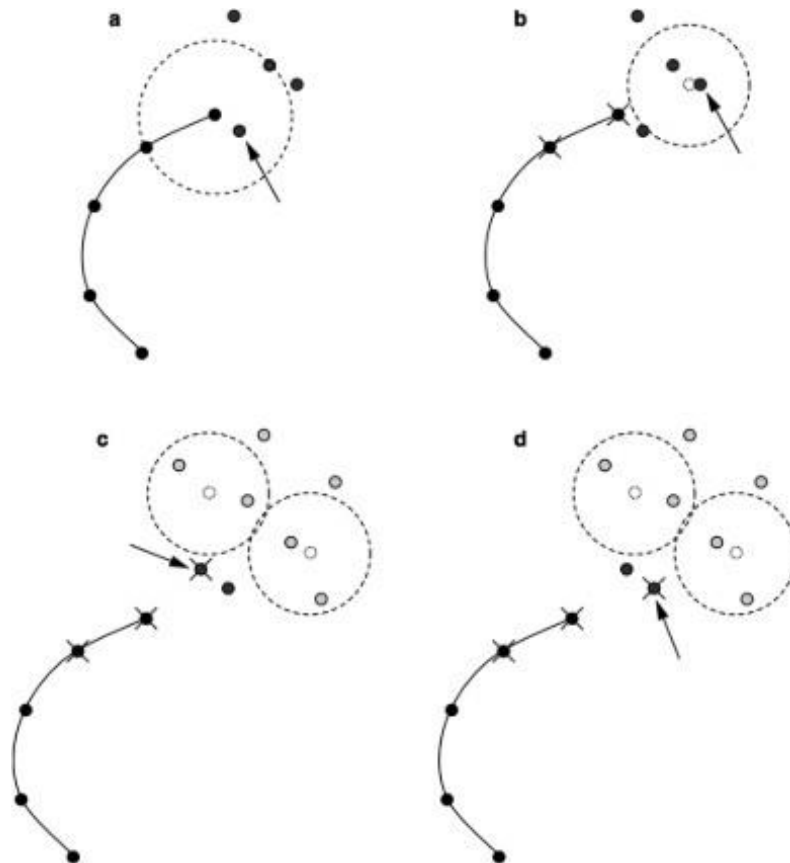
Figure 33: The heuristics used for multi-frame particle tracking algorithms (a) Nearest neighbor (b) Three-frame minimum acceleration (c) Four-frame minimum change in acceleration (d) Four-frame best estimate. (DABIRI; PECORA, 2019).

3.3.5.2 Cross-correlation method

A common two frame matching particles in PTV is the cross-correlation method, which is based in the principle that a fluid particle and its closest neighbor particles move in a rigid-body motion, so it is used to determine the probability of a candidate particle in the first frame being a match with a candidate particle in the second. A technique called Binary Cross Correlation (BCC) was created by (YAMAMOTO et al., 1993), where the particles are identified and binarized to use only the particle position, rather the pixel intensity. This technique has a high-speed algorithm for particle identification and takes a very short time to compute the velocity vectors. First, a cubic search subregion with a side length is done whose center has the same coordinates as the center of a reference particle i, so they become the candidate particles j. Second, the origin of the coordinate system is moved to make the center of the candidate the same as the reference particle. Third, an identification subregion with a new side length is done with the same coordinates as the center of the reference particle. The particle distribution patterns are made up of the particles in the first and the second identification subregions. Fourth, after the pattern is overlapped between them, the number of particles which are overlapped with each other in the overlapped patterns is counted. An image of the process can be seen in the Figure 34. The neighbor particles are called N_i and N_j for i and j, respectively.
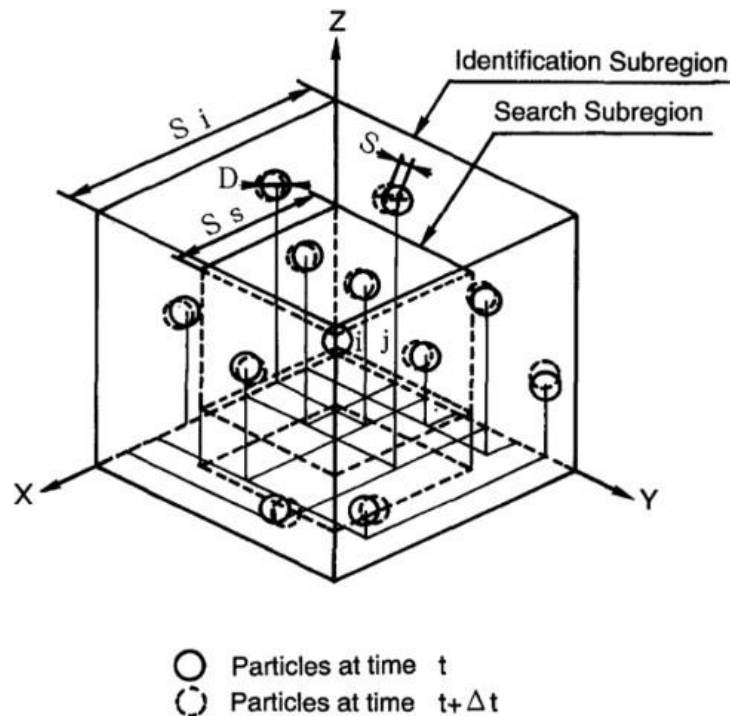
Figure 34: Particle positions from consecutive PTV frames with reference particle i overlapped with candidate particle j. (YAMAMOTO et al., 1993).

The correlation coefficient for each candidate particle is calculated as

$$C_{ij} = \frac{\sum_{k=1}^{N} 1 - \frac{3}{2}S_k + \frac{1}{2}S^3}{N \ N}$$

(3.11)

This correlation coefficient is equivalent to the calculation of the total overlapped volume between the particles in the reference and candidate sub-regions (DABIRI; PECORA, 2019). It is important to notice that the binary-image cross-correlation method is considered a variation of the standard cross-correlation PIV, in which the correlation functions are computed for each interrogation window centered on the first-frame particles using an adaptive shifting scheme (OHMI; LI, 2000).

3.3.5.3 Relaxation method

This method consists similarly to BBC method, the difference, however, is that in the relaxation method the neighbor particles do not need exactly to overlap. As a result, the algorithm allows adjusting for velocity gradients and rotation within the flow (DABIRI; PECORA, 2019). The difference that makes possible the applicability is that the cross-correlation method is increased only if the neighboring particles find their partners at exactly the same relative displacement points. On the other hand, the relaxation method is increased if only the neighboring particles find their partners within a finite distance from the parallel displacement point, as seen in the Figure 35.
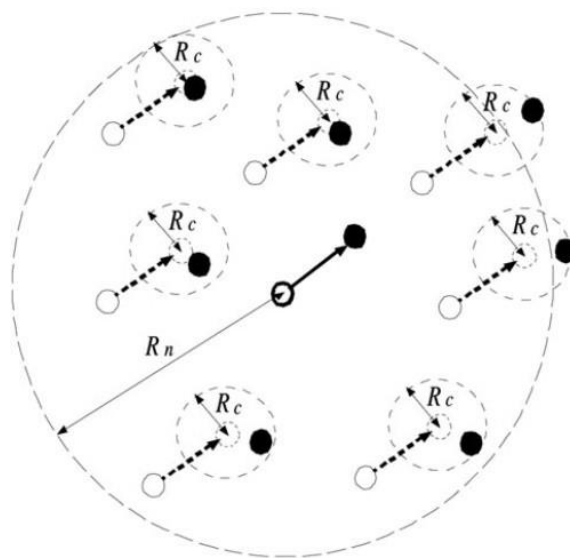
Figure 35: The quasi-parallel motion of the relaxation method. (OHMI; LI, 2000).

The basic concept of the relaxation method is similar to the BBC method because

every possible movement of the reference particle in the first frame is checked in the light of that of the neighboring particles (OHMI; LI, 2000). The main advantage of this relaxation method is that the analysis is based on the probability of particle matching between the first and second frames defined for every possible pair of particles, included the probability of no-match or loss of a partner (OHMI; LI, 2000). A sequence of development was conducted trying to overcome the applicability to higher density particle images, since hybrid PIV/PTV method in which standard cross-correlation PIV is employed prior to the individual particles tracking, in order to estimate in advance the local velocity to be measured by PTV (OHMI; LI, 2000). However, these methods which are a combination of techniques do not effectively detect the small local structures in fully turbulent flows, as a result the need for further improvement of the PTV algorithms are necessary.

A brief review of the three steps for this method is described, based on the work of (OHMI; LI, 2000). First, every first-frame particle pre-selects its candidate partners from second-frame using

$$|x_i - y_i| < R_s \tag{3.12}$$

As x_i and y_i are the coordinate vectors of the first-frame and second frame particles, and R_s is the maximal possible displacement of the particles. Also, the first every-frame selects its neighbors in the same first frame using

$$|x_i - x_k| < R_n \tag{3.13}$$

As x_i and x_k are the coordinate vectors of the reference and neighboring particles and R_n is the radius of vicinity in which the similarity of the particle movement is preserved.

A probability of matching between the first-frame particles and their respective candidates in the second frame is introduced. Using the initial probabilities can be estimated in various ways as cross-correlation functions or others. An example of initialization of the particle-matching probability is shown by the Figure 36.
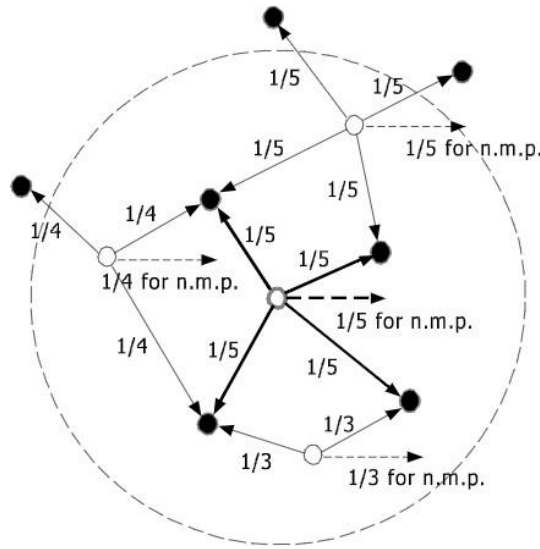
Figure 36: Initialization of the particle-matching probability (n.m.p. stands for the no-match probability). (OHMI; LI, 2000).

The second step consists in the particle matching update for each iteration. In order to update the match probability between the reference particle and a candidate particle and is expressed by

$$\tilde{P}_{ij}^{(n)} = P_{ij}^{(n-1)}\left(A + B \sum_{k}\sum_{l} P_{kl}^{(n-1)}\right) \tag{3.14}$$

Where $\tilde{P}_{ij}^{(n)}$ is the updated probability for each iteration, A and B are constants in the equations, set to be 0.3 and 3.0, respectively (OHMI; LI, 2000).

In the third step, the updated probability $\tilde{P}_{ij}^{(n)}$ is normalized in order to satisfy

$$\sum_{j} P_{ij} + P_i^* = 1 \tag{3.15}$$

The usual scheme for this normalization is the following

$$P_{ij}^{(n)} = \frac{\tilde{P}_{ij}^{(n)}}{\sum_{j}\tilde{P}_{ij}^{(n)} + P_i^{*(n-1)}} \tag{3.16}$$

And the no-match probability itself is normalized by

$$P_i^{*(n)} = \frac{\tilde{P}_i^{*(n-1)}}{\sum_{j}\tilde{P}_{ij}^{(n)} + P_i^{*(n-1)}} \tag{3.17}$$

The update and normalization of the matching probabilities are iterated 10 to 20 times in order that they converge at constant levels and the correct matching is increased almost

to unity while the others tend to zero.

3.3.5.4 Statistical approach

This approach was developed to use that main advantages of the PTV compared to the statistical analysis of an ensemble of particles images by means of cross-correlation approach, as PIV. Tracking individual particles do not suffer from spatial averaging and therefore bias errors can be avoided (FUCHS et al., 2017). Also, the spatial resolution can be increased up to the sub-pixel level for mean fields, specially with high seeding concentrations. It is a challenge to track high seeding particles concentrations which uses typically very complex iterative algorithms to perform, which needs expert knowledge for adjusting many parameters.

To overcome this scenario, a non-iterative tracking approach was developed by (FUCHS et al., 2017), which analyses the motion of the neighboring particles without requiring to specify any parameters, except for the displacement limits. This allows inexperienced users to use and implement particle tracking using standard double-pulse equipment and estimates the flow velocity reliably even at large particle image densities (FUCHS et al., 2017).
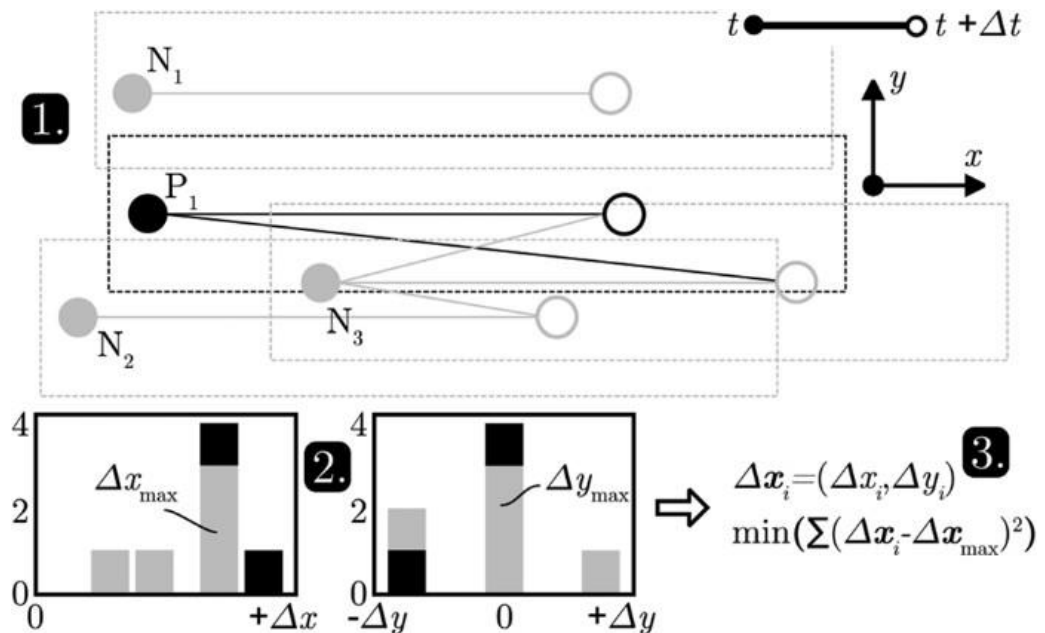
Figure 37: 1) *Dashed lines* displacement limits; *Solid lines* possible displacements. 2) Displacement histograms, where the maximum value is determined (Gaussian fit) 3) Particle P_1 is matched with the *black particle*, *hollow particle* at $t + \Delta t$, since the displacement has the lowest deviation from the histogram maxima. (FUCHS et al., 2017)

This approach is based on three steps, according to Figure 37: First, all possible displacements (solid lines), with a given range (dashed line) between the particle of interest P_1 (filled black) and its three neighbors $k = 3$, $N_{1,2,3}$ (filled with grey) in the first image to particles in the second image (hollow particle) are obtained. Second, histograms are obtained for all possible displacements of P_1 and its three neighbors, and the maxima of these histograms are identified for each direction. Third, the displacement of P_1 to its location in the second frame is determined by the smallest absolute deviation as the most probable displacement (black hollow particle). To allow for statistical analysis, the bin number of the histograms is defined by the rounded value of one-tenth of the number of all possible displacements. The maxima of the histograms are determined using a Gaussian fit to increase the accuracy (FUCHS et al., 2017) (DABIRI; PECORA, 2019). It is worth mentioning that there is a rigid body hypothesis for the selected particle and its neighbors. Consequently, the peak is the most probable particle trajectory.

The method was tested and compared with other algorithms with a synthetic image set for performance analysis, and the results were found that it yielded 95.15% of valid tracks with 2.25% of invalid tracks. These results compare well with those shown in the Table 3, which comes at the third place after vision-based and the VAR method (DABIRI; PECORA, 2019) (LEI et al., 2012).

Table 3: PTV results with known and unknown particle location for Vision-Based-PTV and previous tracking algorithms). (LEI et al., 2012).

Algorithm	Particle location	Matches possible	Matches found	Matches correct	Match yield (%)	Reliability (%)
Present work (tracking only)	Known	4,042	4,039	3,927	97.23	97.15
VAR (Ruhnau et al. 2005)	Known	4,042	4,039	3,894	96.34	96.41
EPTV (Mikheev and Zubtsov 2008)	Known	4,042	3,863	3,823	94.58	98.96
ICCRM (Brevis et al. 2011)	Known	4,042	NA	3,980	98.46	NA
Present work (particle identification + tracking)	Unknown	2,095	1,846	1,761	84.06	95.40
EPTV (Mikheev and Zubtsov 2008)	Unknown	2,029	1,759	1,733	85.41	98.52
VAR (Ruhnau et al. 2005)	Unknown	NA	872	865	NA	99.20
NRX (Ohmi and Li 2000)	Unknown	NA	808	788	NA	97.52
MF-EPS (Shindler et al. 2011)	Unknown	NA	1,160	1,146	NA	98.80
2F-EPS (Shindler et al. 2011)	Unknown	NA	1,123	1,112	NA	99.00

In conclusion, the statistical method offers a powerful alternative to cross-correlation methods for strong velocity gradients. The algorithm is computational efficient, robust, user-friendly and shows acceptable results for high particle densities such as spray development environment.

3.3.6 Outlier detection

For all algorithms presented, and others that have their reliability below 100%, which has at least 1 incorrect particle track, it has an utmost importance to have an algorithm that determines outliers particles and remove them. To do not influence the correct data and affects the differential and integral quantities for vorticity and streamlines (DABIRI; PECORA, 2019).

Many techniques were developed for this purpose, however, it is necessary to explore the technique used in the present work. The universal outlier detection method adopted from (WESTERWEEL; SCARANO, 2005) is indicated for gridded PIV data and has short computation time. This method has been generalized to work for scattered PTV data by (DUNCAN et al., 2010) to enhance the quality of the displacement field reconstruction. Two problems arise when considering the application of a normalized residual test to the scattered data resulting from PTV. First, solve the identifying neighbors. Second, the data resulting from PTV processing are not equally spaced, and thus, should not have the same influence in determining the viability of a vector (DUNCAN et al., 2010). The reason for the adaptation proposed by (DUNCAN et al., 2010) is that the normalized residual defined by (WESTERWEEL; SCARANO, 2005) works well for the gridded data of PIV, however, do not remove spurious vectors from the randomly distributed data of PTV (DUNCAN et al., 2010).

So, a proposed technique Delaunay Tessellation, which is a triangularization method based on triplets of points in two dimensions, was used as a convenient method of defining neighbors as those data point which share triangles, on average each point will have five to eight neighbors. In the space between the neighbors, a closer neighbor should have more effect than the others, thus, all the data points should be weighted by their distance from the point in question. These neighbors were used to calculate a normalized residual, which is defined as

$$r_0^* = \frac{|U_0 - med(U_i)|}{med|U_i - med(U_i)| + \varepsilon_a(d + \varepsilon_a)} \tag{3.18}$$

Where U_0 is the velocity measured at the data point in question, U_i is the velocity of each of its neighbors, med means the median of its neighbors, d is the median of the distances between each of the neighbors and the data point in question, and ε_a is the adaptive tolerance, which was set as 0.1 by (WESTERWEEL; SCARANO, 2005). The performance of this outlier detection scheme for gridded and scattered data can be seen in the Table 4.

Table 4: Detection capability on data with added outliers. (DUNCAN et al., 2010).

Added outliers	PIV 1	PIV 2	PTV 1	PTV 2
0%	0.1%	0.4%	0.9%	0.6%
5%	5.0%	5.3%	5.7%	5.5%
10%	10.0%	10.0%	10.3%	9.9%
15%	14.4%	16.2%	14.2%	13.8%

As a conclusion, this method works fine for PIV and PTV data up to a level of spurious about 15%, beyond this level adjacent outliers affect one another and are either not detected or cause correct vectors to be misidentified as outliers. An adaptive tolerance related by (WESTERWEEL; SCARANO, 2005) of 0.1 pixel was proposed. A threshold of 2-4 for the normalized residual was found to work well. (DUNCAN et al., 2010) recommended to use 2 for any flow with a large percentage of spurious vectors are anticipated.

3.3.7 Considerations

All the presented information along the chapter had the objective to summarize and clarify the most important knowledge about the proposing work. Based on the objective presented on chapter 2, the measurement of the PTV technique for ethanol spray is important because looking into the previous works, there is a gap to overcome that could to be explored by PTV. The overcome is the lower tracer particle densities, where it had in average N_{ppp} = 0.05 particles per pixels for the experiment. This opportunity makes possible the PTV technique for continuous flow that surrounds the spray (air). The contribution of this work, which is PTV analysis for the surrounding air of ethanol spray, will be fundamental to the progress of the knowledge of two phase flow and surrounding air development during a direct injection event.

4   METHODOLOGY

This chapter is divided into three parts. As this work is an extension with a PTV analysis from measurements done by (BERTI, 2018) it is relevant to summarize the main characteristics used and to introduce the Isothermal Ethanol Spray Chamber (IESC) and the experimental procedure. The first part is dedicated to introduce the methodology of (BERTI, 2018). The second part is the selection of the specific cases for PTV analysis which matches with the PTV characteristics for better results. The third part is the PTV optimization that includes about pre-processing, algorithm, PTV strategy analysis and post-processing.

4.1   Experimental arrangement

The direct injection spark ignition (DISI) engines operate their injection during on the intake stroke. On that condition, the spray encounters the air flow in the cylinder with a relatively low ambient pressure. The effects of the air flow and spray interactions, specially in terms of turbulence, are still not well understood.

To evaluate this, the IESC apparatus was designed for the analysis of continuous flow properties on air-spray interactions. The advantage is that it provides more controllable boundary conditions in terms of airflow characteristics, turbulence, and fuel injection. When compared to engine operations, they are less sensitive to instabilities and cycle-to-cycle variations (BERTI, 2018). Different from a Constant Volume Combustion Chamber (CVCC), the IESC operates near ambient conditions where the spray encounters the airflow that is entering the cylinder. It represents general conditions of a real engine cycle, except for low RPM or high-performance demands, where the stratified injection is applied, as shown in Figure 38.
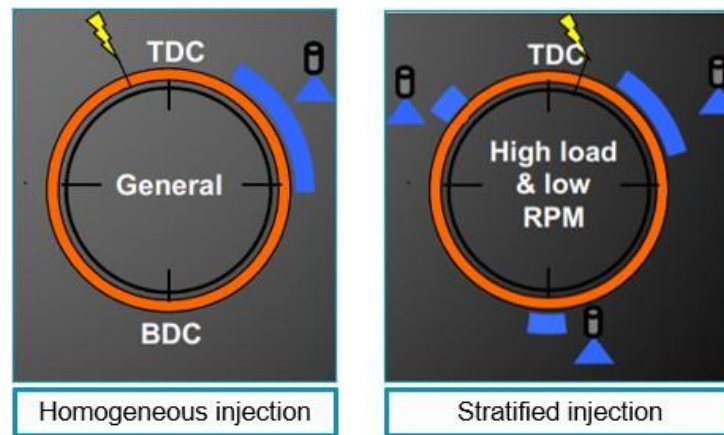
Figure 38: Schematic of the difference between homogeneous injection and stratified injection and its demands. (BERTI, 2018).

The main objective of the IESC is to evaluate the spray development flow field for general conditions of an engine and its turbulent properties, specially for studying spray-air interaction. The IESC is illustrated in the Figure 39.
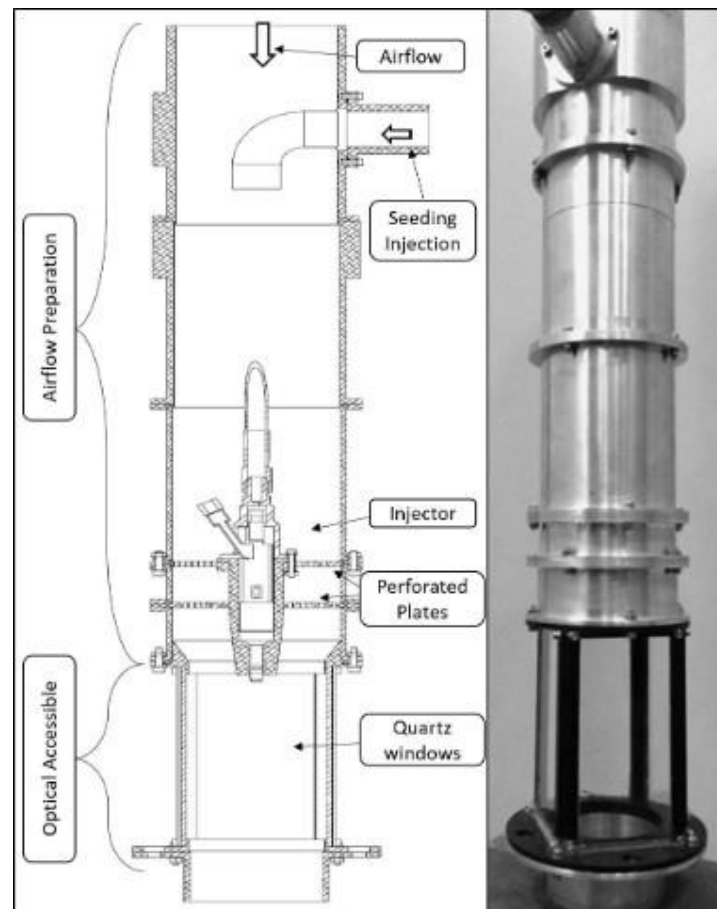
Figure 39: The main components of the IESC and a photograph of the apparatus. (BERTI, 2018).

The experimental arrangement is divided into subsystems and a brief discussion on aspects for proper relation on measurement will be made. The flow is divided into two main sections: The air flow preparation and the optical accessible section. The air enters on the top, with a section of 500 mm in length and 100 mm in diameter. The area of injection corresponds to a standard space for the combustion chamber of modern spark ignition engines. It was made with 20.4 × 29 mm, as shown in Figure 45. The comparison between an experiment with E-10 gasoline spray injection shows that the Field Of View (FOV) was similar for both experiments, as shown in Figure 40.
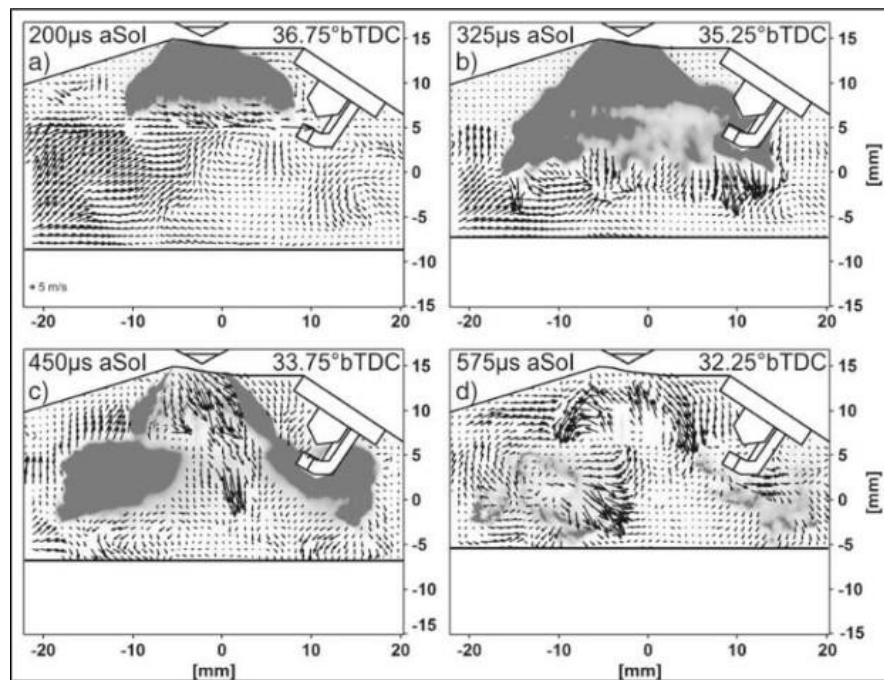
Figure 40: Temporal evolution of spray development conducted inside an DISI optically accessible gasoline engine. (STIEHL et al., 2013).

The seeding with particles is injected subsequently for mixing with the air. A set of two perforated plates were installed near the end of the airflow, which can provide a more controllable turbulence in terms of temporal and length scales. They have different bore diameters: 2 mm, 4 mm and 6 mm, as shown in the Figure 41. The holes are organized to maintain an approximate equal solidity. Also, the parameter is used to scale the degree of turbulence to different inlet geometries in wind tunnels. Additionally, they set a limit for turbulence integral length scale in the flow.
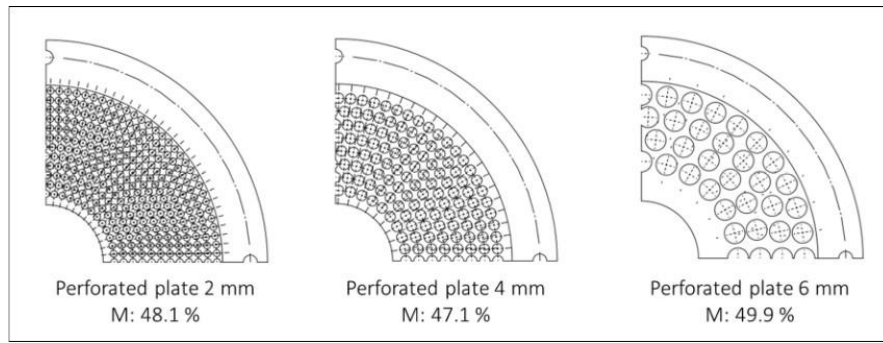
Figure 41: Schematics of the three possible sets of perforated plates used in IESC. (BERTI, 2018).

In the IESC, the two-phase technique for PIV measurement was made. Using a *Laskin* nebulizer, the optical separation of the air and the spray droplets were made by Rhodamine B, dissolved with an oil (propylene carbonate). The determination of the maximum particle diameter should garantee a Stokes number smaller than 0.1 and be in accordance with the criteria of frequency response according to (MELLING, 1997) (BERTI, 2018). The maximum particle diameter for propylene carbonate in air is shown in Table 5.

Table 5: Maximum particle diameter for propylene carbonate in air according to criterion developed in (MELLING, 1997).

Particle	ρ_p $(kg/m^3)^1$	Gas $(10^5 Pa)$	s	ν $(m^2 s^{-1})^2$	f_c (kHz)	S_k	d_p (μm)
Propylene	1198	Ar	928.7	2.08	1	0.05	0.96
Carbonate		(300 K)		x 10^-6	10	2	0.30

The distribution of the size of the seeding was adequated modeled for log-normal distribution with Sauter Average Diameter (SMD) near to 3μm (TODARO et al., 2020). The laser used was a LDY302 with double cavity and Nd:YLF technology, from Litron Inc., the wavelength of the laser is 527 nm and 15 mJ per pulse at 1 kHz. The lenses distributions could make a sheet of light with 50 mm of width and 5 to 50μm thickness. The injector was a high pressure multi-hole injector from *Delphi Powertrains Systems* with five openings arranged radially from the axis. This injector is used for DISI and their center plumes are not symmetric from its axis. The injector is capable of 7.63 mg/pulse of dynamic fuel flow for n-heptane operating at 100 bar of injection pressure with SMD 12μm.

It is important to emphasize that, on the (BERTI, 2018) work, the two-phase particle image velocimetry was conducted. For some sprays, droplets may become natural tracer particles of the flow and with an introduction of artificial particles such as Rhodamine B in the air the environment is mixed with two source of velocity information: the droplet and the Rhodamine B particle. Two cameras were used on the experiment, one of them responsible for receiving the light scattering from droplets (same wavelength of the laser beam), and the other captured the fluorescence of Rhodamine B. Both were positioned orthogonally from the laser sheet. The absorption peak occurs at 542.75 nm, and the emission peak occurs at 565 nm, they both can be seen in Figure 42. Using a long-pass optical filter, the camera responsible for Rhodamine particle acquisition was only be sensitive to wavelengths greater than 570 nm, this way eliminating all laser light scattered by the spray.
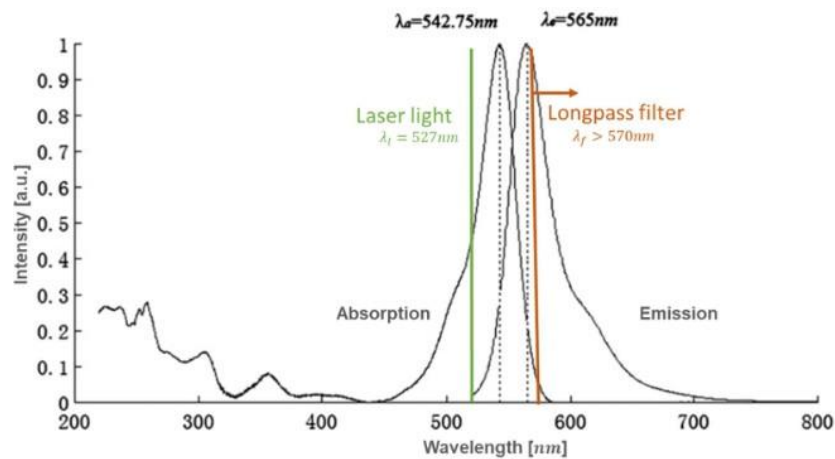
Figure 42: Emission and absorption spectra of Rhodamine B dissolved in ethanol. (YANG et al., 2011).

The cameras were Phanton V3.11 of 16 GB of internal memory from Vision Research Inc. with a sensor *CMOS* of 1280 × 800 pixels - *pixel pitch* equals to 20μm - with 12 bits of resolution. The disposal of the cameras for two phase acquisition is shown on the Figure 43.
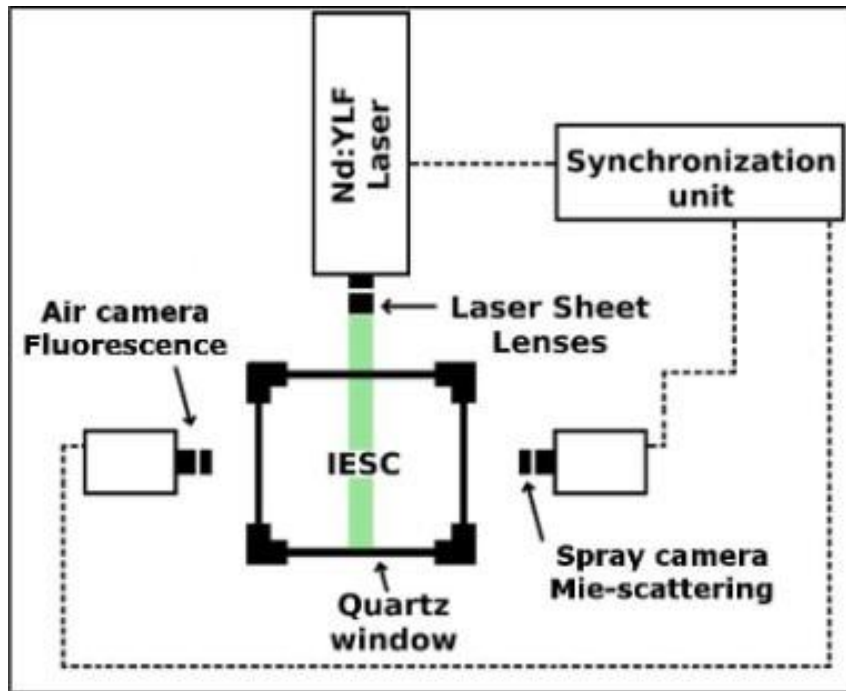
Figure 43: Camera disposal visualization for two phase acquisition. (BERTI, 2018).

Additionally, the acquisition frequency of each unity is near to 5000 fps and the pair was equipped with *Planar* 1.4/50 ZF (focal distance of 50 mm and f_n equals to 1.4), from Carl Zeiss (TODARO et al., 2020) (BERTI, 2018). The injector controller synchronized with cameras and injector was a direct injection module NI 9751 from manufacturer National Instruments. The configuration was achieved with an interface created in the LabView software®. To supply the high-pressure fuel system, the fuel pressurization was made in two stages. First, to elevate the pressure to 2 bar of relative pressure with an electric automotive fuel pump in a by-pass circuit. The second stage elevated the pressure to a range of 80 to 120 bar. The air supply system was composed of the blower (rotary lobe blower model DB 236 C, manufactured by *Kaeser Compressors* controlled by a frequency inverter model CFW08 by *WEG*). The instrumentation were air flow meter, pressure transducer, thermocouple, Laskin generator and filter. The air mass flow rate was kept at 0.06538 kg/s, resulting into a Reynolds number of 4.18×10^4 using IESC hydraulic diameter. All the subsystems used for the experiment are shown in the Figure 44.
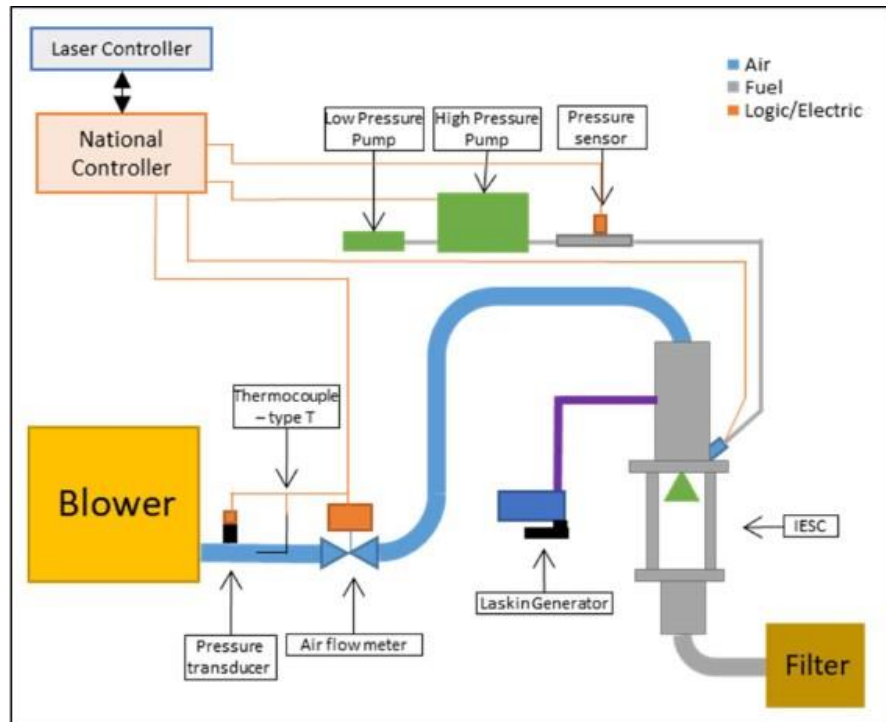
Figure 44: Operation of the equipment during the experiments with IESC. (BERTI, 2018).

4.2   Especific cases selected for PTV analysis

On this chapter, the specific case selected is considered from all experimental data obtained. First, the (BERTI, 2018) experiment conducted the technique of two-phase PIV, which has an optical separation between the air and the spray droplets. The configurations were defined by their pressure on the injector, on the air mass flux and the diameter of the holes used on IESC configuration. Over all experimental data captured, one specific case will be analysed. The main parameter for choosing case is the best fit for PTV analysis. The average air mass flow rate was 0.066 kg/s (quiescent environment), 4 mm diameter for the holes, the integral length 3.5 mm and Reynolds number of 4.22×10^4. The values of the air mass flow represent the expected average of a 1.4 liters engine capacity DISI turbocharged engine operation in mid-high loads between 2000 and 3000 rotations per minute (BERTI, 2018). The scenario of all parameters can be seen on the Table 6.

Table 6: The conditions of the cases in the spray-air interaction analyses. (BERTI, 2018).

Perforated plate	PP2			Integral length scale
	Air mass flow [kg/s]	Injection Pressure [bar]	Reynolds number []	From inlet [mm]
Case PP2-01	0.06536 ± 0.00080	100 ± 5	$4.18x10^4$	2
Case PP2-02	0.06539 ± 0.00088	60 ± 3	$4.18x10^4$	2
Case PP2-03	0.09786 ± 0.00095	100 ± 5	$6.25x10^4$	2
Perforated plate	PP4			
	Air mass flow [kg/s]	Injection Pressure [bar]	Reynolds number []	From inlet [mm]
Case PP4-01	0.06614 ± 0.00082	100 ± 5	$4.23x10^4$	3.5
Case PP4-02	0.06568 ± 0.00081	60 ± 3	$4.22x10^4$	3.5
Case PP4-03	0.09674 ± 0.00091	100 ± 5	$6.19\ x10^4$	3.5
Perforated plate	PP6			
	Air mass flow [kg/s]	Injection Pressure [bar]	Reynolds number []	From inlet [mm]
Case PP6-01	0.06552 ± 0.00078	100 ± 5	$4.19\ x10^4$	5
Case PP6-02	0.06553 ± 0.00083	60 ± 3	$4.20\ x10^4$	5
Case PP6-03	0.09664 ± 0.00092	100 ± 5	$6.18x10^4$	5

From all those cases presented, one case will be selected for further PTV analysis. For better visualization, the chosen image should have a lower injection pressure that ensure a better tracking technique, since the spray becomes diluted and easier to identify the droplets from images. With that information in mind, the possible cases are PP2-02, PP4-02 and PP6-02. However, as this work has the objective to improve information and compare both PIV and PTV techniques, it is necessary to select the case with most previous information. As a continuation of (BERTI, 2018) work, (TODARO et al., 2020) made two PIV analysis from (BERTI, 2018) images. Both cases had the same air mass flow 0.066 kg/s with holes with 4 mm but two pressures 100 bar and 60 bar, case 1 and case 2 respectively. Thus, the best option is to select is the PP4-02 case (Table 7), because the results presented from PTV will be compared with (BERTI, 2018) and (TODARO et al., 2020) work. Additionally, as presented by (BERTI, 2018) by comparing PP4-01 and PP4-02, the velocity distributions are observed to be similar throughout the temporal evolution, and the difference lies in the acceleration magnitude, such as lower pressure gradient was imposed between the inlet and the spray plumes, as a result, the velocity

magnitudes at images were lower near injection tip due to this acceleration decrease (BERTI, 2018).

Table 7: Configuration selected for this work and their main parameters for air spray analysis.

Case PP4-02	Air mass flow [kg/s]	Injection Pressure [bar]	Reynolds Number []	Integral length scale (From inlet) [mm]
	0.06568 ± 0.00081	60 ± 3	4.22×10^4	3.5

From all studied cases, the acquisition rate was 8000 Hz and interframe time interval equals to 20μs. From each case, the images were recorded in 17 sequences with 15 injection events, which has 255 sprays injection cycles under the same condition and 14001 images from each injection event sequence (BERTI, 2018) (TODARO et al., 2020). All images were recorded as a *pixel* matrix of 360 $\times$ 512 pixels, which is 20.4 $\times$ 29 mm, with grayscale values and 12 bits. The spatial resolution of the system was 59μm/pixel. The *spray* has an axisymmetric geometry, so the left side was selected to make the recording. The representation is presented by the Figure 45.
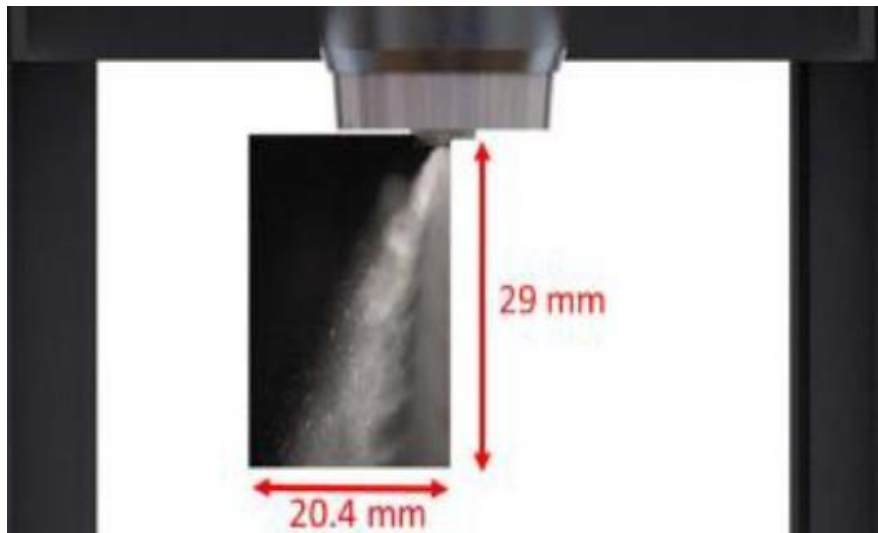
Figure 45: Air-spray flow field visualization by the recording of (TODARO et al., 2020).

4.3   PTV measurement analysis

The PTV technique has two types of errors that affect significantly the results. First, the particle accelerations due to either change in particle direction or speed can affect the accuracy of particle velocity measurements. Second, errors in particle locations can affect particle velocity measurements (DABIRI; PECORA, 2019) (FENG et al., 2011). The first step in processing PTV images is the identification of particle images for 2D or 3D experiments. So, for improvement of tracking techniques it is necessary after the recording a pre-processing for each time t for particle images. This pre-processing process is used to improve the quality of particle images and ease their detection and tracking by the algorithm (LACASSAGNE et al., 2020). The method is proposed to improve the sensitivity (number of detected particles) and selectivity (only particles detected) of the overall process.

As the objective of the DI multi-hole injectors are designed to produce compact and fast sprays, all the energy scattered by the spray density showed to be a challenge factor. To overcome this, (BERTI, 2018) proposed optical filters for two-phase PIV to express a combination of laser light intensity, dye concentration and camera aperture. A combination of those factors should allow enough energy to excite the fluorescence camera sensors, but at acceptable levels for the camera that registers the spray Mie-Scatteting (BERTI, 2018). These conditions demand filters with high performance on the rejection band, especially the longpass band filters that could attenuate significant laser energy. In this case, a set of longpass filters was selected. This set was designed to reject most laser wavelength energy by reflecting on a dichroic filter. The residual unwanted energy is filtered by the absorption filter sequence. The first filter, Brightline[®] Di02-R32 from Semrock Inc, is a dichroic beamsplitter with an optical density (OD) of 6 on the rejection band and cut-off wavelength of 532 nm. The angle of incidence is specified by the filter manufacturer. The next filters are longpass absorption filters where the sequence is: RazorEdge[®] LWP Filter with optical density of 5 and 532 nm wavelength from Semrock Inc, longpass optical density of 4 and 570 nm wavelength generic filter and longpass optical density 3 and 570 nm wavelength generic filter. The illustration of the filters can be seen in Figure 46. It is recommended to read the (BERTI, 2018) work for better knowledge about the light scattering filter used in the experiment.
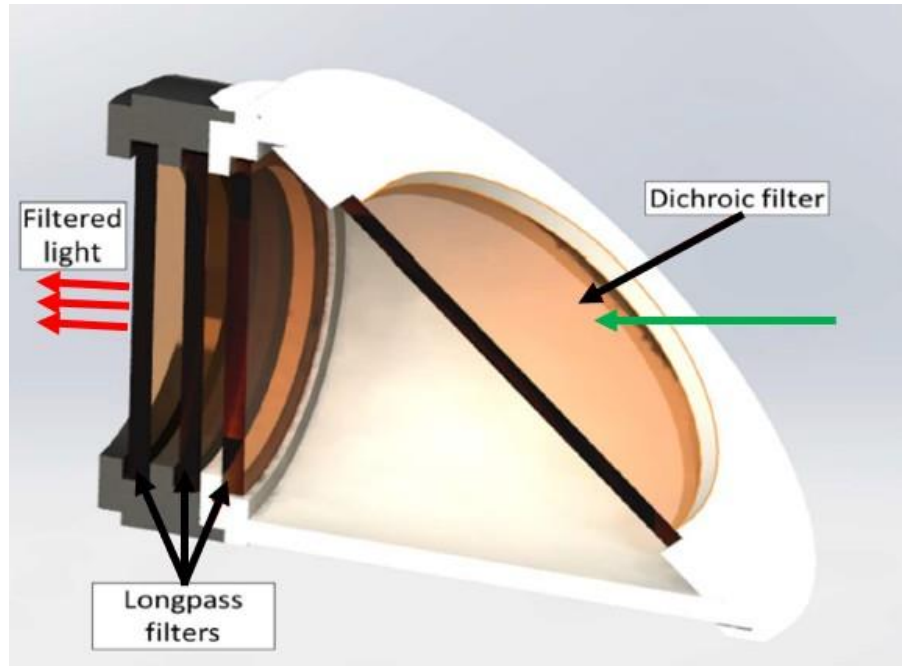
Figure 46: Illustration of the filtering assembly section view. Adapted from (BERTI, 2018).

However, the results showed that, even with optical filters, the intensity registered showed to be highly heterogenic and has high noise levels for 100 bar sprays. The high intensity of light scattered represent a wide amount of counts intensity in different levels, this can be seen in the Figure 47. (TODARO et al., 2020).
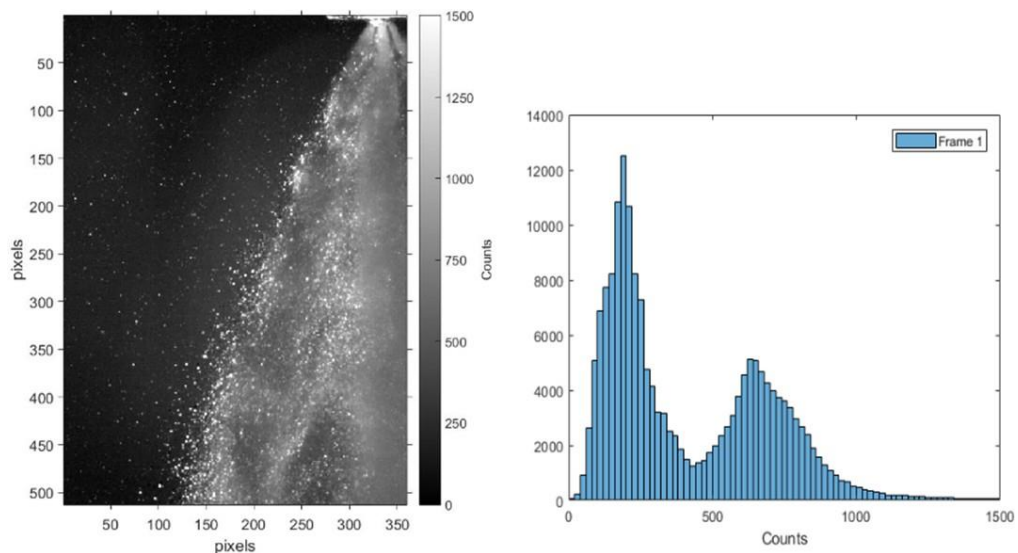
Figure 47: Primary spray image and histogram of an instant with 100 bar pressure. Adapted from (TODARO et al., 2020).

On the other hand, the selected case, 60 bar, the image was found out to be less

heterogenic than the 100 bar case was run. The image and the histogram in the Figure 48 shows that the image turns quite darker, the histogram resembles a log-normal graph.
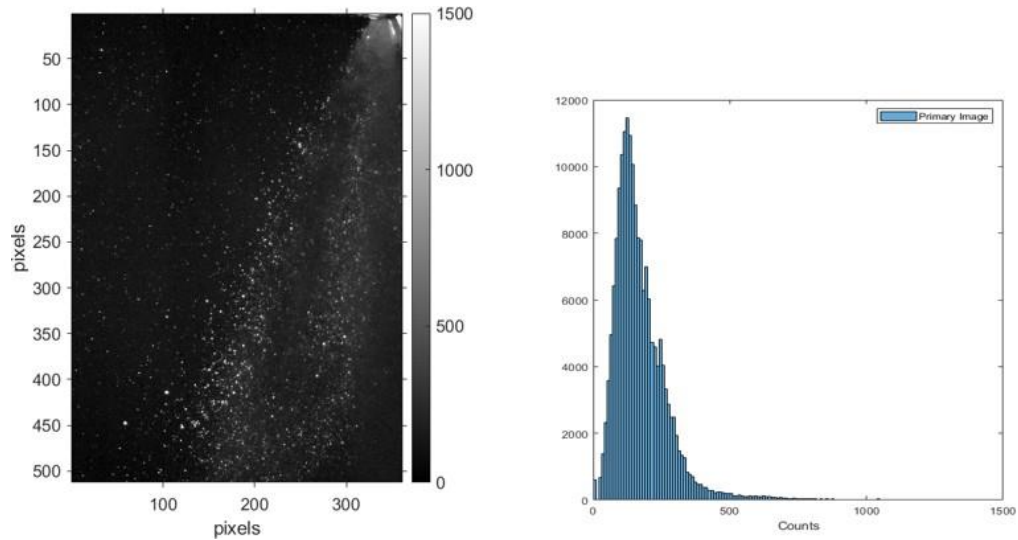
Figure 48: Primary spray image and histogram of an instant with 60 bar pressure.

The fluorescence tracers had lower concentration and less scattering intensity. Also, the raw image has significant noise and low particle identification quality, this can be seen in the comparison between a low quality primary image and a pre-treated image Figure 49. Thus, a pre-processing routine must be necessary and this is motivated by PTV improvement and with a quality identification and matching of particles. The quality of the particles consists in a high contrast of particle images over the background, which should have homogeneous distributed intensities for good SNR to the primary vector field (TODARO et al., 2020).
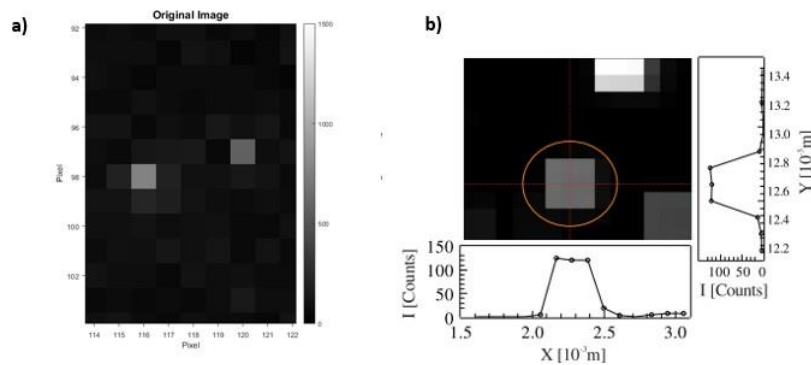
Figure 49: a) Original raw image (lower quality) b) Pre-processing particle image (higher quality). Adapted from (MOURA, 2017).

4.3.1   Pre-processing

The first pre-processing step is the background noise removal, this procedure removes static noise caused by background recording. Everything that stays stagnant in the image, such as light reflections from stationary objects, is assumed to be a source of disturbance and should be removed by subtracting the second frame of the image pair from the first frame. (HONKANEN; NOBACH, 2005). The images acquired by (BERTI, 2018) had a background removed by averaging the intensity fields for numerous samples and subtracting it from the original images. The procedure was performed in the Dynamic Studio ® software - Dantec Dynamics. The Figure 50 shows an example of this background subtraction process.
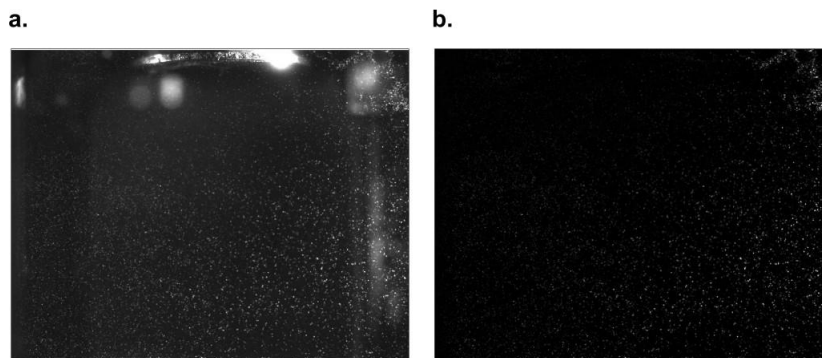
Figure 50: Background subtraction pre-processing. a) Recorded image. b) Resulting image after background subtraction. (BERTI, 2018).

After the background subtraction, in order to achieve better characterization of the particles and reduce the noise of the image, a pre-processing procedure strategy proposed by (TODARO et al., 2020) as Beta pre-processing procedure was made. Even though the algorithm chosen deal properly with high density particle images, it is sensible to select better particles to represent the flow field, so the pre-processing has an utmost impact in the results.

4.3.1.1   Beta Pre-processing

The main objective of this pre-processing step is to simultaneously remove the scattered light noise from the spray and maximize the contrast of the image. Only spacial filters were used for this strategy and a simple numeric procedure was made. The global strategy of the pre-processing can be seen in the Figure 51.

The first intervention is a Root Mean Square (RMS) spacial filter applied with the

main objective to remove the noise and to remove images of particles with a lower diameter from the recommended to ensure better results. The RMS filtering makes use of base standard deviation, which was applied in all the spatial domain of the primary images, considering 3×3 *kernel*. The equation that rules this filtering is shown in the Equation (4.1) (TODARO et al., 2020). The results of this first filtering can be seen in the Figure 52.

$$RMS(i,j) = \sqrt{\frac{1}{N^2} \sum |I(i \pm k, j \pm k)|^2} \qquad (4.1)$$
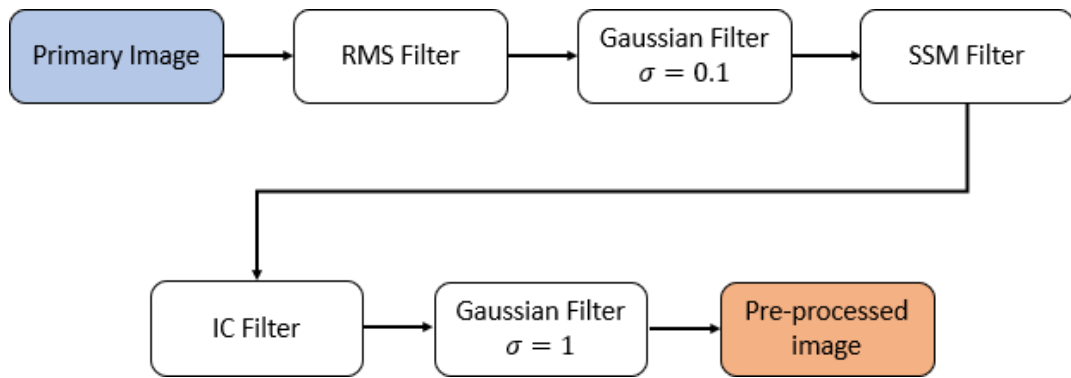
Figure 51: Global overview of the Beta pre-processing.

Figure 52: Gas-phase image after RMS filtering in an instant of the spray at 60 bar pressure.

After the RMS filtering, a Gaussian filtering was applied as described in the Figure 51. The objective here is to improve the shape of the particles, therefore it was considered a standard deviation of 0.1 *counts* and *kernel* of 3×3. The Gaussian filter applied

on the images tends to blur the image in order to preserve lower frequency regions and smooth those higher frequencies (TODARO et al., 2020). It is used to reduce the noise and preserve the homogeneous regions. However, it does not remove efficiently the background light (MOURA, 2017). A Gaussian function for 2-D derived from radially symmetric form as follows (SOLOMON; BRECKON, 2011).

$$f(x, y) = \frac{1}{2\pi\sigma^2} exp \left(-\frac{x^2 + y^2}{2\sigma^2} \right) \tag{4.2}$$

The x and y refers to the pixel position on the adopted *kernel* of matrix size $N \times N$. σ is the standard deviation of the Gaussian function. This function has a rather special property which makes it very convenient for the frequency-domain analysis of filters (SOLOMON; BRECKON, 2011). It is important to mention that the *kernel* size does not have much influence on the smoothing result, however, the standard deviation has an utmost importance for the results. An example of the Gaussian function application is shown in the Figure 53.
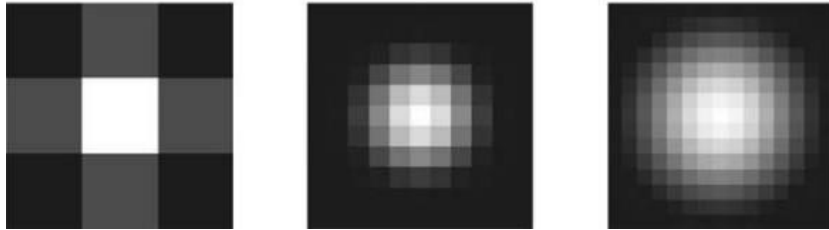
Figure 53: Gaussian filtering kernels 3×3-(N = 3) σ = 1, 11×11-(N = 11) σ = 2 and 21×21-(N = 21) σ = 4, respectively. (SOLOMON; BRECKON, 2011).

After the application of the Gaussian filtering, (TODARO et al., 2020) proposed to use the Subtract Sliding Minimum (SSM) to ensure substantial contrast between the particles and the background. This filter was applied on all the matrices of a *kernel* of 50×50. This filter operates with strongly dependence on the neighbors and their connectivity. The connectivity is made selecting the four pixels (up, down, left, right) from the chosen pixel as a 4-neighbour for the calculation. Therefore, an 8-neighbor means the eight pixels that surrounds the selected pixel, identified as a 3×3 matrix (SOLOMON; BRECKON, 2011) (TODARO et al., 2020).

The filtering operation consists in selecting the main parameters as the $N \times N$ matrix for the pixel (i, j) and the addition for the sliding as k, indexed for operations as ($i \pm k, j \pm k$).

The SSM uses directly the Window Sliding technique, and it consists in subtracting from a sliding window $N \times N$ the lowest value of intensity between the matrix on the Region Of Interest (ROI). This technique elevates significantly the contrast of the elements and remove the background noise. However, it can increase the difference between particle intensities (MOURA, 2017) (TODARO et al., 2020). To overcome this, (SHAVIT et al., 2007) it is suggested to establish a limit for intensity to turns zero the intensity of a pixel below this value. The results of the procedure on the images after the Gaussian filtering is shown in the Figure 54.
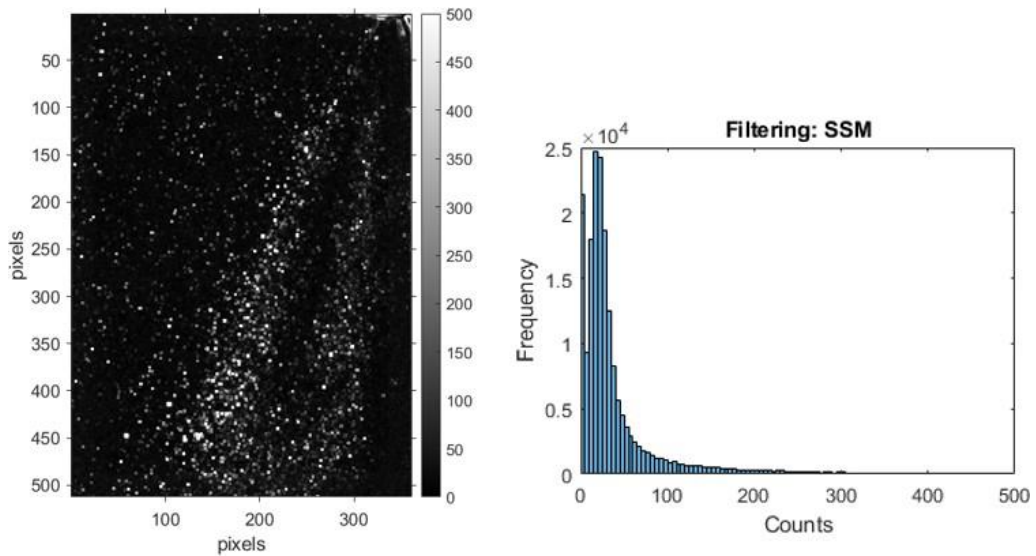
Figure 54: Gas-phase image after SSM filtering in a instant of the spray at 60 bar pressure.
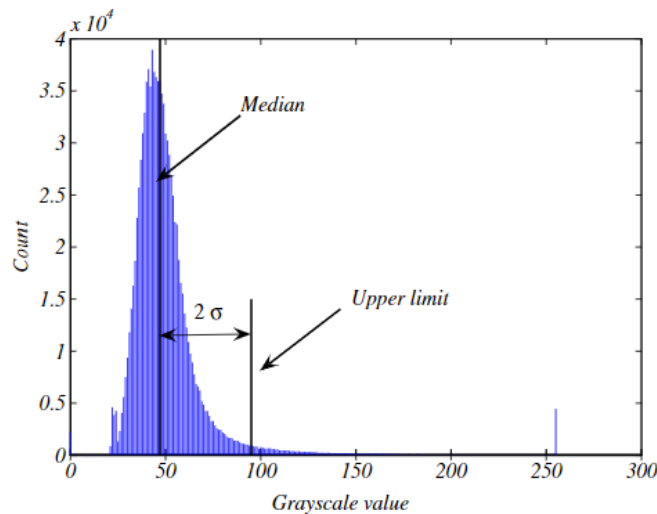
Figure 55: An intensity histogram for a image treated by (SHAVIT et al., 2007) and its grayscale median showing the upper limit described by the equation (4.3) used for Intensity Capping. (SHAVIT et al., 2007).

After the SSM filter, the Intensity Capping Method was applied as a pre-processing strategy to tackle the Bright Spots (BS) and do not affect the particles, which are good for processing and post-processing. This strategy developed by (SHAVIT et al., 2007) propose an upper intensity limit, as I_{max}, for all pixels that are described by the two-frame selection. The equation becomes

$$I_{max} = I_0 + n.\sigma \qquad (4.3)$$

Where I_0 and σ represents the median and the standard deviation of the intensities in the image, respectively, and n is specified for the method used (SHAVIT et al., 2007) (TODARO et al., 2020). An example of the description can be seen by the Figure 55 where the saturated pixels have a value of 255.

As a result from SSM filtering, the contrast becomes too intense, so, the IC was used to reduce substantially the generated intensities and the participation of the bright spots on the particle identification and the matching process. Moreover, the outlier detection strategy and elimination of spurious vectors becomes more efficient. The results of the IC method applied to the spray images becomes as follows by the Figure 56. It is worth to notice the saturated pixels with a value of 185, approximately.
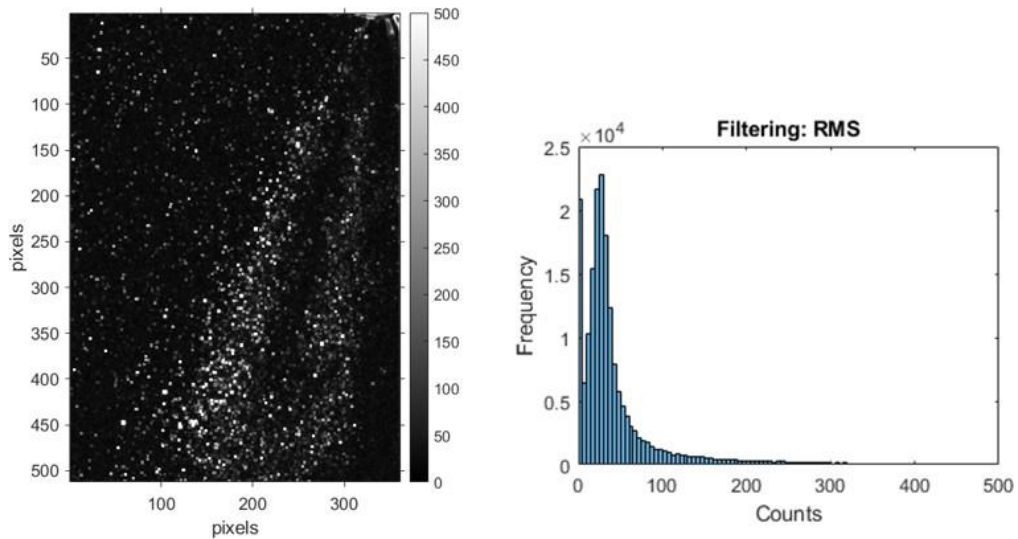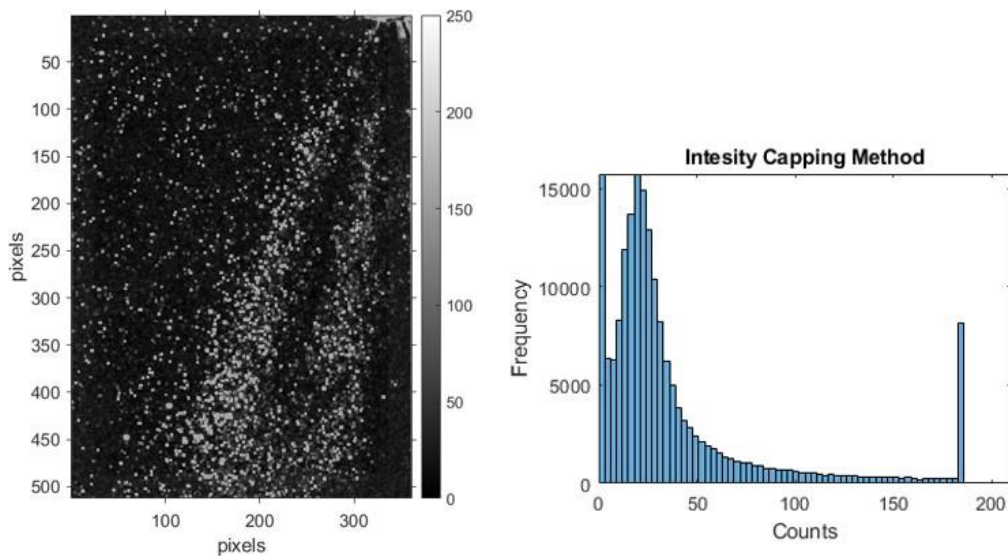

Figure 56: Gas-phase image after IC filtering in an instant of the spray at 60 bar pressure.

Finally, a Gaussian filter was again applied, with the same objective as described before, however, this time the standard deviation was used as 1 count. As a result of this filtering, the pre-processing process is finished, and the final results can be seen in the

Figure 57. Also, a sequence of the histograms shows the pre-processing at each image, and it might be seen that the grayscale levels are substantially reduced and a homogenization of their intensity. The Beta pre-processing do not suffer from high grayscale change of each step, because their objective is to focus on the shape of the particle rather their intensity. However, a good background noise reduction was noticed (TODARO et al., 2020).
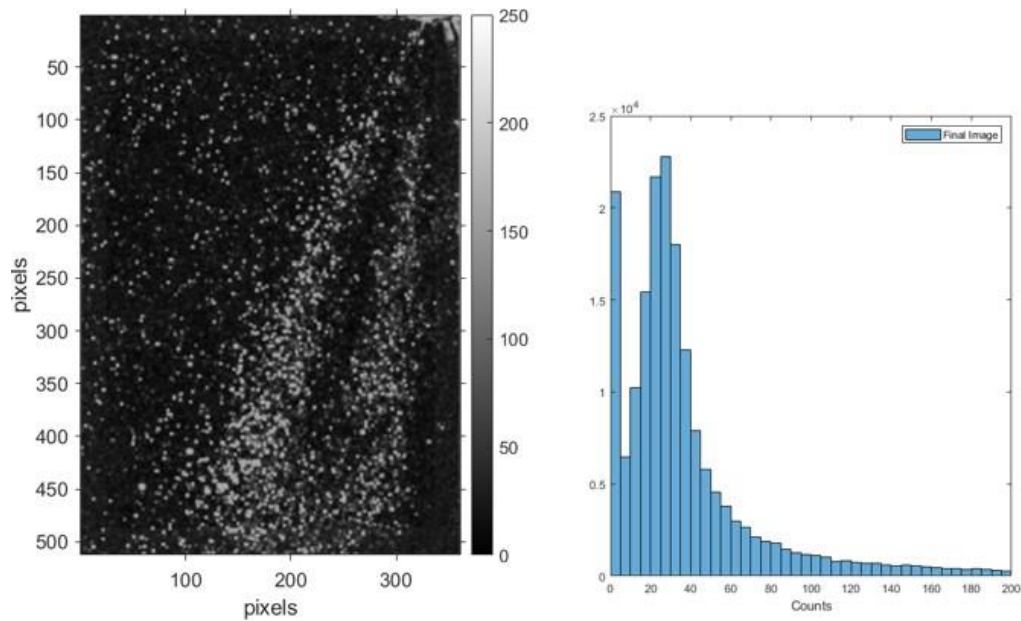
Figure 57: Gas-phase image after the last Gaussian filtering in an instant of the spray at 60 bar pressure.
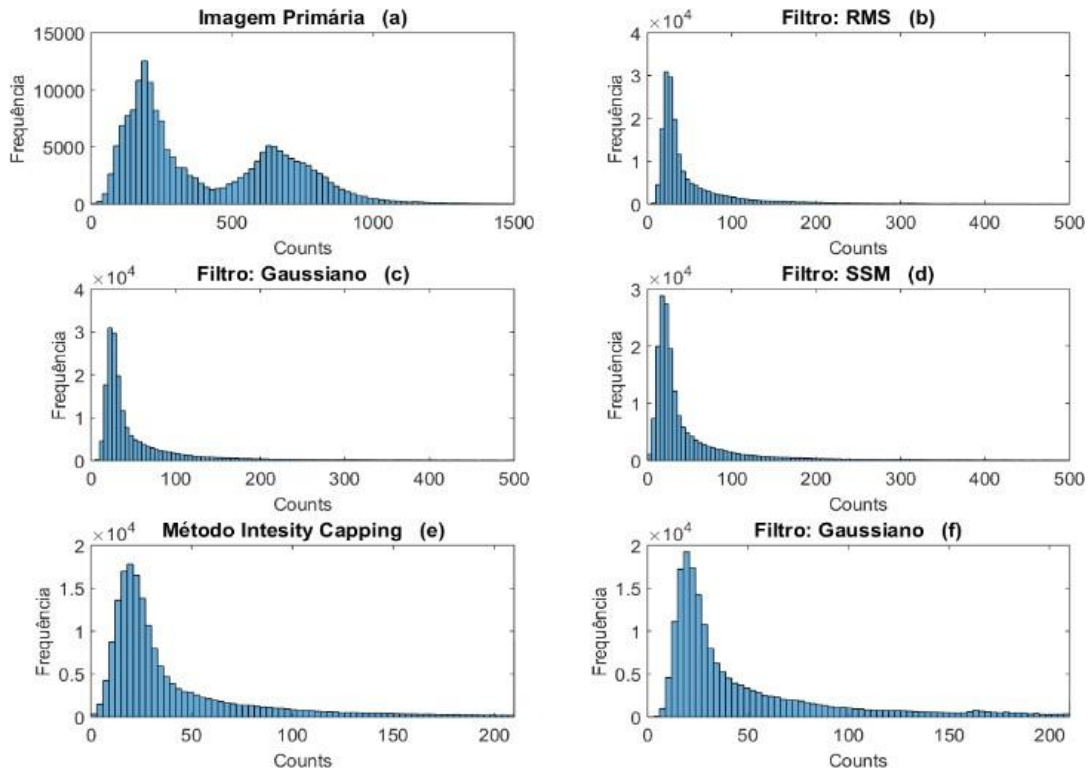
Figure 58: Histogram sequency of each step of the Beta pre-processing rotine made by (TODARO et al., 2020) as comparison with those obtained. First frame processed. a) Primary Image; b) RMS filtering; c) First Gaussian filtering $\sigma = 0.1$; d) SSM filtering; e) IC filtering; f) Last Gaussian filtering $\sigma = 1$.

The logical sequence to provide the Beta pre-processing turned out to be appropriate for PTV analysis by the results obtained from the histogram sequence steps, as shown by Figure 51. A comparison between the final result, Figure 57, was made with other PTV pre-processing analyses. The results were very similar to those in Figure 59. On PIV histograms, it is common to observe two columns of intensities, similar to Figure 58a. On the other hand, the PTV shows low particle counts on higher grayscale intensities because the goal is to have lower particle densities. It shows that the Beta pre-processing achieved the objective to provide a better image quality to process the tracking algorithms.

The Beta pre-processing routine was made with the recommendations done by (TODARO et al., 2020) and showed similar results for 60 bar pressure surrounded air particle image captures as shown in Figure 58. The result was a satisfactory particle size with a clear separation between particle and background, and low signal noise.
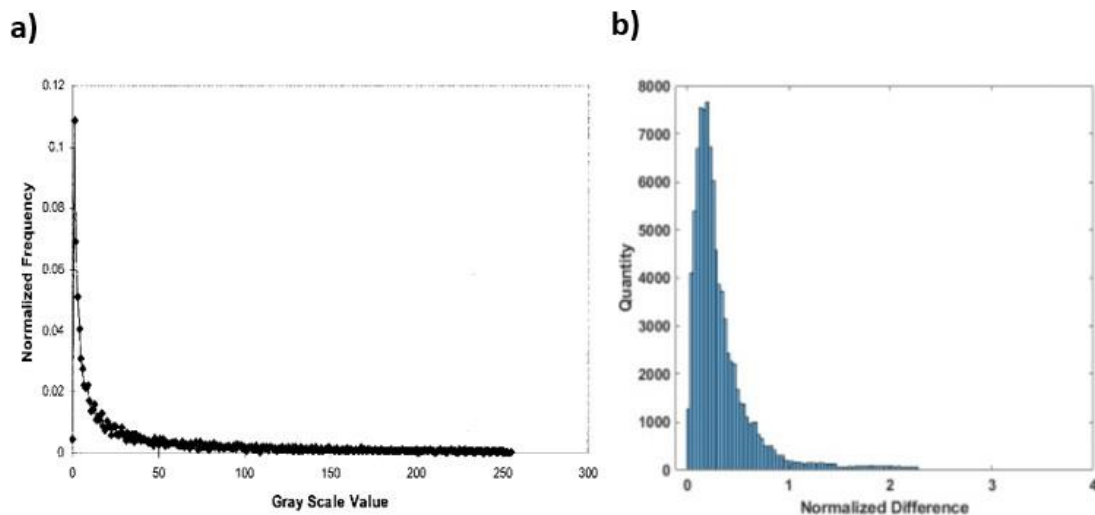
Figure 59: Histogram comparison between grayscale intensity values and frequency of those values from different works. a) Histogram of hyperbolized image. Adapted from (DELLENBACK et al., 2000). b) Histogram of normalized differences after a Gaussian post-processing for particle tracking velocimetry. Adapted from (TANG et al., 2019).

4.3.2   Algorithm

The algorithm used for this step of the image processing is an open source MATLAB$^{®}$ program called Part2Track (JANKE et al., 2020) which provides two sources of two-dimensional PTV algorithm, time-resolved processing and double frame image evaluation. The double frame recording techniques used for PIV are the same as used for the PTV algorithm. Originally, PTV was only used for sparsely seeded flows, however, over the time, PTV algorithms were developed to handle large amount of particles. The algorithm package provide an easy and fast processing of the image data and consists in two main functions. First, a routine to convert the image data into final scattered velocity field. Second, a collection of various post-processing functions for velocity data analysis. The PTV does not have the same limits of the PIV for resolution, instead, it could enhance the spatial resolution and increase the data yield per image if it has a high SNR and not too much overlapped particle images (KAHLER et al., 2012). A schematic overview of the main processing script is given in the Figure 60.
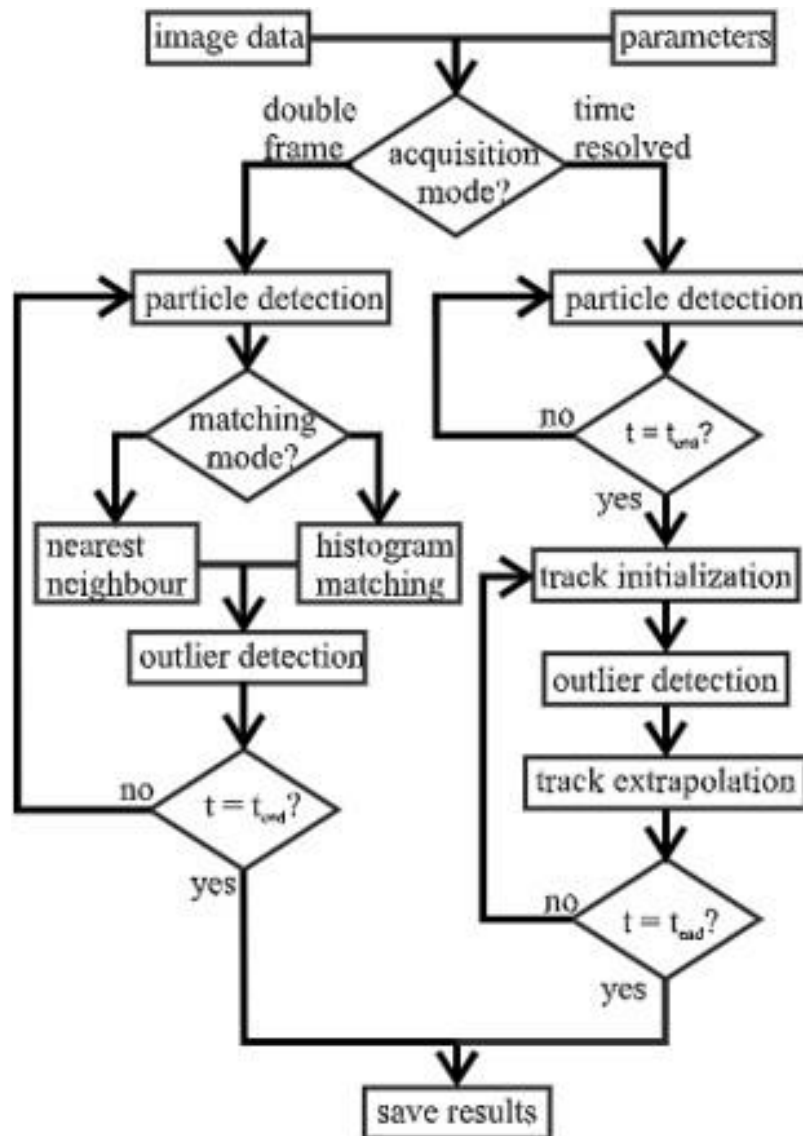
Figure 60: Schematic representation of the processing routine. Adapted from (JANKE et al., 2020).

For the case of double frame data, a method capable of handling higher particle densities was adopted from (FUCHS et al., 2017), as described by the subsection 3.3.5.4 (histogram matching), and implemented (JANKE et al., 2020). The sub-pixel accurate detection of the tracer particles is achieved by a Laplacian of Gaussian image filtering technique, followed by a Gaussian interpolation of the particle peak intensities. This particle detection method is the "blob detection" adopted from the (HEYMAN, 2019) and described in the subsection 3.3.4. During the iterative matching process, a universal outlier detection described in the subsection 3.3.6 and adopted to work with scatted velocity data (PATEL et al., 2018). The selected method to interpolate the scattered data is the Gaussian-weighted binning, which consists in weighting the velocity contributions

to the statistical moments according to their distance with respect to the center of the interrogation spot.

The parameters involved in the algorithm were divided in two parts. First, important information about the experiment, such as the image acquisition mode, which is double frame for the present study, the resolution of recorded images, the number of double frame pairs, the time separation, the linear conversion scale mm/px and the pre-defined image mask. All these parameters can be seen Table 8.

Table 8: Image recording parameters.

Recording Parameters	
Image Acquisition mode	Double Frame
Camera Resolution [pixels]	512×360
Number of Injections	17
Time Separation of Image Pairs [s]	$1.25.10^{-4}$
Mapping Scale [mm/px]	0.0566

Second, the parameters control the displacement calculation, for example particle detection parameters like size and brightness, and the particle matching such as: method, field of search and size of particle neighborhood, the outlier detection, like threshold for validity and noise, and the multi pass approach (number of iterations), shown in the Table 9.

Table 9: Double-Frame processing and outlier detection parameters.

Double Frame Processing Parameters	
Particle Size [pixels]	3×3
Particle Intensity [grey scale]	95
Algorithm for Particle Matching	Histogram Match
Field of Search [pixels]	35
Neighbours for Displacement Detection	15
Outlier Detection	
Number of Neighbours for Outlier Detection	50
Threshold for Outlier Detection	2
Estimated Noise Level of Measurement	0.05
Number of Iteration for Outlier Convergence	3
Number of Steps to Increase Field of Search	3

The (JANKE et al., 2020) work also shows the results of the algorithm comparing with synthetic data using Taylor-Green-Vortex for the simulated flow and for double frame a PIV measurement campaign covering the flow within the conductive human airways. The results for the synthetic flow can be seen in the Figure 61.

At least 90% of all detected particles were matched validity in a range of $ppp = 0.025$ to $ppp = 0.05$. The algorithm was tested against a well established, commercial software and could prove comparable performance in the investigated case selected by the study (JANKE et al., 2020). It offers a broader choice of already available software tool, such as openPTV, PTVlab or TracTrac (HEYMAN, 2019).
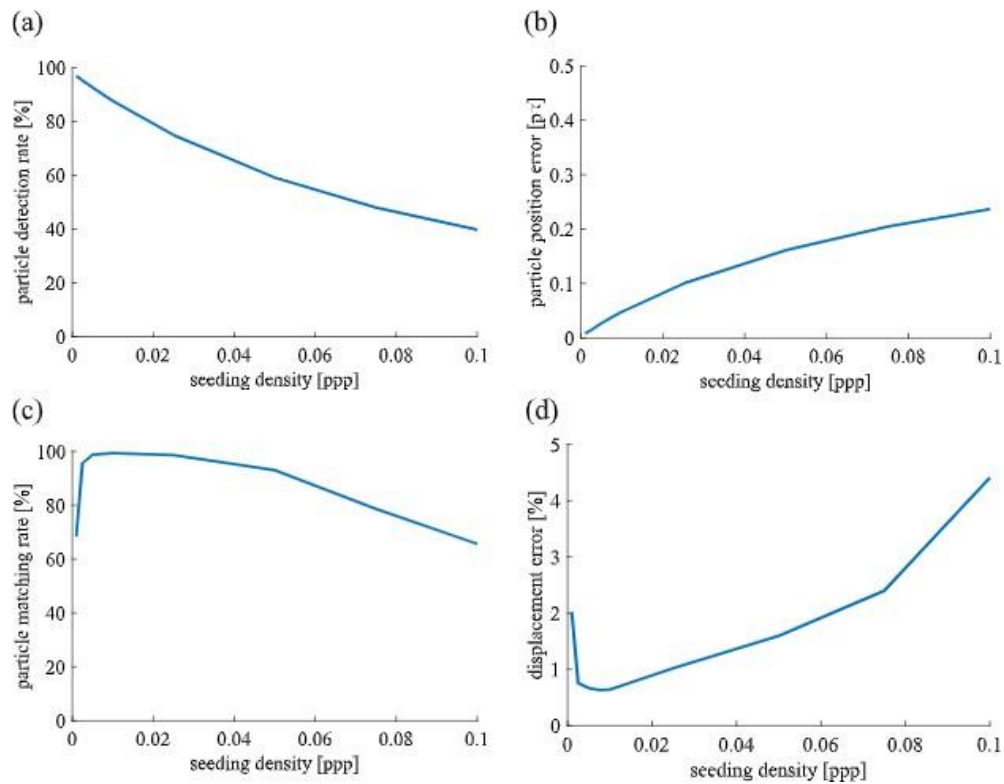
Figure 61: Results of the synthetic image evaluation. a) Particle detection rate; b) Particle position error; c) particle matching rate; d) Displacement error. (JANKE et al., 2020).

4.3.3 PTV strategy analysis and Post-processing

Here, the primary goal is to provide velocity estimations at discrete, scattered points within a measurement space. As the PIV data is generated on a grid, the velocity gradients can be estimated using finite difference methods as shown in Figure 62.
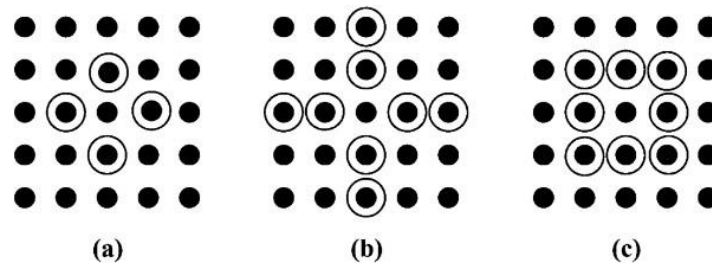
Figure 62: Velocity measurement location used for estimation of spatial derivatives using a) second-order central difference; b) fourth-order central difference; c) eight-point circulation methods. (COHN; KOOCHESFAHANI, 2000).

PTV vectors are typically interpolated for analysis and the post-processing step consists of all routines to convert the image data to the final scattered velocity fields, and they are a collection of functions for a deeper analysis of the velocity data. Also, the outliers detection technique used for this package is described in subsection 3.3.6.

The PTV ensemble of these two approaches for 3D PTV can be summarized by the Figure 63. For 2D, which was the analyzed case made by the present work, the PTV procedure is the same except for the particle identification. The difference between those approaches is the ensemble approach creation (step 4 in Figure 63).
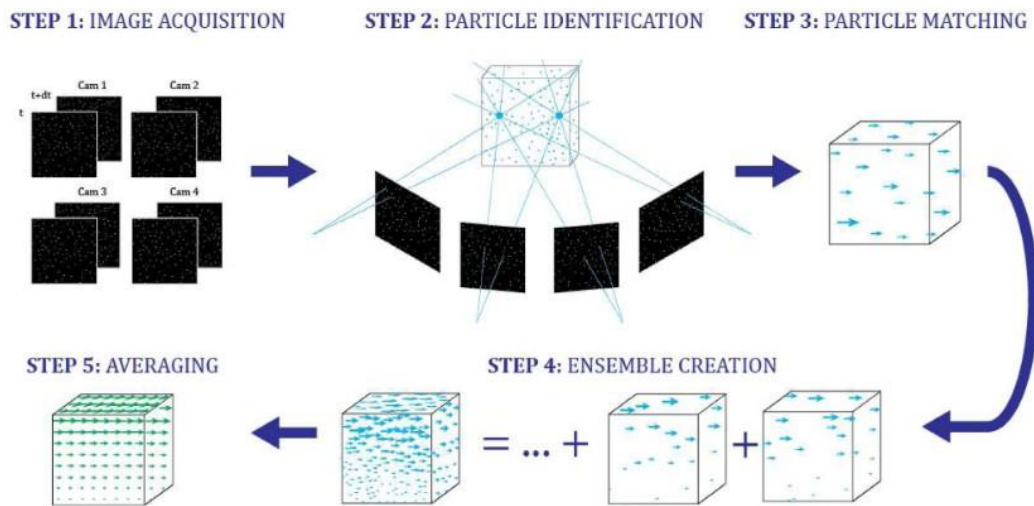
Figure 63: Ensemble PTV process. (AGUERA et al., 2016)

Often the main steps for the post-processing are the validation of the raw data, replacement of incorrect data, data reduction, analysis of the information and presentation and animation of the information. For turbulent analysis it is important to reduce the residual gradient effect allowing to reach higher resolution even with relatively large interrogation spots, therefore retrieving many particles to calculate turbulent statistics. For

the standard ensemble PTV approach, all velocity vectors would have the same weight, resulting in a top-hat filtered mean velocity field as shown in Figure 64.

The ensemble particle tracking velocimetry process is used for resolution improvement, and the binning methods implemented to interpolate the scattered data on a regular grid with adjustable grid sizes and interrogation windows are the Gaussian-weighted binning and the binning based on second degree polynomial interpolators (JANKE et al., 2020) (AGUERA et al., 2016).

The first approach proposed by (AGUERA et al., 2016) and applied in the algorithm by (JANKE et al., 2020) is the Gaussian weighting function, which consists in weighting the velocity contribution to the statistical moments depending on their distance to the center of the interrogation spot. Second order moments are affected by large errors. However, the regions with larger deviations from the mean velocity measurement in the central part of the window are considered with lower weight, thus reducing their spurious contribution (AGUERA et al., 2016). The second approach takes the large amount of particles within the windows and fit these distributions in a polynomial function, for the Figure 64 (AGUERA et al., 2016) selected a second order polynomial. The velocity component is expressed as a second order polynomial, which is a function of the distance to the grid point considered. The advantage of this approach is that second order moments are computed with respect to a locally adapted mean, thus providing precision (AGUERA et al., 2016). Both approaches were compared with a source of error considering the particle local velocities spreading around the mean velocity profile with one interrogation spot and being spatially variable due to an unresolved velocity gradient Figure 64.
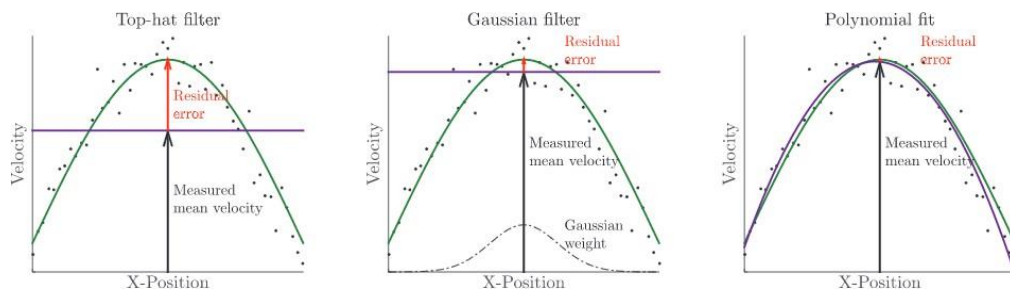
Figure 64: Illustration of sources of error due to residual velocity gradient within an interrogation spot. ( )Particles velocities; (-)exact mean field; (-) filtered mean field. (AGUERA et al., 2016).

A schematic view of the process of post-processing step was summarized in the Figure 65. The fluid flow visualization could be any dynamic visualization of the fluid that uses the vector field. In this work, the mean velocity field will be represented and used for

comparison with PIV previous data.
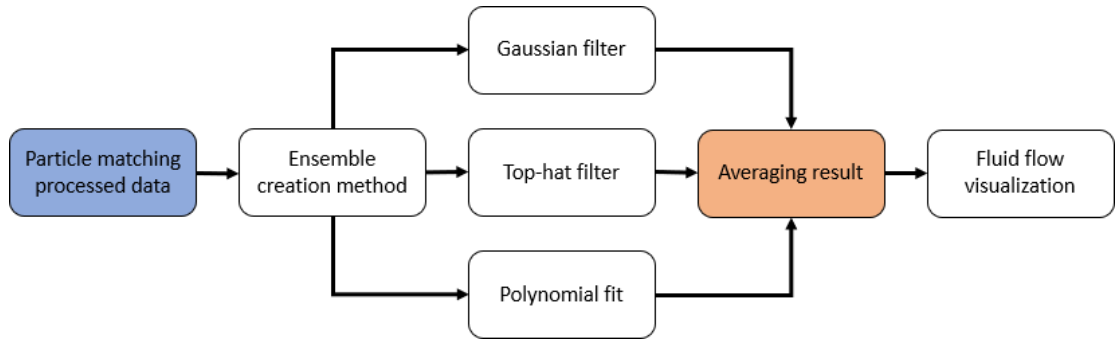
Figure 65: Post-processing schematic view.

5   RESULTS

This chapter has the first goal to present the results of the PTV analysis, an investigation of the air-spray interactions, the fluid dynamic of the air, and their turbulent characteristics. A sequence of spray development after the pre-processing was made. The velocity field and velocity intensity, U, of the flow shows the main characteristics of the air interaction with spray development. The vectors U were separated into two components u and v, horizontal and vertical, respectively. Due to color restrictions, velocity profiles were selected to describe the flow in detail. The main results of the ethanol injection were compared with PIV and showed similar results. Some specific characteristics of the flow could only be seen with PTV analysis. The second goal of the chapter is to present a peak locking analysis, where it demonstrates the quality of the results obtained with the PTV technique.

5.1   Air-spray interactions and air dynamics

The present section has the goal to analyze air-spray flow. A previous result obtained from the PTV analysis for a fully developed spray event at IESC is shown in Figure 66. This result is a vision of the entire spray event and an ensemble of all vector fields. The results were obtained from events of ethanol injection, where its time of injection was near 3 ms. All the results produced were a consequence of a temporal evolution of 17 spray injections, where the interval of each spray was 100 ms. The mean velocity field of the 17 injections allowed to mitigate local instabilities that could compromise the results. The vertical component corresponds to the vertical orientation at the end of the injector. Also, the horizontal is orthogonal to the vertical orientation, where the vertical and horizontal axis are respectively orientated down and to the right of the picture. The comparison between the 66a and 67, which is an example of a result obtained by (TODARO et al., 2020), shows that the PTV vector field similarly represents the air surrounding the spray. Both could not precisely show the spray droplets' velocity for the effective number of particles, in PIV, and a high concentration of particles, for the PTV. However, both

techniques represented the air flow velocity field with the same magnitude. The high number of vectors per grid inside the spray can be seen in Figure 66b, showing that the spray contains most of the particle concentration.
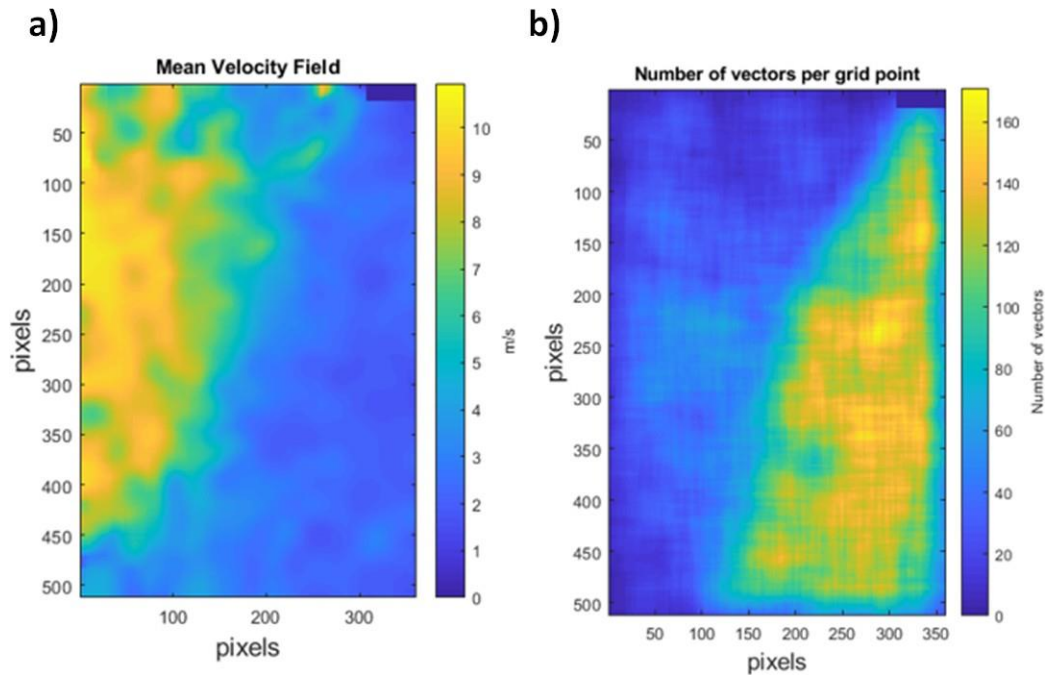
Figure 66: Measured results from PTV analysis using absolute velocity magnitude in a full developed spray injection at IESC. Injection pressure of 60 bar and 6 ms time exposure. a) Mean velocity field. b) Number of vector per grid point.

The differences between the air particle density and the spray droplet density are significant. The figure 66b shows the number of vectors found in the spray regions. The number of vectors inside the spray due to elevated number of particle per pixel are higher for all spray development stage. The two defined regions makes the shear layer a challenge region due to the higher gradient of particle difference. The parameters selected to investigate the inlet air movement makes the particle images start to overlapping and therefore becomes more difficult to distinguish between different particle images and determinate their location. The PIV analysis of the shear layer presented better results as compared to the PTV, since it could be found more reliable values of air movement inside this noisy region.
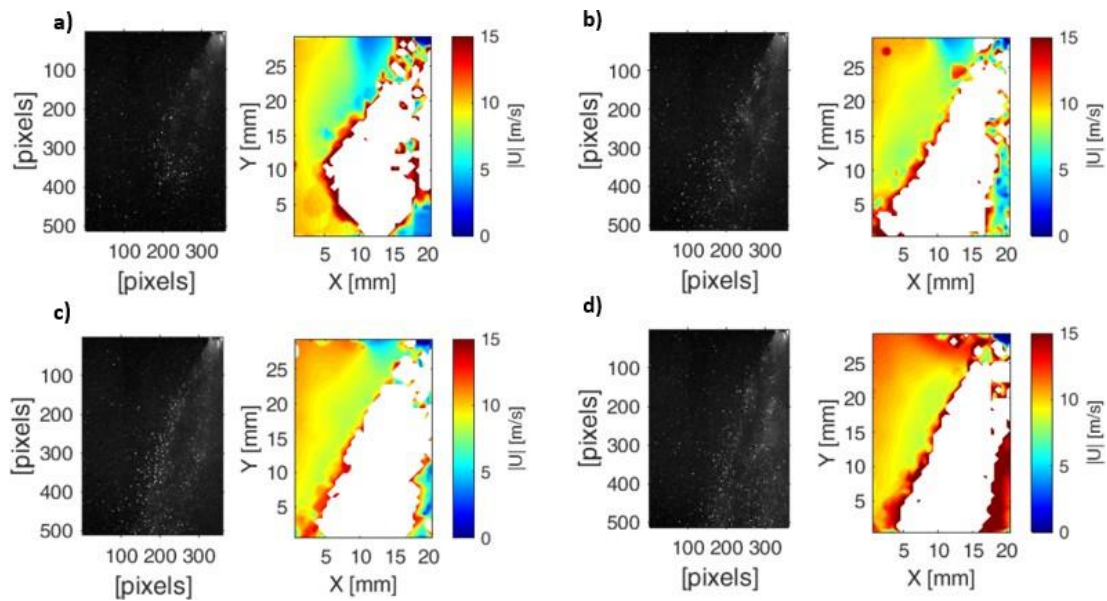
Figure 67: Comparison between the velocity over time in a full developed spray injection at IESC with PIV analysis from (TODARO et al., 2020). a) Injection time 0.400 ms b) Injection time 0.800 ms c) Injection time 1.200 ms d) Injection time 2.677 ms. Adapted from (TODARO et al., 2020).

The velocity intensity in Figure 66a shows the influence of the inlet air injection in the spray development. Without spray, the velocities of the inlet air injection were analyzed and shown in Figure 68a. It shows the recirculation zone below the injector tip and the velocity distribution over the chamber with the conditions of a flow around a bluff body. The chamber had not a constant velocity distribution, but two different regions. First, a recirculation structure showed in blue color and circular lines in Figure 68a. This recirculation zone was a consequence of regions of lower pressures than the pressure of the flow. Secondly, an irrotational flow where the velocity field was mainly downstream in the chamber. A turbulence intensity generated by the perforated plates can be seen in Figure 68b. The turbulence is more sensitive to the change of plate set than the velocity distributions. Therefore, fluctuations of the velocity magnitude were expected even outside the spray injection development. The air flow parameter is controlled by the air mass flow rate. The air mass fluid flow was 0.06568 kg/s for the analyzed images of the spray injection and the stationary conditions shown in Figure 68.
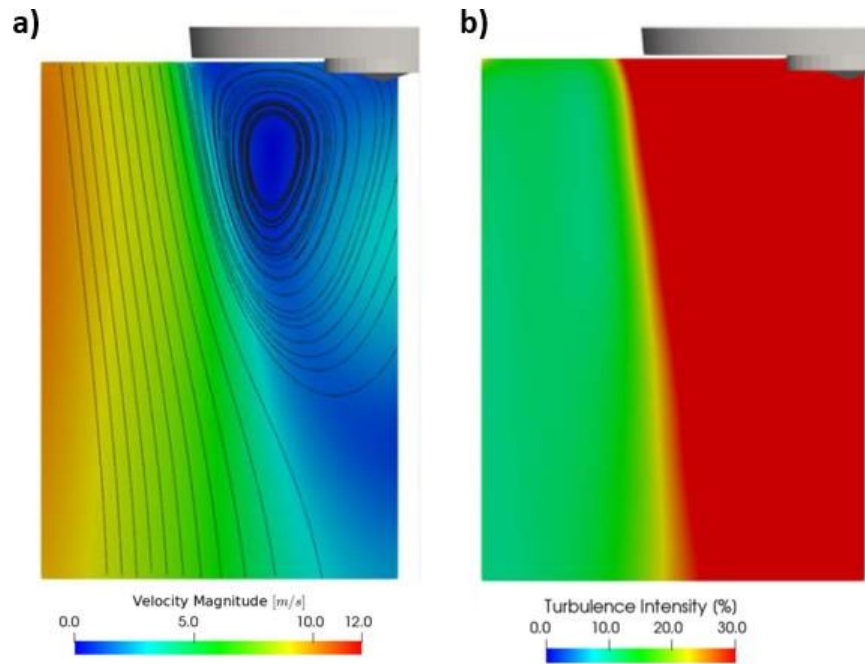
Figure 68: a)CFD simulation of air flow inlet mean velocity field of the stationary conditions for the PP4 perforated plates set. (BERTI, 2018). b) Turbulence intensity for *U* distributions for the PP4 perforated plate set. (BERTI, 2018).

The resultant FOV was of 20.4×29 mm^2 or 316×512 pixels, where the mapping scale parameter was 0.0566 mm/pixel. The tip of the injector was hidden to not interfere with the particle identification technique. For the spray development, it is relevant to highlight the shear layer line, which is the line where there is a transition from air movement and the spray droplet.
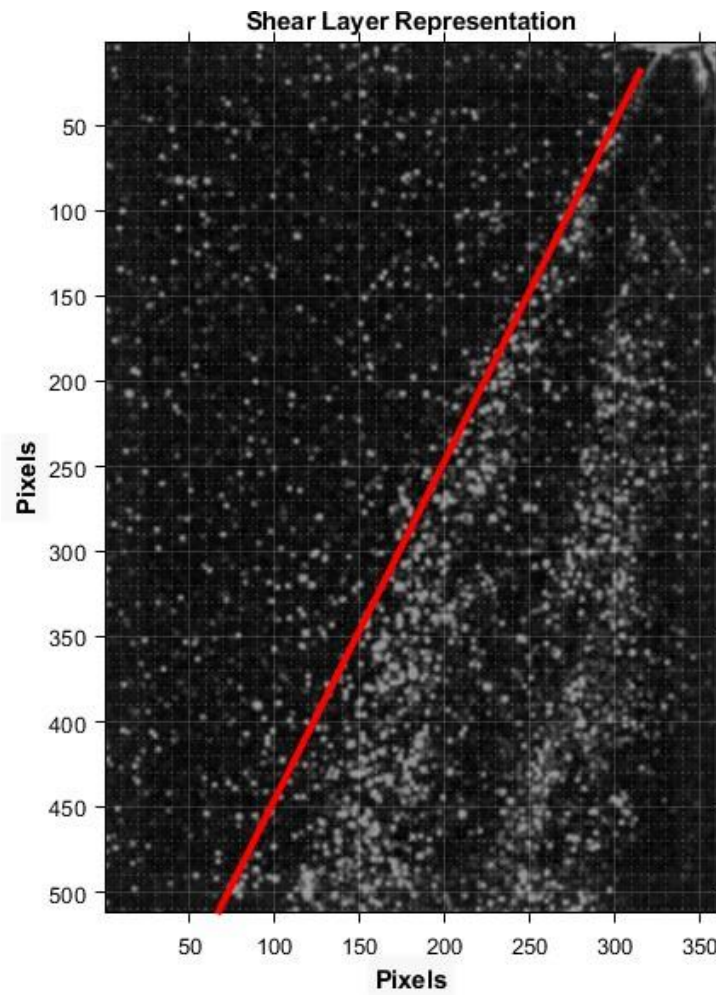
Figure 69: Shear layer of the spray with its representation line.

The shear layer is shown in Figure 69 and, while the particle moves down from the spray tip, the angle of injection makes the droplet moves away from the center line. This cone angle is a characteristic of each spray injector. Table 10 shows the coordinates of the shear layer for velocity analysis profiles.

Table 10: Shear layer coordinates of the spray for specific points over the injection.

Shear Layer Coordinates (Pixels) [mm]	
x	y
300 [16.98]	50 [2.83]
250 [14.15]	150 [8.49]
198 [11.21]	250 [14.15]
147 [8.32]	350 [19.81]
96 [5.43]	450 [25.47]

To compare with the PIV results, different time instants were selected. The sequence of images of the spray development can be seen in Figure 70. It is worth to summarize that the presented velocity field represents the air flow and its interaction with the spray. The air moves into the spray and mixes with the fuel. Before the spray, the velocity field represents features of the stationary condition, where a low-velocity recirculation structure below the injector tip and a constant velocity of the flow field can be seen as shown in Figure 68. The Figure 71a shows the PTV measurement for the stationary condition before the start of injection. It can be seen in the recirculation zone below the injector tip, where the values of the vectors are from -2 to 0 m/s. Also, the flow of the air outside the circulation zone is near the mean velocity magnitude, for the air flow inlet mean velocity field of the stationary condition, calculated as shown in the Figure 68a. Both regions could be seen with the PTV measurement.

The following results comprise three different stages of spray development. First, the liquid was injected and broke the recirculation of the air. This interaction causes a disturbance in the air flow by the energy of the spray injected in the chamber. This injection changes the direction of the vectors and elevates their magnitude. It is noted in Figure 71b to 71c the direction of the air inlet flow changes by the unstable environment of the movement on the tip of the injector. Due to the momentum of the spray, the velocities near the spray tip elevates to nearly 16.4 m/s with a strong vertical component.

The Figures 71d to Figure 71f the spray presents a quasi-steady condition, where the differences between velocity distributions are similar. This condition shows the interaction of the inlet air flow colliding with the spray cone. The spray's momentum elevates the vector magnitudes near the spray cone and changes its direction. Besides, a structure begins to rise to change the air velocity into the spray tip. It was affected by the injection pressure. These structures presented higher horizontal components than vertical ones.

Figures 71g to 71h represent the injection's end, where the air tries to fill the lower pressure left by the spray drag. This zone turns part of the inlet air to change its direction to the center of the injector axis and shows horizontal components. Also, the spray is developing below the image, and the amount of air is moving forward facing the other part of the inlet air flow.

The next timesteps the vector field tends to return to the stationary air injection condition after the injection. The presence of the spray affected near to 10 ms ASOI.

(a) t=-0.125 ms   (b) t=0.250 ms   (c) t=0.375 ms

(d) t=1.250 ms   (e) t=2.500 ms   (f) t=3.125 ms

(g) t=3.875 ms   (h) t=4.000 ms   (i) t=5.750 ms
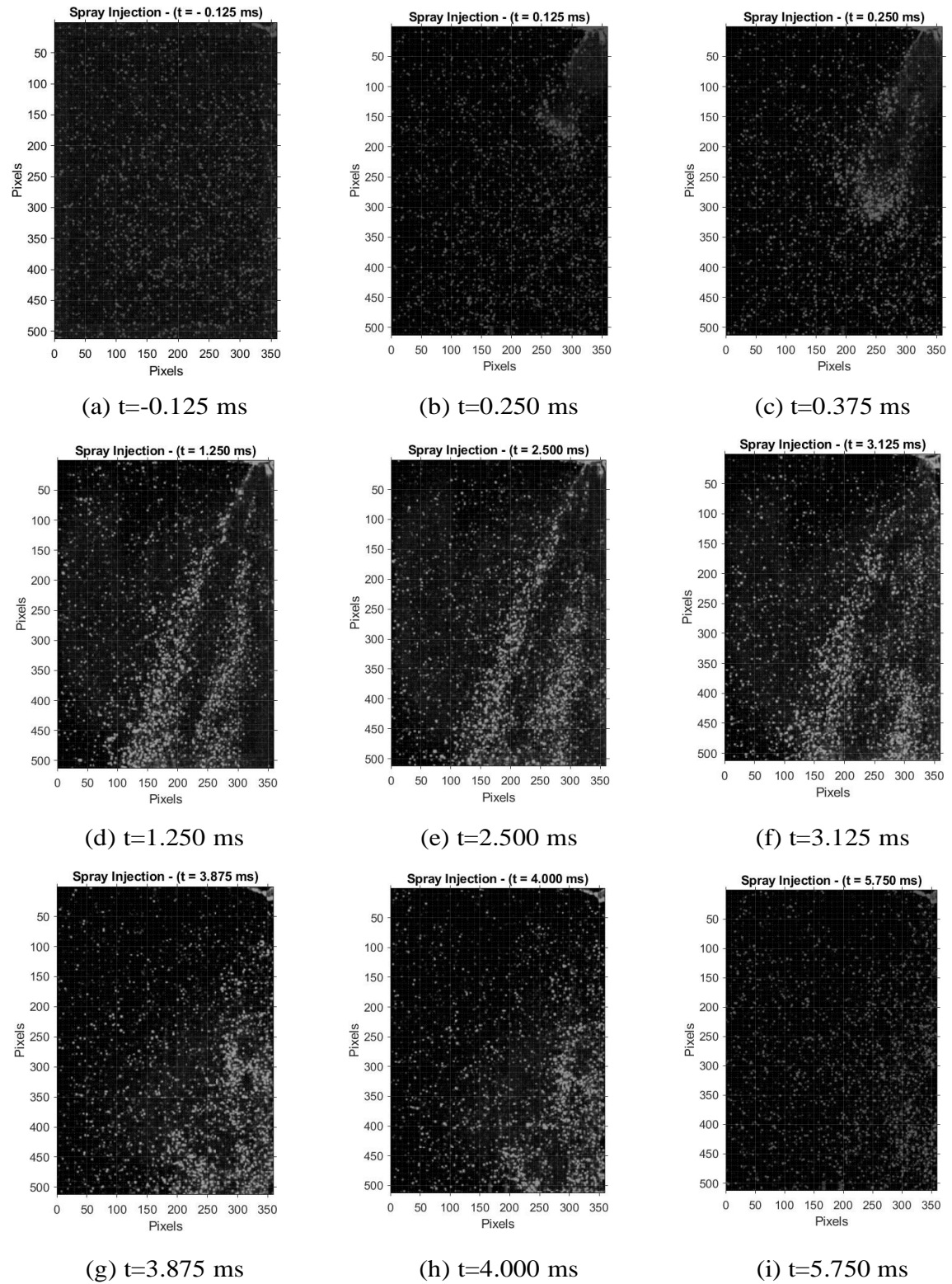
Figure 70: Comparison between Beta pre-processing images with timestep evolution of the spray injection.

(a) t=-0.125 ms (b) t=0.250 ms (c) t=0.375 ms

(d) t=1.250 ms (e) t=2.500 ms (f) t=3.125 ms

(g) t=3.875 ms (h) t=4.000 ms (i) t=5.750 ms
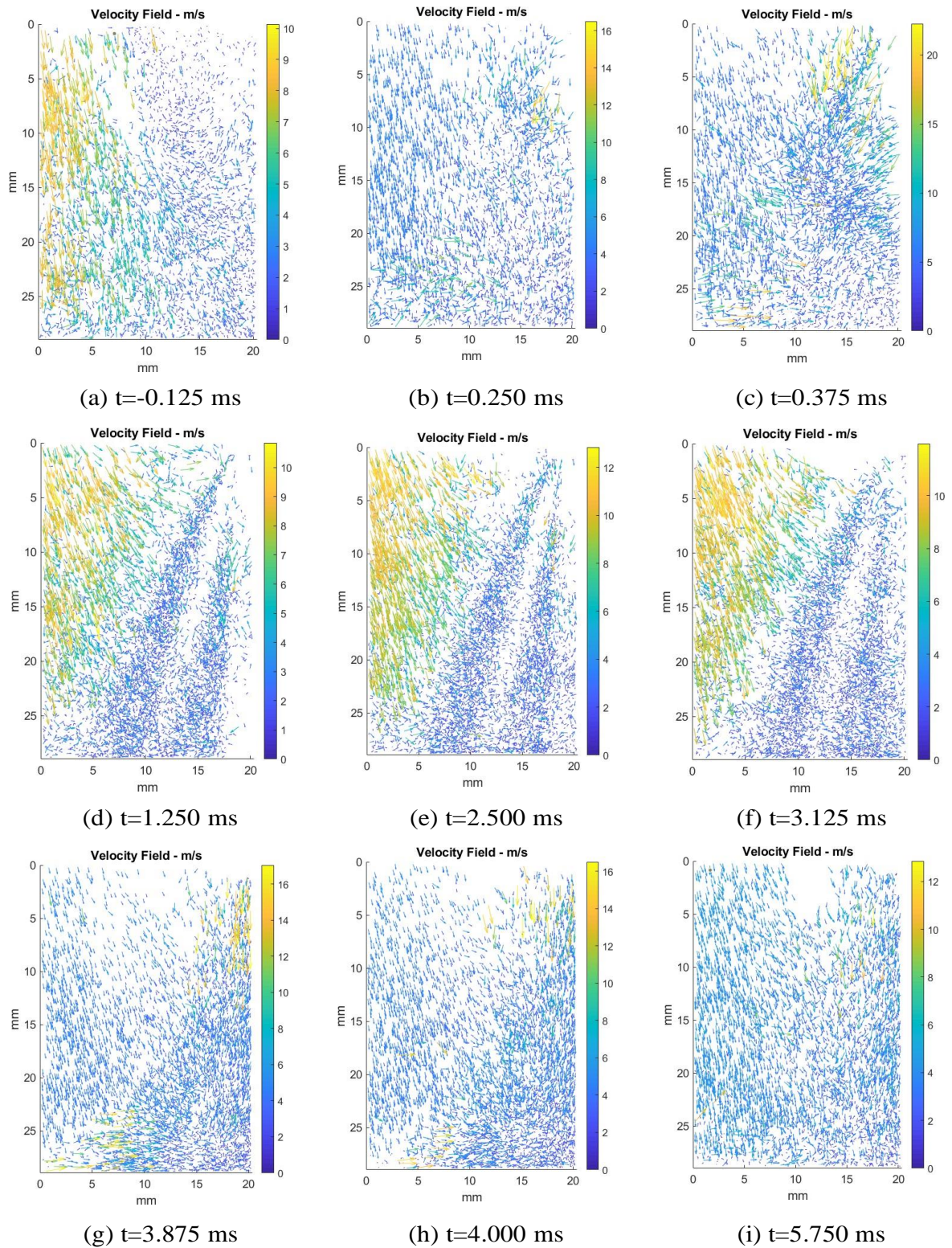
Figure 71: Comparison between global vector field velocities of the air during the spray injection for case PP4-02, in the IESC.

The PIV vector field presented by previous works showed highly order of direction of the velocity vectors. The PIV vector intensity field is shown in Figures 75 to 77. The PTV otherwise showed different orientations over the time of these vectors. This shows more coherency with the turbulence intensity shown in Figure 68b, where even with the stationary air flow, the perforated plates presented 15% to 30% turbulence intensity. With the presence of the spray, the amount of energy introduced in the FOV tends to elevate the intensity of the turbulence.

The PTV technique also presents the velocity intensity field of the flow, $|U|$. The interpolation of the vector field intensities can be seen in Figure 72. The velocities of the air tend to be around 5 to 18 m/s depending on their spatial location. The FOV selection made the analysis focus on the near spray tip, but some relevant structures could not be seen, especially in a quasi-steady state. Moreover, the recirculation structures discussed by (ZHANG et al., 2014) were dissipated by the vertical air flow injected in the chamber. The injector is a multihole type, and it is injected at velocities of 20 m/s or more, thus the injection of ethanol is not uniform through the section of the spray cone. The higher magnitudes were found in the quasi-steady condition and at the end of the injection. The quasi-steady condition shown in Figures 72d to 72f shows higher magnitudes near the spray tip due to the drag of the movement of the fast droplets. Moreover, when the injection stops, the spray drag causes a low-pressure region where the air tries to fill. The velocities of the air right below the spray tip are near 16 m/s.

Figures 71i and 72i show the influence of the spray injection after the spray closure. It could be observed that the spray drag elevated the air velocities and directed it down-stream. The velocities after the spray dissipate tend to zero near the spray region, and the recirculation zone reestablishes.

(a) t=-0.125 ms

(b) t=0.250 ms

(c) t=0.375 ms

(d) t=1.250 ms

(e) t=2.500 ms

(f) t=3.125 ms

(g) t=3.875 ms

(h) t=4.000 ms

(i) t=5.750 ms

Figure 72: Comparison between global vector intensity field of the air during the spray injection for case PP4-02, in the IESC.

(a) t=-0.125 ms (b) t=0.250 ms (c) t=0.375 ms

(d) t=1.250 ms (e) t=2.500 ms (f) t=3.125 ms

(g) t=3.875 ms (h) t=4.000 ms (i) t=5.750 ms

Figure 73: Comparison between horizontal vector intensity field of the air during the spray injection for case PP4-02, in the IESC.

(a) t=-0.125 ms

(b) t=0.250 ms

(c) t=0.375 ms

(d) t=1.250 ms

(e) t=2.500 ms

(f) t=3.125 ms

(g) t=3.875 ms

(h) t=4.000 ms

(i) t=5.750 ms

Figure 74: Comparison between vertical vector intensity field of the air during the spray injection for case PP4-02, in the IESC.

To visualize the characteristics of the velocity component, the velocity intensity, $|U|$, was divided into two components: u and v, horizontal and vertical components, respectively. The timestep evolution was represented by Figures 73 and 74. Due to color restrictions, the negative values (opposing the coordinates) represent the darker scales of blue. Note for Figure 73a the horizontal component of the recirculation zone near the 200 to 250 in vertical pixels (11, 32 to 14, 15 mm). It is the horizontal component that represents the recirculation zone. Moreover, the Figure 74a is the vertical component of the recirculation zone, the negative values are represented by the vertical vector opposing the coordinates showed in Figure 71a and dark blue color showed in Figure 74a, where $t = -0.125$ ms. The dark blue region represents the vertical components of the recirculation zone and its magnitude are found between -2 and 0 m/s. Also, the entrance of air, where the air is entering the chamber, is observed for the vertical velocity corresponding to the entrance values for the air mass flow. The inlet air is shown as yellow and light green, where its magnitude range is between 10 and 4 m/s. The vertical component loses strength as far as it enters the chamber.

At the beginning of the ethanol injection, 0.000 to 0.250 ms, the spray enters and elevate the vertical component, which can be seen in Figure 74b and 74c. Both magnitudes, horizontal and vertical components, accelerated towards the spray boundary, which represents the air moving due to the spray penetration. The vertical component represents most of the value of the velocity vector and dominates over the horizontal vectors. At this stage of injection, the early injection phase, the spray pushed the remaining cluster downstream. Additionally, a vertical upstream component at the center axis of the spray suggests that the air is filling a pressure difference caused by the spray injections at the shear layer droplet velocities and the center droplet velocities. The difference between those vertical components can be seen in the color comparison between Figures 74b and 74c, where the light blue and dark blue represents regions where the air is between -2 to 2 m/s and yellow represents velocities between 8 and 14 m/s.

(a) t=-0.267 ms

(b) t=0.000 ms

(c) t=0.133 ms

(d) t=0.800 ms

(e) t=1.200 ms
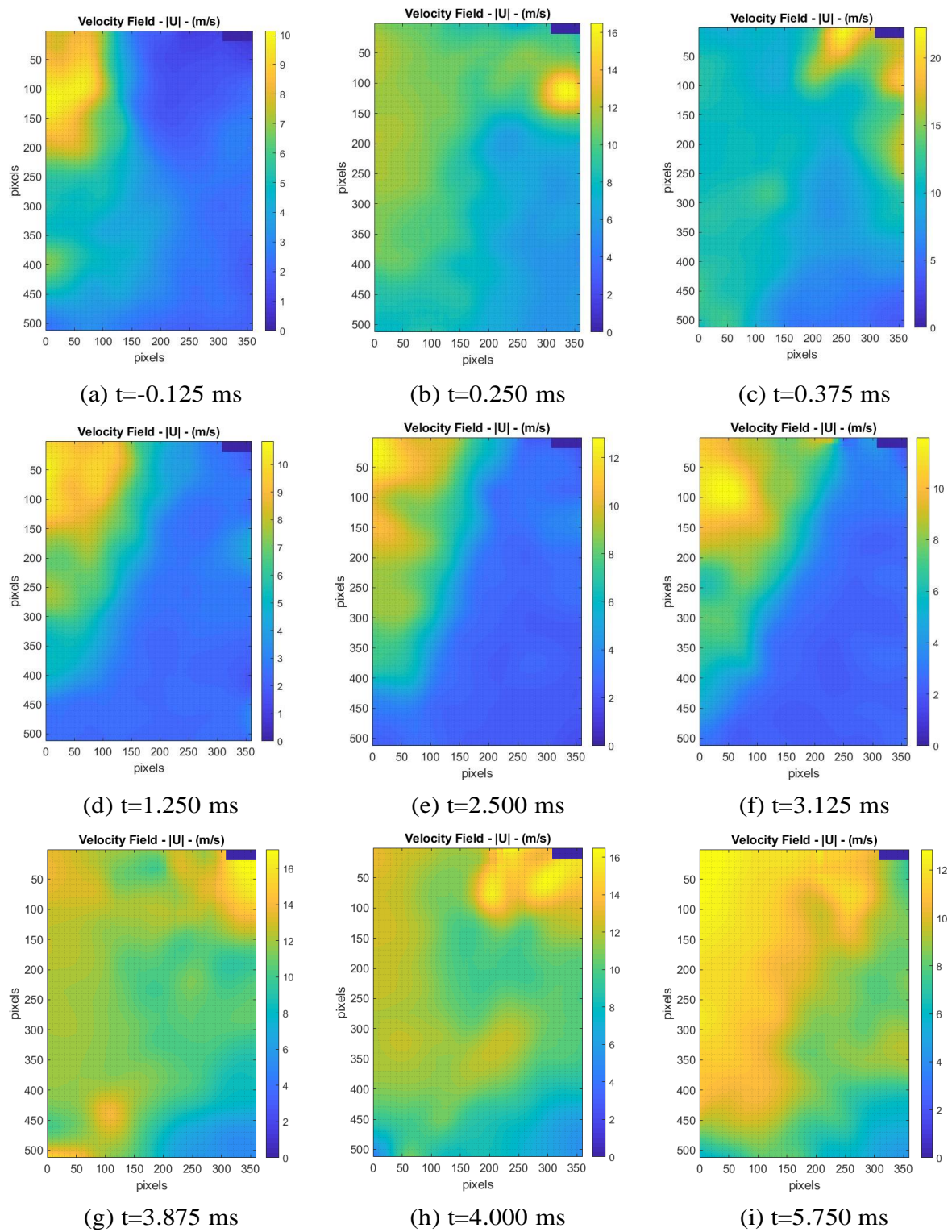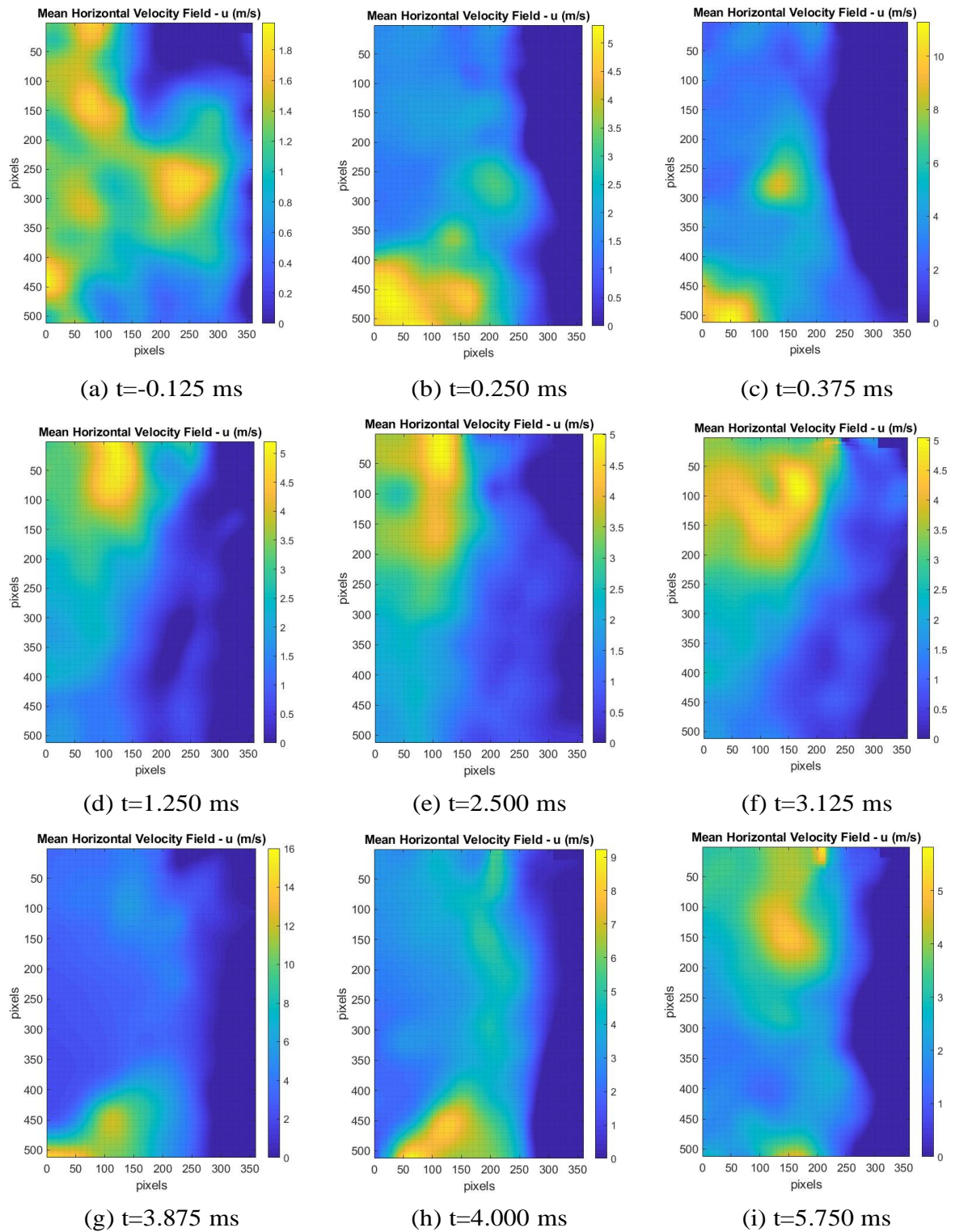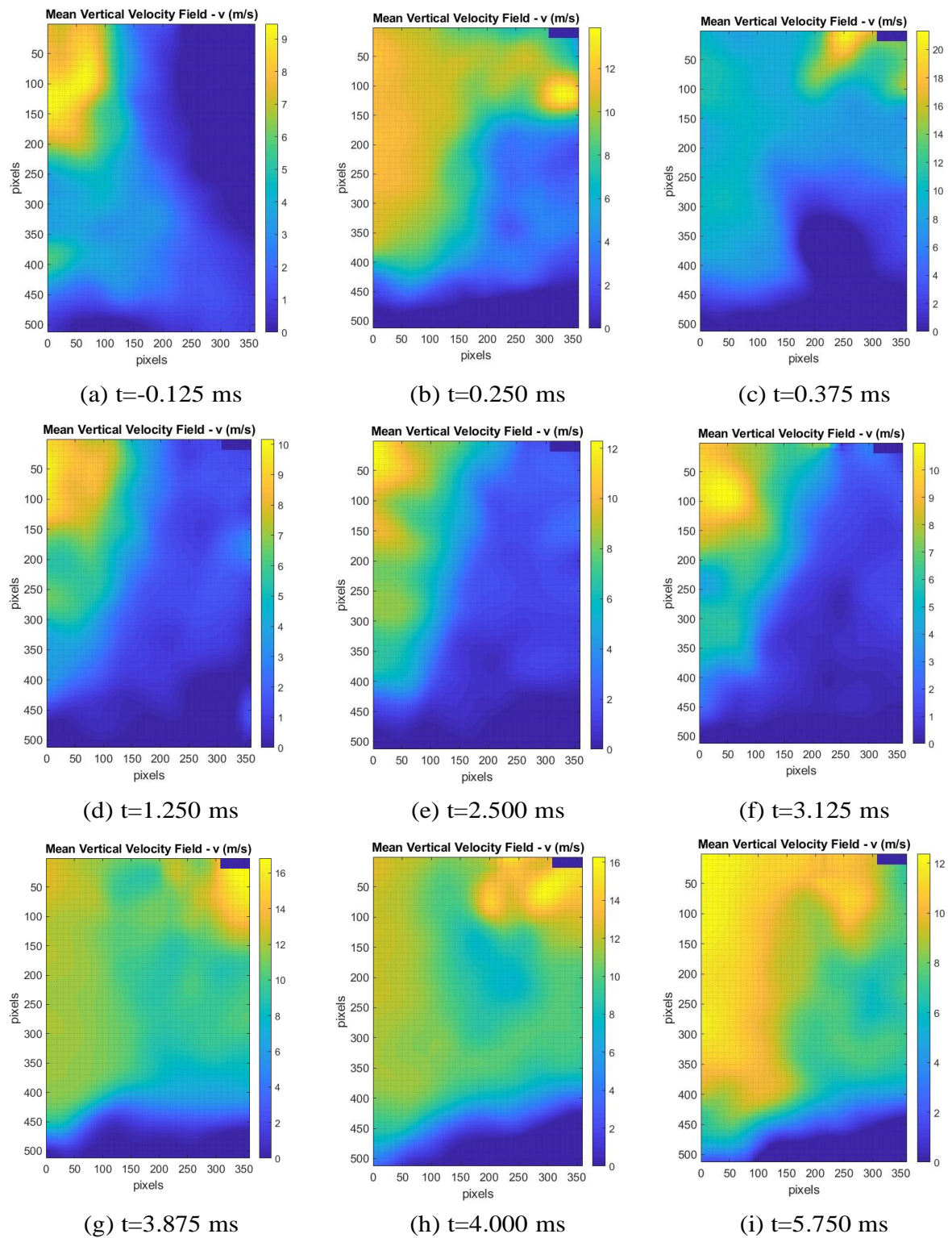
(f) t=2.667 ms

(g) t=3.733 ms

(h) t=4.000 ms

(i)

Figure 75: PIV measurement comparison between global vector intensity field of the air during the spray injection for case PP4-02, in the IESC. (TODARO et al., 2020).

(a) t=-0.267 ms

(b) t=0.000 ms

(c) t=0.133 ms

(d) t=0.800 ms

(e) t=1.200 ms

(f) t=2.667 ms

(g) t=3.733 ms

(h) t=4.000 ms

(i)

Figure 76: PIV measurement comparison between horizontal vector intensity field of the air during the spray injection for case PP4-02, in the IESC. (TODARO et al., 2020).
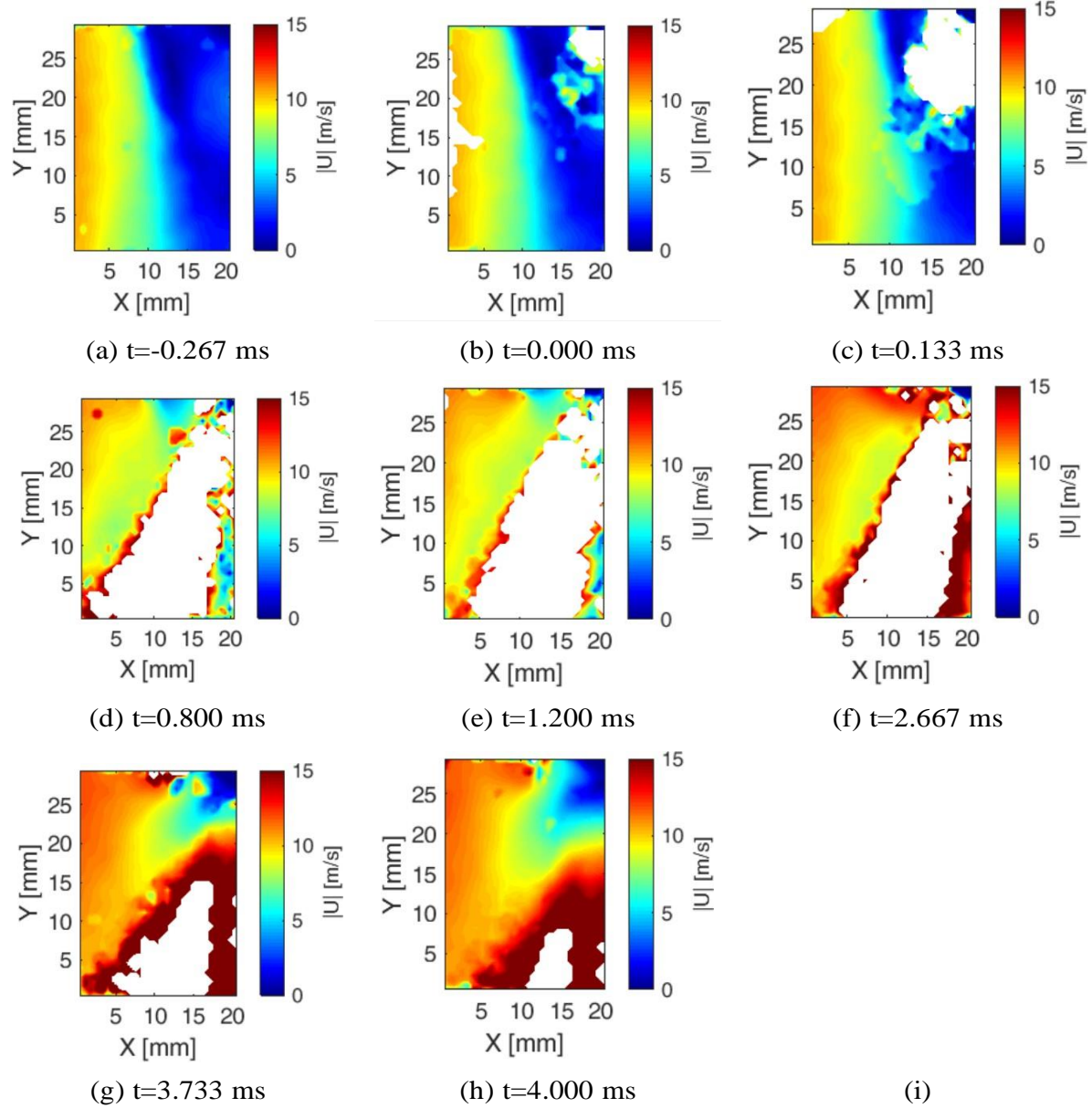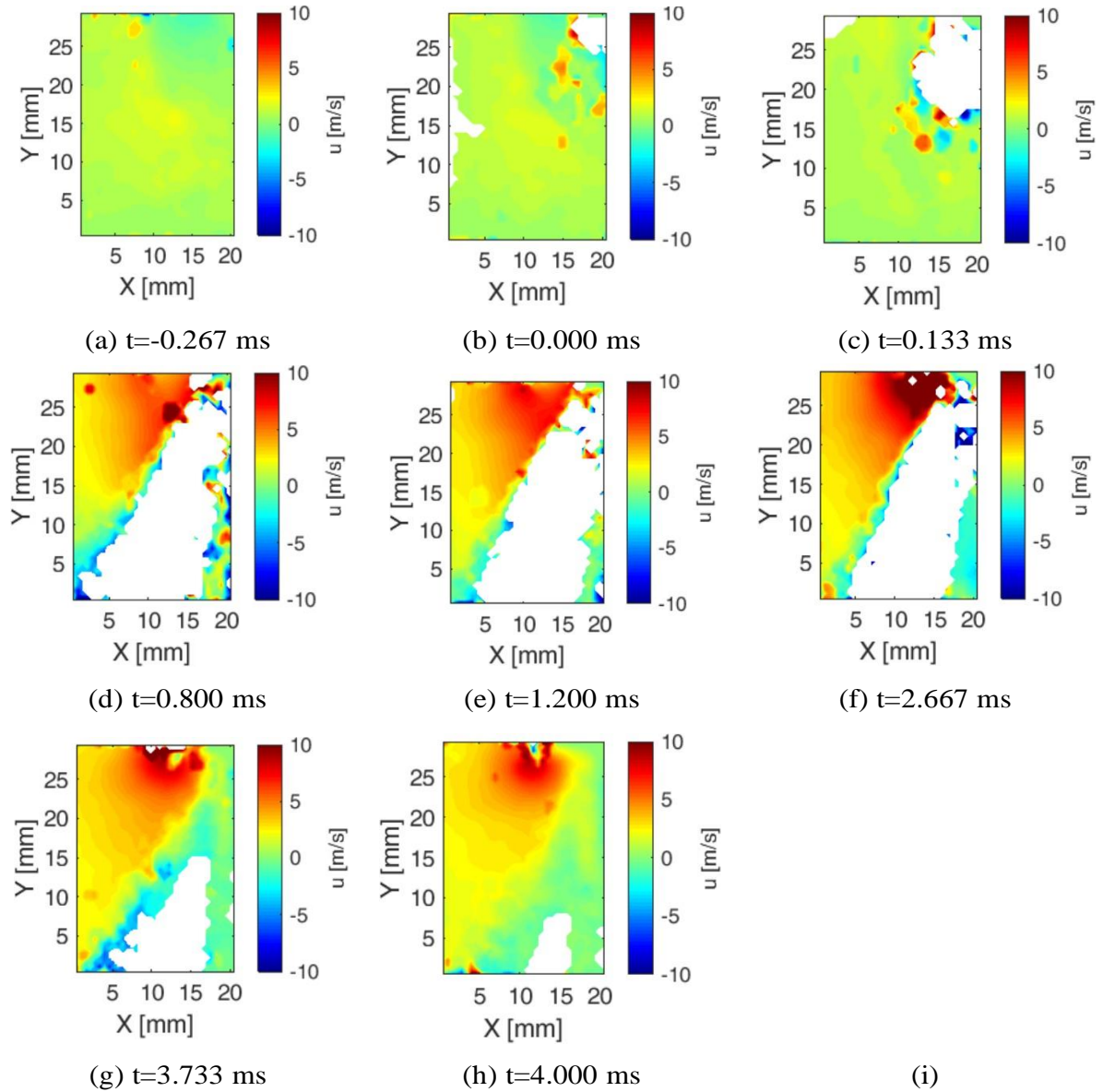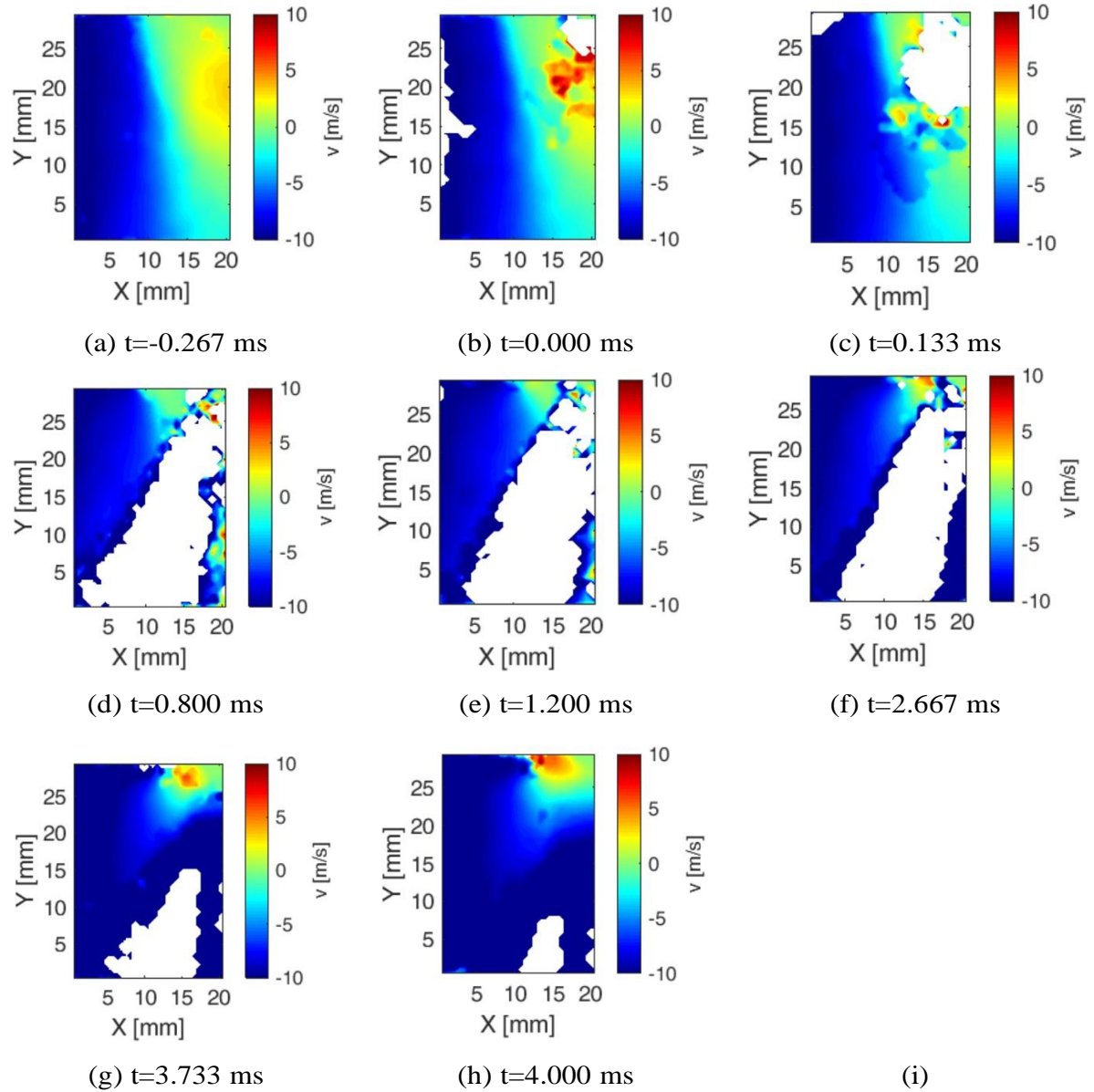
Figure 77: PIV measurement comparison between vertical vector intensity field of the air during the spray injection for case PP4-02, in the IESC. (TODARO et al., 2020).

The PIV results showed a horizontal component towards the spray tip in the quasi-steady condition, 1.250 to 3.125 ms, as shown in Figure 76d to 76f. Similarly, the PTV also showed an increase in horizontal velocities near the spray injection tip, as shown in Figures 73d to 73f. This structure corresponds directly to the spray injection pressure, where the magnitudes of the horizontal component tend to elevate while the pressure elevates.

At this stage of the injection, the velocity orientation is very similar to those found by PIV. Since the modification of the velocity fields is a result of the pressure differential acting over the region, the same velocity orientations were expected for PP4-02. However, the velocity magnitudes in PIV for 100 bar pressure injection showed higher magnitudes, especially for the region near the initial dense spray.

The end of the injection is shown by the Figures 73g to 73h, for u, and 74g to 74h, for v. The spray drag elevates u in the interface of the two regions, where at the center of the injector the magnitudes were near zero or negative. On the other hand, the vertical components near the spray tip measured a strong component of the air moving toward the spray. Since this effect is related to the mass and momentum conservation after the needle valve closing, a higher velocity magnitude should be expected for case with higher injection pressure. This indicated that the injector structure promoted remaining air drag behind the spray, and it was caused by the geometry configuration of the experiment and the inlet air velocities.

To go further into the analysis, a velocity profile over some specific locations were selected. Figure 78 shows the horizontal profile over five vertical location. The shear layer location was represented with a cross, and measurements on the right side of the cross represents the air velocities inside the spray injection.
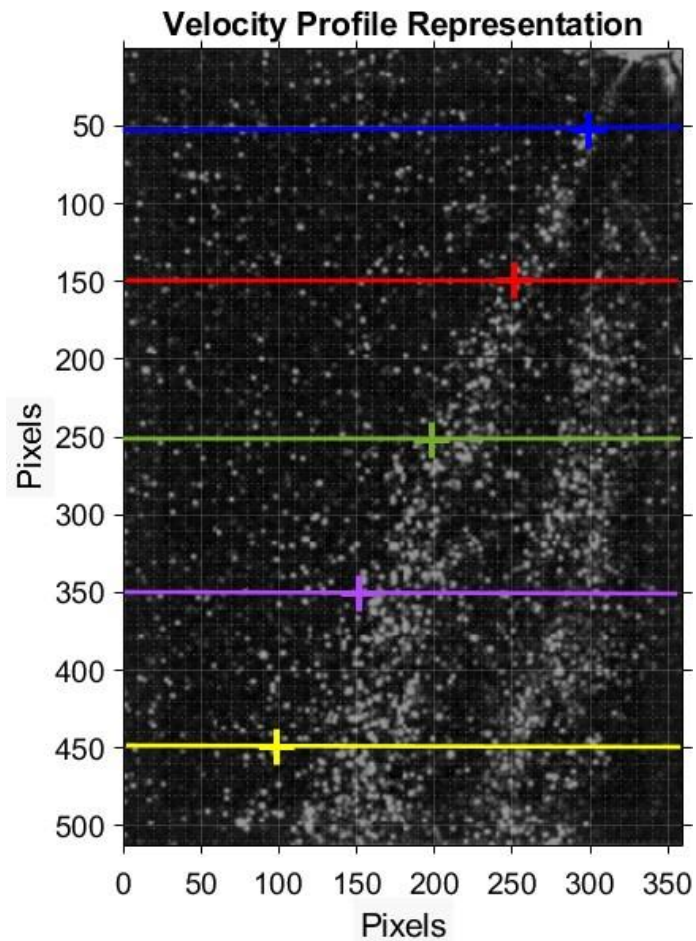
Figure 78: Shear layer of the spray and the selected velocity profiles for velocity components, *u* and *v*, horizontal and vertical, respectively.

Figures 79 to 87 represent the velocity profile over the lines represented by Figure 78. The first graph, Figure 79, shows the -0.125 ms SOI. Since at this time there is no spray, it is not represented the shear layer in the graph. The *u* velocities had -0.2 to 1.8 m/s range. The negative values near $y = 50$ (2.83 mm) and $x > 200$ represent the low velocities with opposite directions of the recirculation zone. The *v* velocities were separated into two regions described previously. After $x > 150$ pixel the vertical velocities tended to zero or even negative values for $y = 50$ (2.83 mm) and $y = 150$ (8.49 mm), where the velocities were upstream and opposite to the vertical axis. The inlet air velocities induced downstream velocities until $y = 250$ (14.15 mm) and $x > 275$ pixels. The inlet air flow changes the vertical component, where *v* velocities were 8 to 10 m/s, to 2 to 4 m/s. The *u* velocity grows due to vortical characteristic of the flow at this region.

(a) Horizontal component   (b) Vertical component

Figure 79: Comparison between velocity profile components for time instant t = - 0.125 ms SOI in the IESC with Beta pre-processing.

The velocity intensity graphs for $t = 0.125$ ms, Figure 80, show elevations for u and v magnitudes. At this time, the spray begins to be developed, and the droplet momentum affects the u velocity near the spray tip. The u direction changes between 250 to 300 pixels in x direction and between 50 to 150 in y direction. This region represents the edge of the spray cone. Also, the v magnitudes changes for $y = 50$ (2.83 mm) to $y = 150$ (8.49 mm). At $x > 150$ pixels, the velocity grows from 2 to almost 10 m/s. However, for $y > 250$ no apparent change was observed in v velocities.

(a) Horizontal component (b) Vertical component

Figure 80: Comparison between velocity profile components for time instant t = -0.125 ms SOI in the IESC with Beta pre-processing.

For $t = 0.250$ ms, Figure 81, the spray development was almost completed. At this stage of the injection, the u velocities changed the transition point from negative values to positive at 200 to 250 in x axis and between $y = 150$ (8.49 mm) to 250 (14.15 mm) in y axis. Comparatively with $t = 0.125$ ms, the transition point changed its location, which means that the tip of the spray cone extended its length in y and to the opposite direction of the center axis of the spray in x. Additionally, the u magnitude at $y = 450$ (25.47 mm) elevates from 4.5 average to 7 m/s. This raise could be the effect of the injection moving the air around the spray cone as a consequence of the air mass continuity-equilibrium penetration zone. Moreover, the v component at $y = 50$ (2.83 mm) elevated the magnitude to 16 m/s at the shear layer region. It was an increase of 52.4%. The v component for other y did not have a relevant increase.

(a) Horizontal component   (b) Vertical component
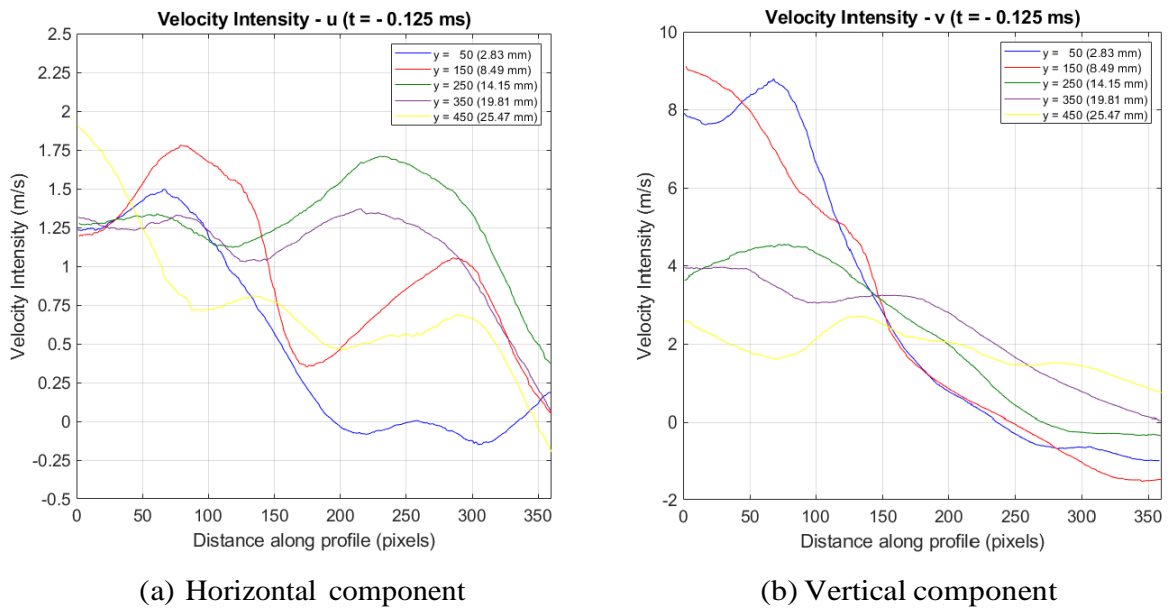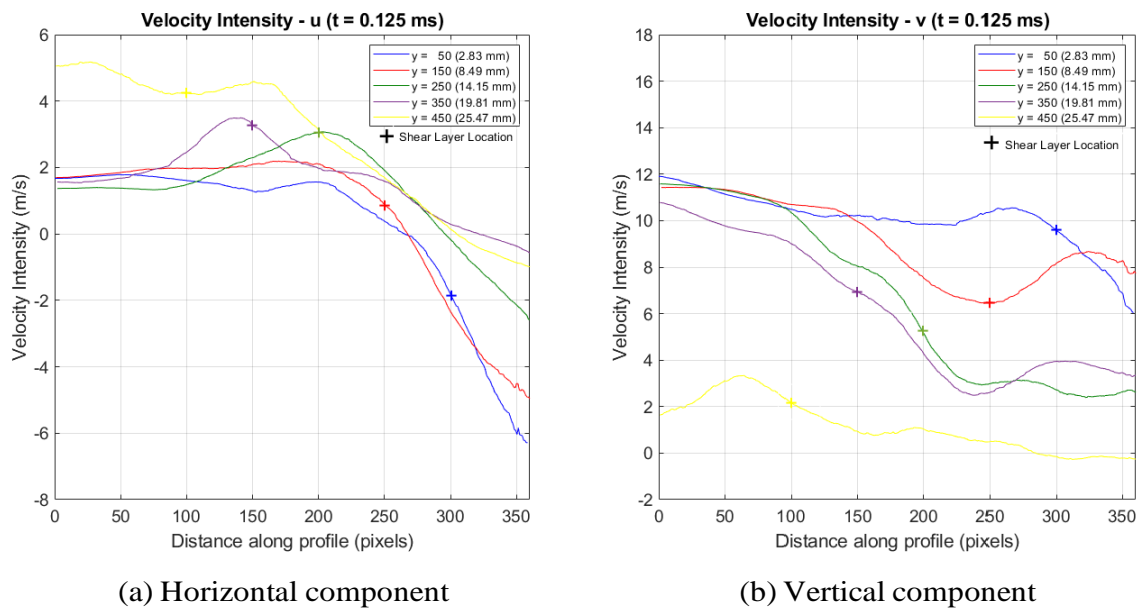
Figure 81: Comparison between velocity profile components for time instant t = 0.250 ms SOI in the IESC with Beta pre-processing.

At the quasi-steady condition, figures 82 to 84, the velocities graphs show small changes between each other even with 2 ms in time difference. The *u* velocity of the air constantly decreases with the evolution of *y*. The peak of 5 m/s reaches between 100 to 150 at *y* = 50 (2.83 mm). The *u* component increasing could be seen as a process of drag of air inside the internal spray cavities. These cavities extend in all spray development, but are more pronounced near the spray tip. These cavities turn the velocity vectors from the vertical to the horizontal direction. The *v* component enters the chamber with 12 m/s velocity, and it decreases with *y* growth until 2 m/s. At the shear layer, *u* and *v* had low-velocity intensity because the amount of light scattered by the droplets could reduce the PTV capacity to recognize the particle tracking. The turbulent intensities found by (BERTI, 2018) also demonstrated very similar results for quasi steady condition.

(a) Horizontal component   (b) Vertical component

Figure 82: Comparison between velocity profile components for time instant t = 1.250 ms SOI in the IESC with Beta pre-processing.

(a) Horizontal component   (b) Vertical component

Figure 83: Comparison between velocity profile components for time instant t = 2.500 ms SOI in the IESC with Beta pre-processing.
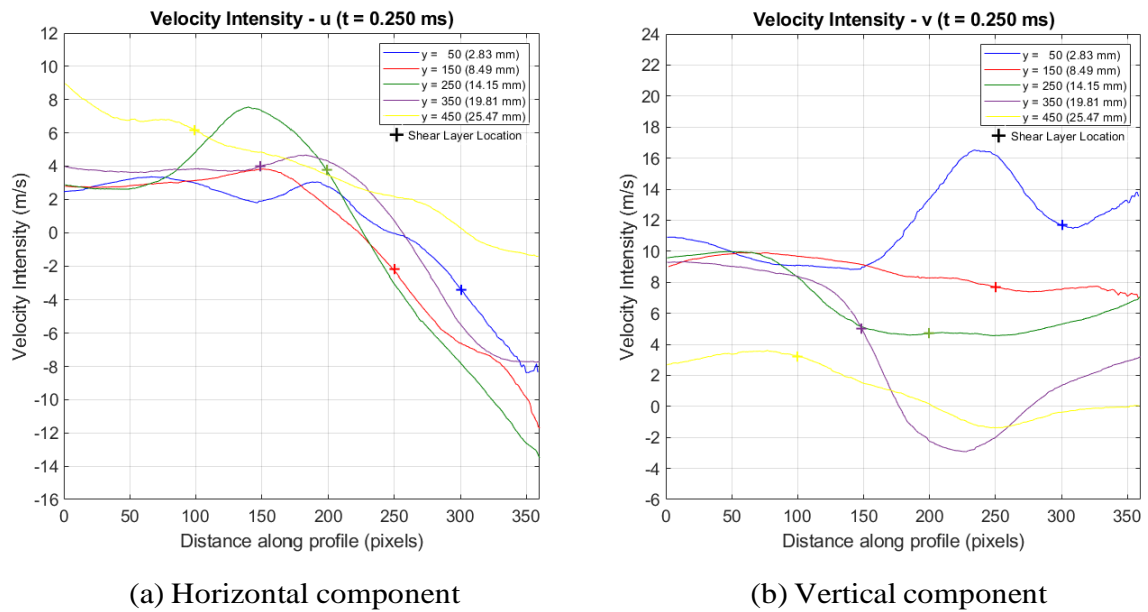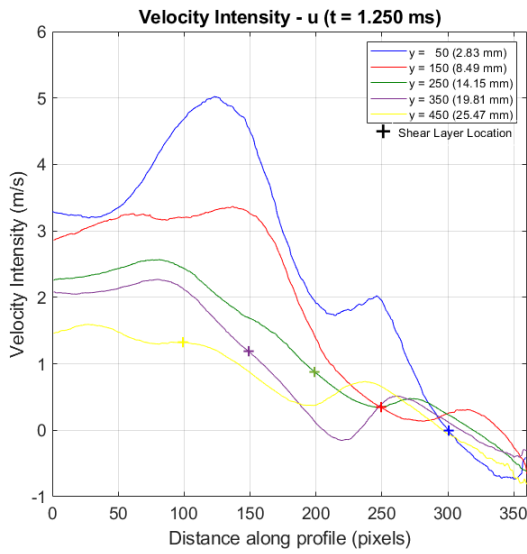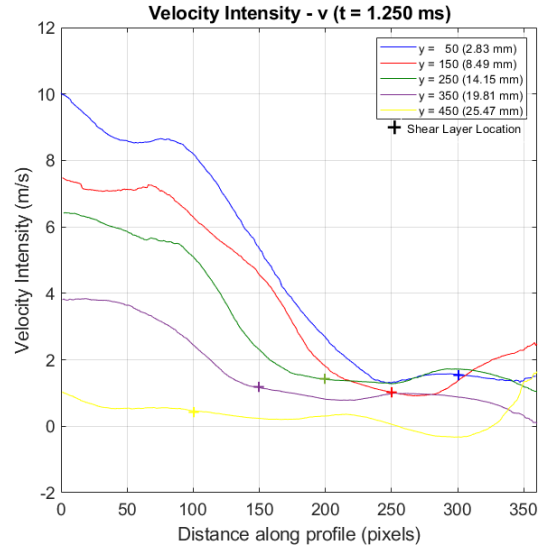
(a) Horizontal component   (b) Vertical component
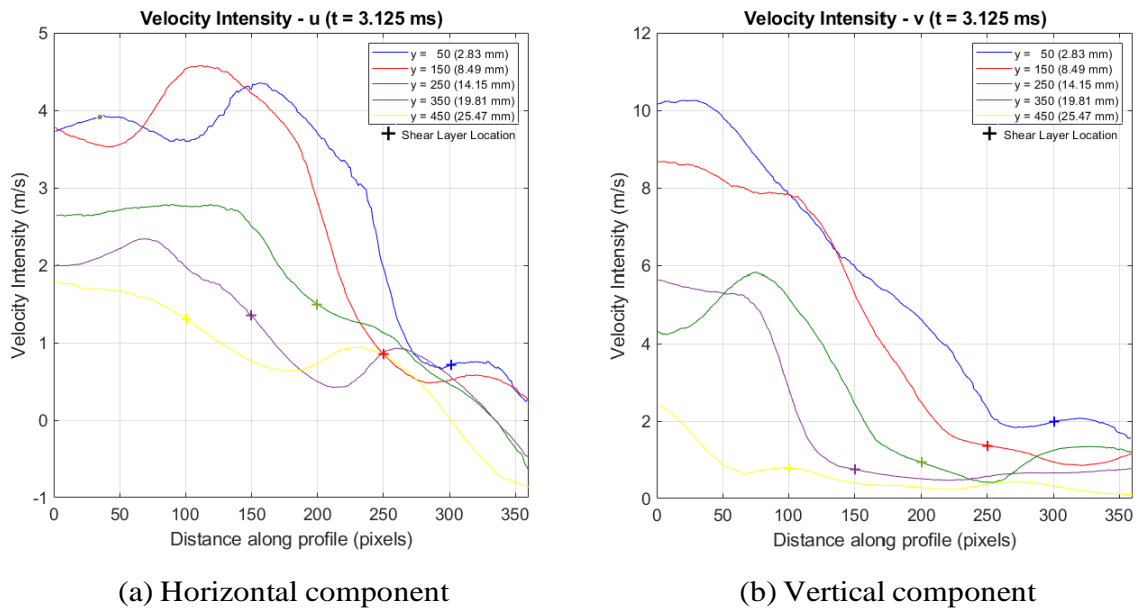
Figure 84: Comparison between velocity profile components for time instant t = 3.125 ms SOI in the IESC with Beta pre-processing.

At the end of injection, Figures 85 to 86, *u* component had the same magnitude profile for both time instants, except for *y* = 450 (25.47 mm), where a strong positive component could be seen. This effect might be the air movement outside the spray moving through the spray drag between spray cavities. Due to limitations on interrogation area, the complete flow below *y* = 450 (25, 47 mm) could not be seen. However, the air in 50 pixel in *x* showed velocities in order of *u* = 5 m/s and *v* = 7 m/s. An exchange on the almost pure vertical component at *x* = 0 pixels, where *v* = 8.5 m/s, turns the velocity vectors to near completely horizontal at *x* = 100 pixels, where *u* is between 6.5 to 11.5 m/s. The *v* component shows an increase of vertical vector intensity in the center of the spray, where *y* = 50 (2.83 mm). The velocity raise to near 16 m/s.

(a) Horizontal component
(b) Vertical component
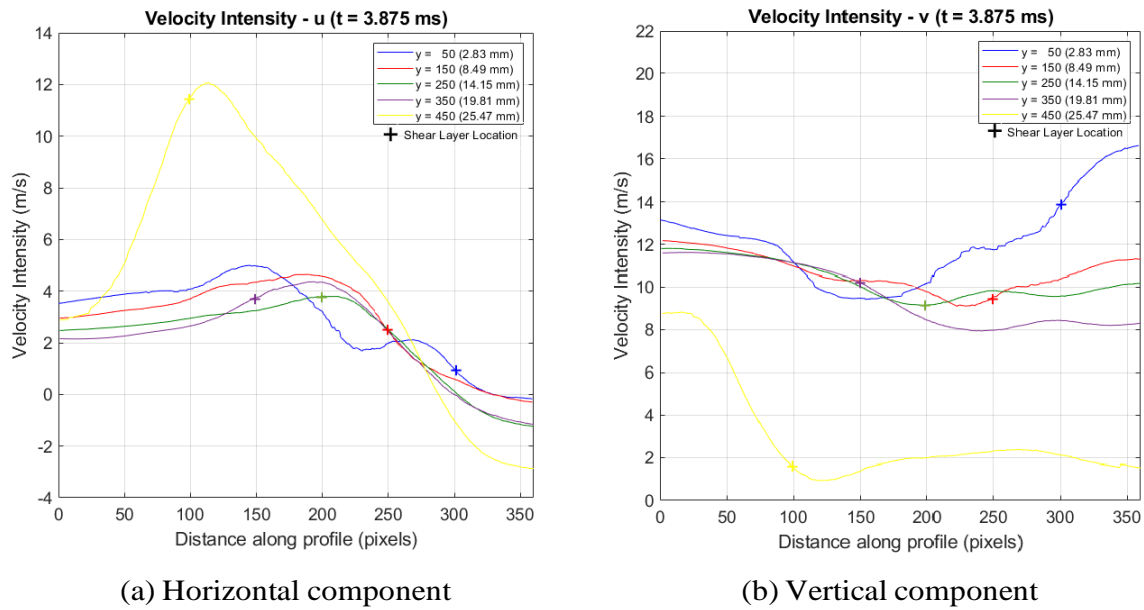
Figure 85: Comparison between velocity profile components for time instant t = 3.875 ms SOI in the IESC with Beta pre-processing.
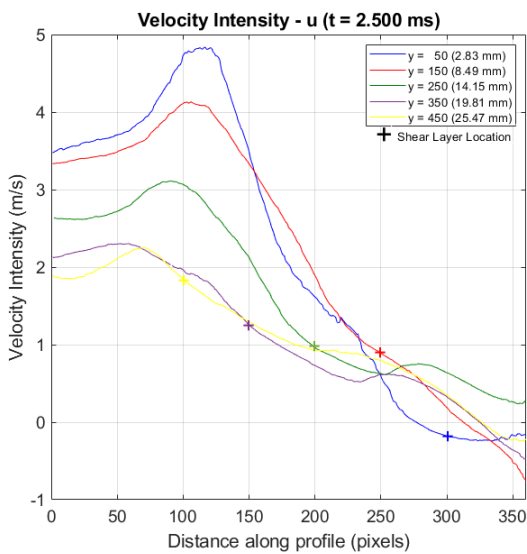

(a) Horizontal component
(b) Vertical component
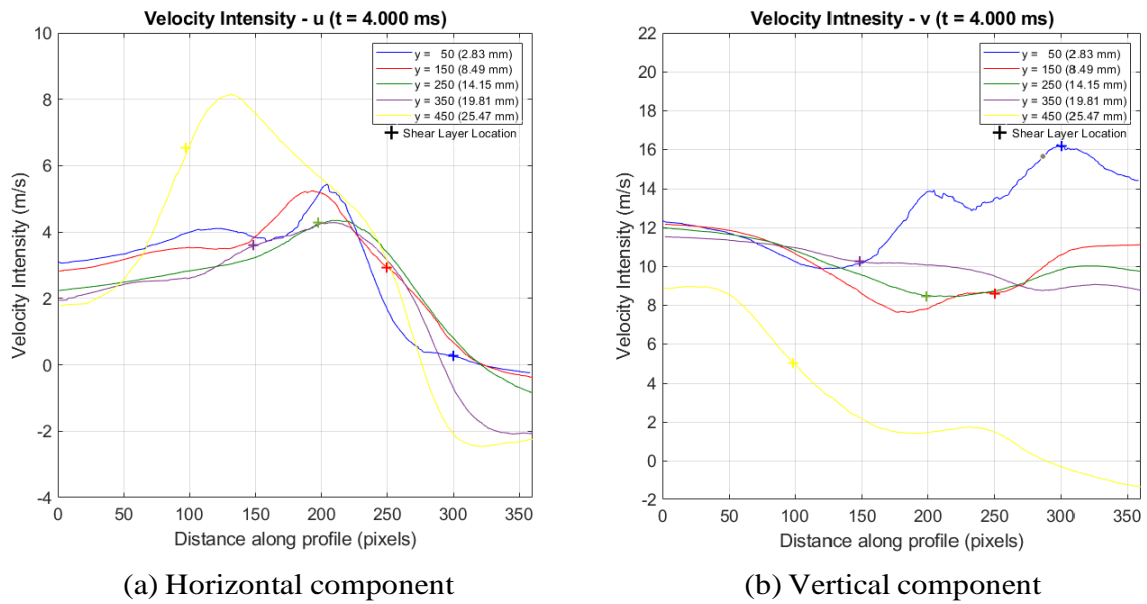
Figure 86: Comparison between velocity profile components for time instant t = 4.000 ms SOI in the IESC with Beta pre-processing.

The turbulent effects of a spray injection last more time than the injection closure or the spray passage. At $t = 5.750$ ms the air behavior inside the chamber tends to return to $t = -0,125$ ms. However, the velocity comparison did not show similarities. The v velocities had no negative values and no recirculation structure could be seen.
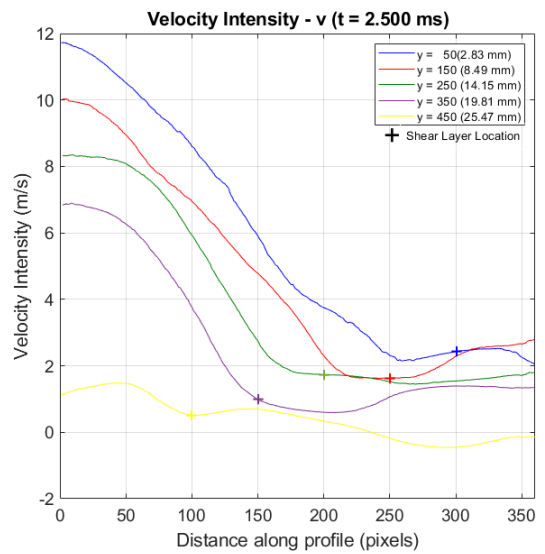
(a) Horizontal component   (b) Vertical component
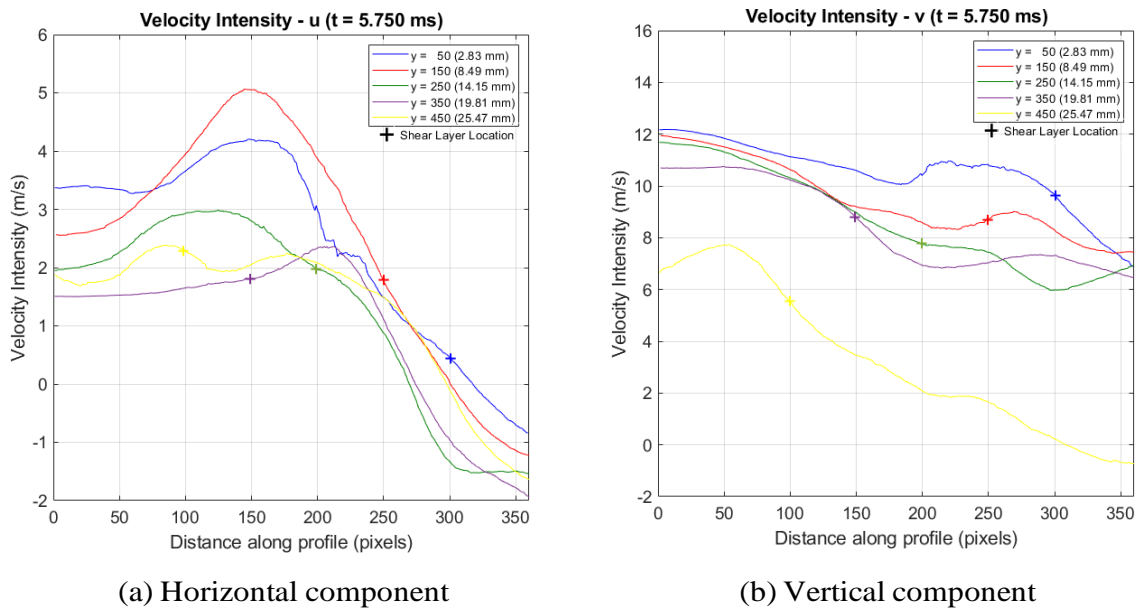
Figure 87: Comparison between velocity profile components for time instant t = 5.750 ms SOI in the IESC with Beta pre-processing.

5.2 Peak locking analysis

The spray development and its interactions with the continuous surrounding air are time-dependent to statistical random processes. Therefore, all the results were ensemble-averaged by the temporal evolution of the spray, as described by section 4.3.3. The time window selected was 100 ms between spray injection, shown in Figure 88. In each case, 255 injection events were captured and were chosen to improve the convergence of the statistical properties (BERTI, 2018). The experiments were divided into runs of 17 injection events. According to (BERTI, 2018), this value is high as the common procedure to improve statistical properties.
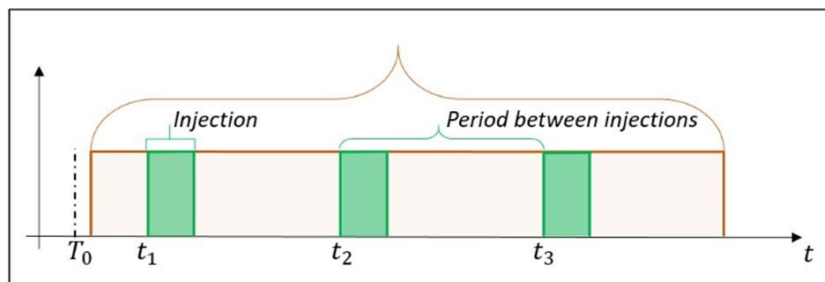
Figure 88: Spray injection period over the time representing the sequence of 17 injections over 100 ms. Adapted from (BERTI, 2018).

The uncertainties associated with the measurements can be classified into two categories: random error and bias error. The random error can be reduced by statistical analysis using a sufficiently large ensemble set. The bias error, however, may be present in the results even after averaging (CHEN; KATZ, 2005). The most significant bias error is the peak locking error, where this phenomenon is inherent to the smooth curve-fitting which is used to obtain the sub-pixel part of the displacement. To avoid significant bias errors due to peak locking, it is important to have a particle image diameter of at least two pixels. The pixel diameter selected for the PTV analysis was 3 as shown in Table 9. The peak locking is caused by very small particle images, where to occur a shift of the estimated displacement values towards the closer integer pixel position (SCHARNOWSKI et al., 2019).
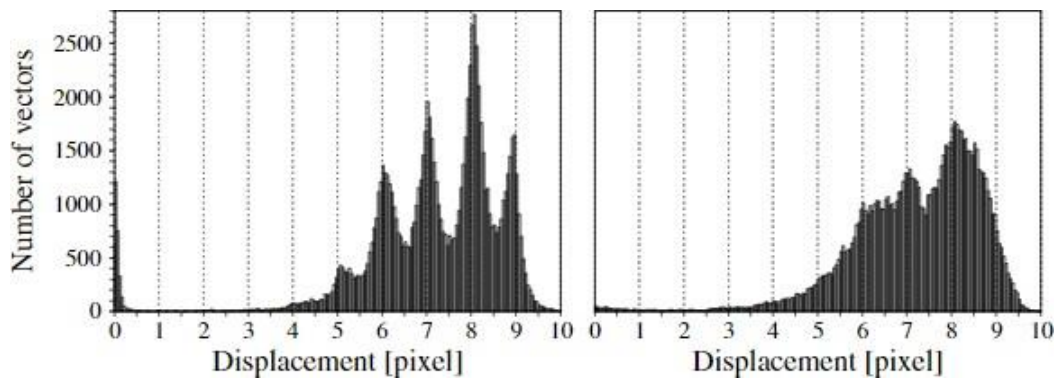
(a) Histograms of displacement data obtained from a 10-image sequence of a turbulent boundary layer illustrating the peak locking associated with insufficient particle image size (left). Histogram bin-width = 0.05 pixel. (RAFFEL et al., 2007).
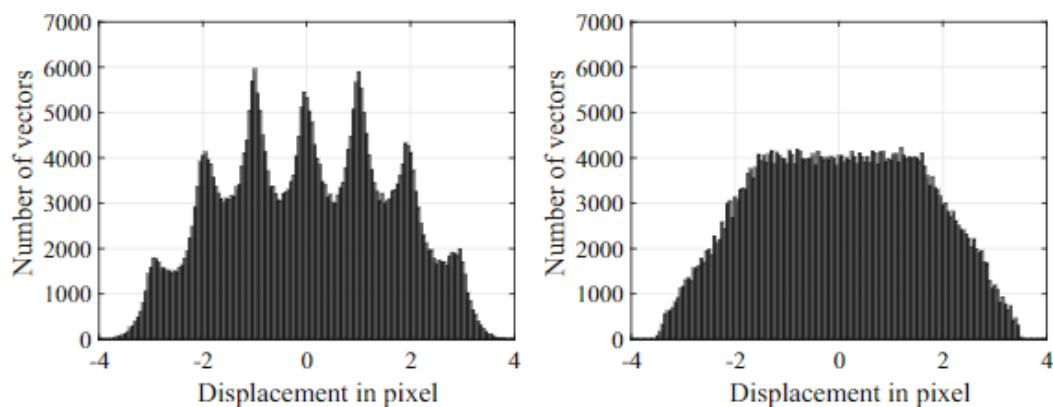
(b) Histograms of estimated displacement for a particle image diameter of 1 pixel illustrating the peak locking associated with insufficient particle image size (left) and 3 pixel image size (right). Histogram bin-width = 0.05 pixel. (RAFFEL et al., 2018).

Figure 89: Histogram distortion shown by insufficient size particles. (RAFFEL et al., 2007) (RAFFEL et al., 2018).
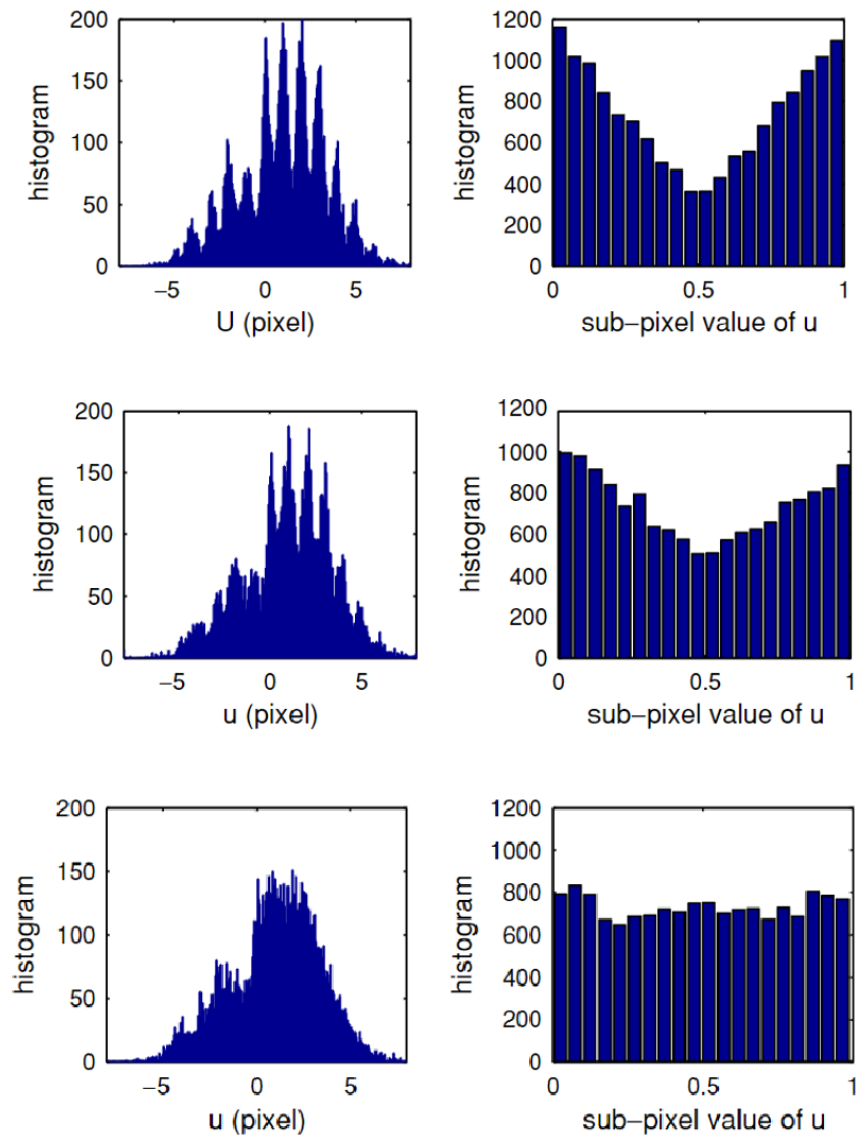
Figure 90: Histograms of the measured displacement component (left) and its sub-pixel part (right) done for three different approach to improve sub-pixel accuracy and reduce peak locking effect. The bin-width was 0.05 pixels. a)Parabolic SPCF. b) Gaussian SPCF and c) CMM-PID. Adapted from (CHEN; KATZ, 2005).

The presence of peak locking can be detected by plotting a displacement histogram. The histogram would make a distortion, and it is a good indicator that the systematic errors are larger than the random noises in the displacement estimates. The histogram distortion can be seen in Figures 89a and 89b. However, if the random error noise is larger than the systematic error a smooth histogram can also be present, so care must be taken with misinterpreting the histogram data. Also, for the peak locking, the probability density function shows its pinnacle at the integer pixel values. Only if the peak locking is negligible that velocity histograms appear similar as only the random error

varies (SCHARNOWSKI et al., 2019). The sub-pixel displacement varies between 0 and 1, and for peak locking occurrence the histogram would show higher values close to 0 and 1, as shown in Figure 90.

For the PTV measurements, the peak locking analysis was made for each velocity field. To prove the low presence of the peak locking error, the histograms showed near flat distribution in the sub-pixel displacement, and no distortion in the displacement histograms. The results are shown in Figures 91 to 95.
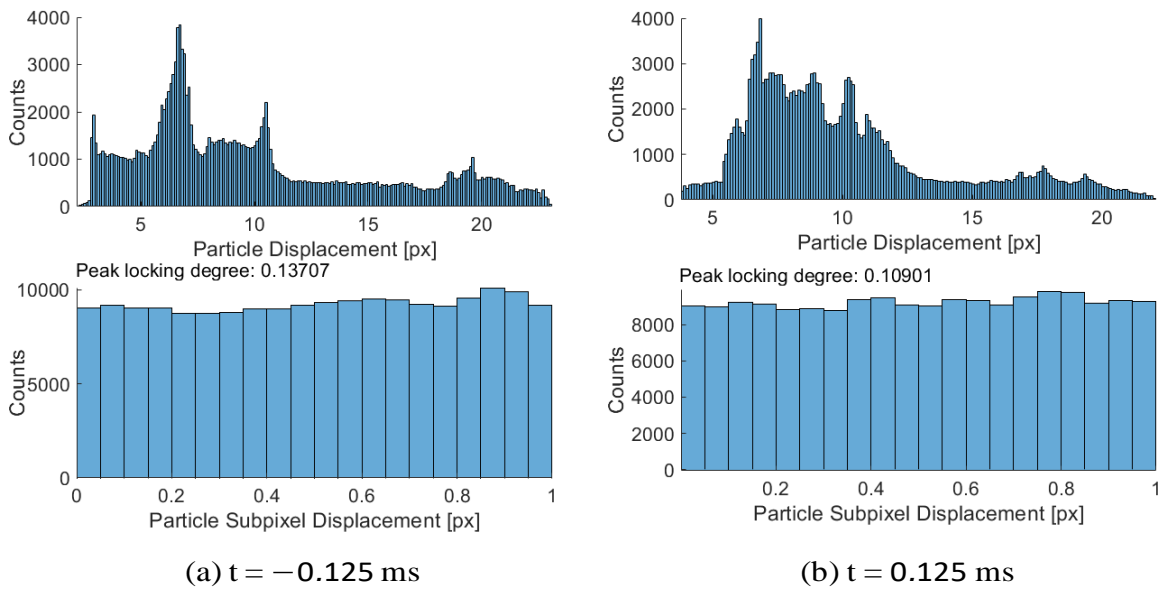
(a) $t = -0.125$ ms   (b) $t = 0.125$ ms

Figure 91: Histograms of the displacement in pixel and sub-pixel streamwise displacement for a)$t = -0.125$ ms b) $t = 0.125$ ms. Bin-width is 0.05 pixels.
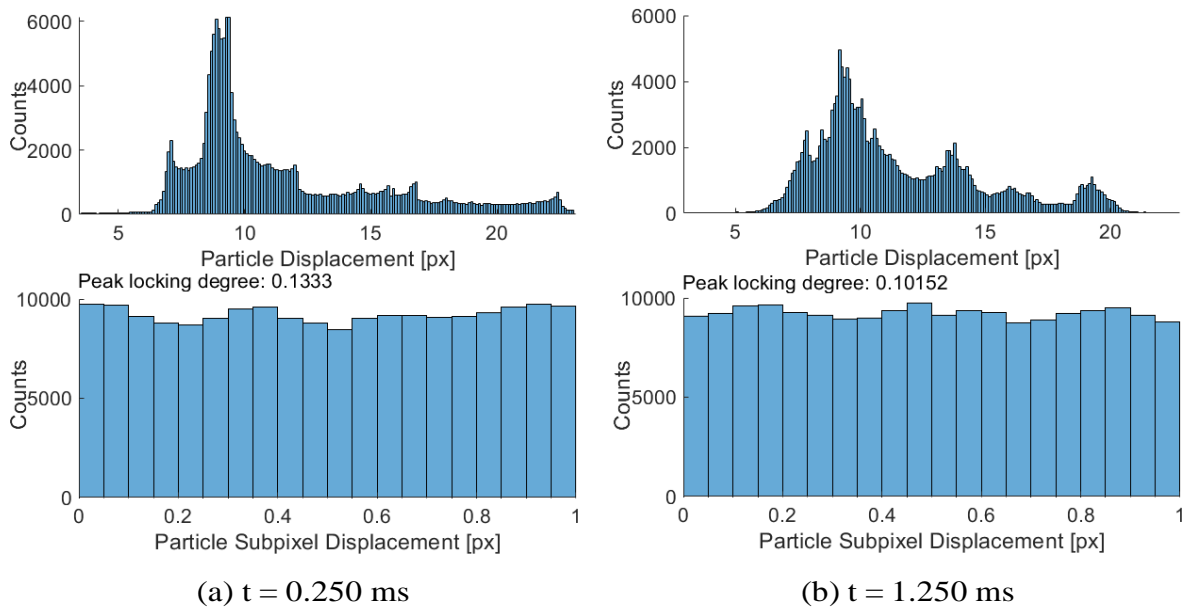
(a) t = 0.250 ms
(b) t = 1.250 ms

Figure 92: Histograms of the displacement in pixel and sub-pixel streamwise displacement for a)t = −0.250 ms b) t = 1.250 ms. Bin-width is 0.05 pixels.
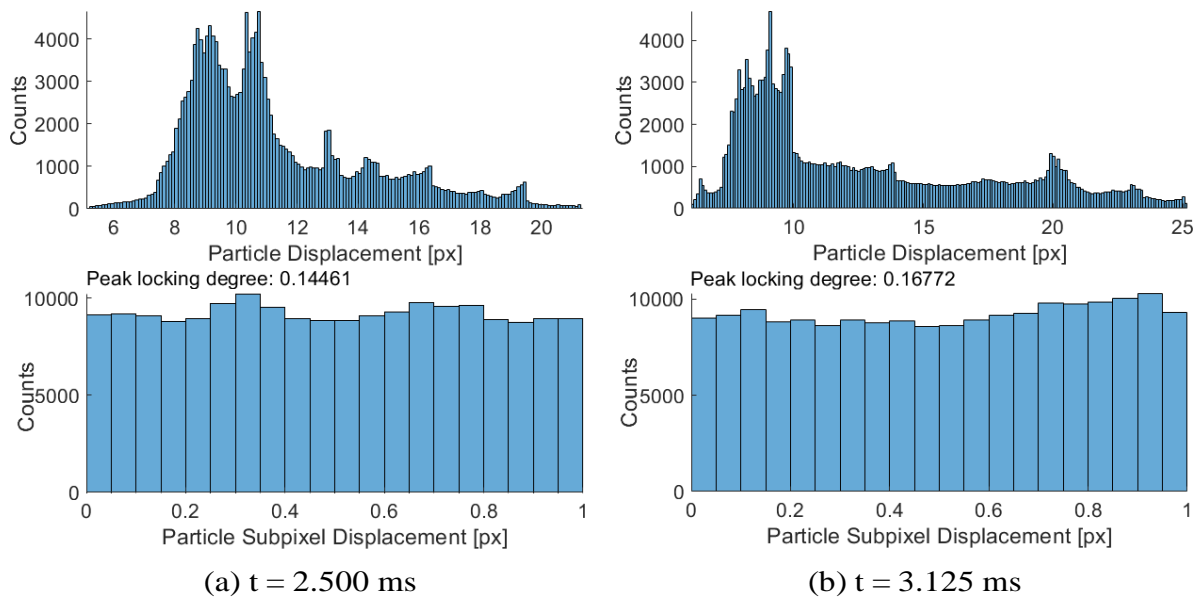
(a) t = 2.500 ms
(b) t = 3.125 ms

Figure 93: Histograms of the displacement in pixel and sub-pixel streamwise displacement for a)t = 2.500 ms b) t = 3.125 ms. Bin-width is 0.05 pixels.
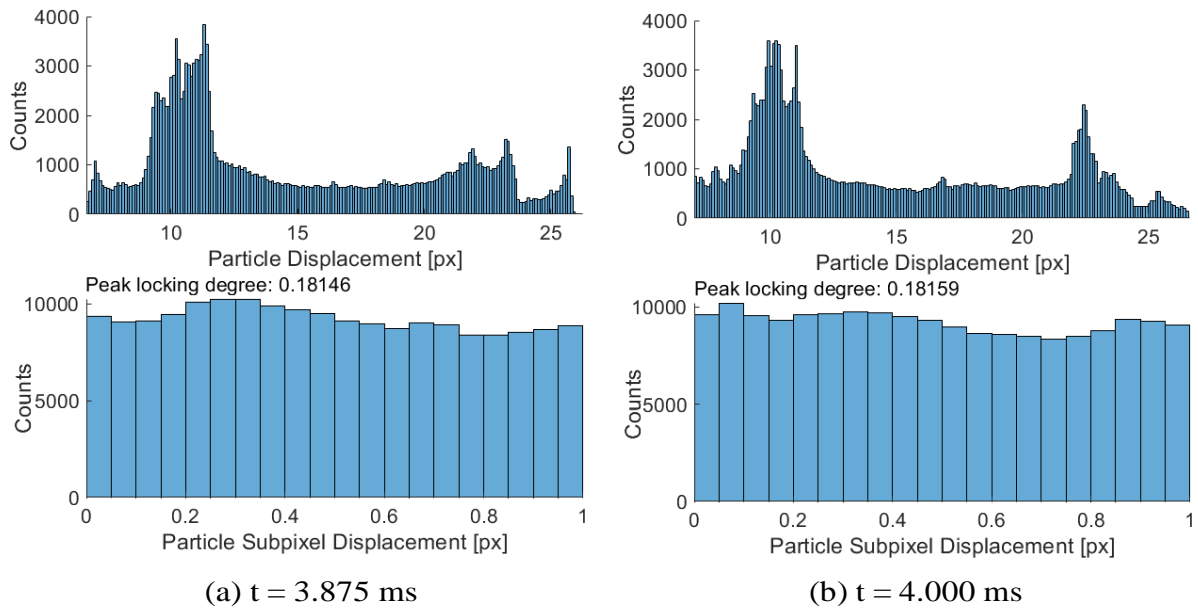
(a) t = 3.875 ms   (b) t = 4.000 ms

Figure 94: Histograms of the displacement in pixel and sub-pixel streamwise displacement for a)t = 3.875 ms b) t = 4.000 ms. Bin-width is 0.05 pixels.
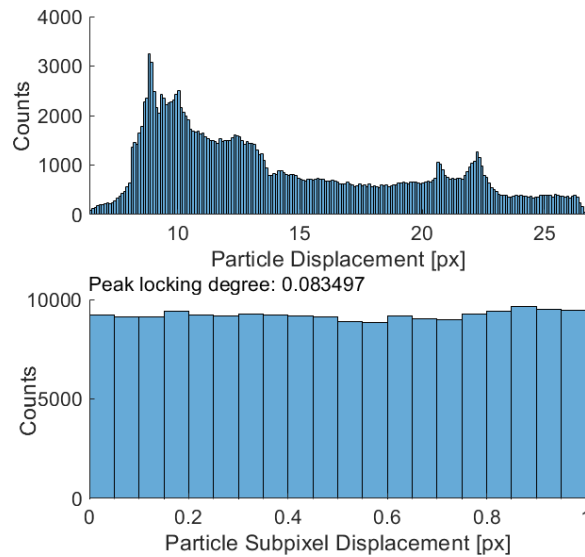
Figure 95: Histograms of the displacement in pixel and sub-pixel streamwise displacement for t = 5.750 ms. Bin-width is 0.05 pixels.

The peak locking degree is a parameter that shows the level of the peak locking presence. The degree is calculated by finding the minimum and maximum counts and calculating them with

$$PD = 1 - \frac{N_{min}}{N_{max}} \tag{5.1}$$

Where PD is the peak locking degree, N_{min} is the minimum occurrence of a sub-pixel displacement in pixel and N_{max} is the maximum occurrence of a sub-pixel displacement in pixel. For the PTV measurements of the present work, the values of PD vary between 0.083497 and 0.18159. The higher the values of the peak locking degree, the more presence of the bias error or peak locking error.

6 CONCLUSIONS AND FUTURE WORKS

The objective of the present work was to apply the particle tracking technique to the previous air flow image acquisition found by PIV technique. The PIV technique showed higher noise ratio associated with lower particle densities and high velocity gradients. The newer PTV algorithms aims to handle with higher seeded flows and the particle density found with previous works suits with PTV application. A study of the surrounding air was proposed and a comparison with PIV was provided.

The present work contributes to the field of spray development by studying the surrounding air flow using PTV technique analysis. A discussion on the technique, the characteristics of the air flow around spray the development and PTV limitations were done. The PTV analysis was proposed to tackle the noise presence associated with low particle concentrations found by PIV measurements from previous work. The major conclusions and remarks were summarized in this section.

The experimental procedure selected a constant-flow chamber to evaluate the effects of a continuous flow outside the spray. The PTV technique contributed to provide data in these experimental conditions, which are real engine general conditions, except for low rotational speed and high load conditions. The two-phase analysis showed to be a challenge to the technique due to elevated divergence on particle concentrations. The spray light scattering could not provide particle identification near the shear layer.

A pre-processing technique was selected to enhance the particle identification. The Beta pre-processing was elaborated with spatial filtering and showed 150% better relation in SNR according to (TODARO et al., 2020). The pre-processing technique was selected to improve the particle identification, and the average outliers detection was about 15% of the found vectors.

The amount of acquired results was an average-ensemble of 17 injections for each velocity field. This consideration for the PTV application was taken to provide reliable results in statistical approach.

In the spray development analyses, the results indicated structural formations differences between the inner and outer regions of the spray. In the first instants, the velocity field indicated the break of the recirculation structure and an acceleration of the air flow around the spray development. The initial instants of the spray development showed in the recirculation zone uprise velocities between 2 and 4 m/s. The gas phase had these structures due to the geometry of the injector inside the chamber, which a production of a quiescent environment and a particular vortical structure. The results were similar to spray development in quiescent environments at the beginning of the injection, as shown in simulation analysis. During the injection, the divergence on velocities were significantly reduced, and the velocity fluctuations were also reduced. These results match with turbulent intensity reduction found by (BERTI, 2018) at this stage of injection. The results also provided a horizontal component (defined as orthogonal to the center of the spray nozzle) of the vectors as an air drag between the internal cavities of the ethanol spray. At the end of injection, the spray drag was the most relevant structure found by PTV measurement. The air flow behind the spray moved into the center of the spray axis and followed the spray structure.

The PTV analysis proved to be a capable technique to investigate surrounded air around spray development. The main known characteristics of the air were reproduced with this technique. Important structures could be found, and new air movement were found. Until the present day, few PTV analysis for surrounded air of a spray was found. And the present work could add knowledge in two phase flow using PTV technique.

The peak locking results demonstrated the efficiency in the smooth curve fitting for obtaining the sub-pixel part of displacement. The histograms revealed no distortion in particle displacement, and the sub-pixel histograms indicated a near flat distribution between 0 and 1. With peak locking, the histogram would show higher values close to 0 or 1 pixel. Thus, the results for the PTV measurements presented minimal influence of the peak locking error.

6.1   Future works

For future works, the challenging boundary region between spray and air indicated that no complementary knowledge was added with PTV technique, thus a further measurement of this region with different experiment parameters could be capable of investigate such challenging region. Also, an improvement of the technique is to apply the PTV technique for 3D measurement using Shake-The-Box approach as an accurate tomo-

graphic particle tracking velocimetry. This approach could detail the tridimensionality of the spray event.

REFERENCES

AGUERA, N.; CAFIERO, G.; ASTARITA, T.; DISCETTI, S. Ensemble 3d ptv for high resolution turbulent statistics. **Measurement Science and Technology**, Institute of Physics Publishing, v. 27, 10 2016. ISSN 13616501.

ALEIFERIS, P. G.; SERRAS-PEREIRA, J.; ROMUNDE, Z. van; CAINE, J.; WIRTH, M. Mechanisms of spray formation and combustion from a multi-hole injector with e85 and gasoline. **Combustion and Flame**, The Combustion Institute., v. 157, p. 735–756, 2010. ISSN 00102180. Disponível em: <http://dx.doi.org/10.1016/j.combustflame.2009.12.019>.

ANFAVEA. Anuário da indústria automobilistica brasileira. 2018.

BAUMGARTEN, C. **Mixture Formation in Internal Combustion Engine**. [S.l.: s.n.], 2006.

BERESH, S. J.; HENFLING, J. F.; SPILLERS, R. W. "postage-stamp piv:" small velocity fields at 400 khz for turbulence spectra measurements. In: . [S.l.]: American Institute of Aeronautics and Astronautics Inc., 2017. ISBN 9781624104473.

BERTI, R. d. C. R. **Interaction of turbulent structures with ethanol sprays in mixture formation processes in a constant-flow chamber.** Tese (Doutorado) — Universidade de São Paulo, São Paulo, sep 2018. Disponível em: <http://www.teses.usp.br/teses/disponiveis/3/3150/tde-19092018-082453/>.

BOSCH, R. Gasoline direct injection - key technology for greater efficiency and dynamics. 2013. ISSN 0036-8075.

CHEN, J.; KATZ, J. Elimination of peak-locking error in piv analysis using the correlation mapping method. **Measurement Science and Technology**, Institute of Physics Publishing, v. 16, p. 1605–1618, 8 2005. ISSN 09570233.

COHN, R. K.; KOOCHESFAHANI, M. M. The accuracy of remapping irregularly spaced velocity data onto a regular grid and the computation of vorticity. **Experiments in Fluids**, v. 29, p. S061–S069, 12 2000. ISSN 0723-4864. Disponível em: <http://link.springer.com/10.1007/s003480070008>.

DABIRI, D.; PECORA, C. **Particle Tracking Velocimetry**. IOP Publishing, 2019. (2053-2563). ISBN 978-0-7503-2203-4. Disponível em: <https://dx.doi.org/10.1088/978-0-7503-2203-4>.

DELLENBACK, P. A.; MACHARIVILAKATHU, J.; PIERCE, S. R. **Contrast-enhancement techniques for particle-image velocimetry**. 2000.

DUNCAN, J.; DABIRI, D.; HOVE, J.; GHARIB, M. Universal outlier detection for particle image velocimetry (piv) and particle tracking velocimetry (ptv) data. **Measurement Science and Technology**, IOP Publishing, v. 21, p. 057002, 5 2010. ISSN 0957-0233.

FENG, Y.; GOREE, J.; LIU, B. Errors in particle tracking velocimetry with high-speed cameras. **Review of Scientific Instruments**, v. 82, n. 5, 2011. ISSN 00346748.

FUCHS, T.; HAIN, R.; KÄHLER, C. J. Non-iterative double-frame 2D/3D particle tracking velocimetry. **Experiments in Fluids**, Springer Berlin Heidelberg, v. 58, n. 9, p. 1–5, 2017. ISSN 07234864.

HASSAN, Y. A.; CANAAN, R. E. Full-field bubbly flow velocity measurements using a multiframe particle tracking technique. **Experiments in Fluids**, v. 12, n. 1-2, p. 49–60, 1991. ISSN 07234864.

HEYMAN, J. TracTrac: A fast multi-object tracking algorithm for motion estimation. **Computers and Geosciences**, v. 128, p. 11–18, 2019. ISSN 00983004.

HONKANEN, M.; NOBACH, H. Background extraction from double-frame PIV images. **Experiments in Fluids**, v. 38, n. 3, p. 348–362, 2005. ISSN 07234864.

JANKE, T.; SCHWARZE, R.; BAUER, K. Part2Track: A MATLAB package for double frame and time resolved Particle Tracking Velocimetry. **SoftwareX**, Elsevier B.V., v. 11, p. 100413, 2020. ISSN 23527110. Disponível em: <https://doi.org/10.1016/j.softx.2020.100413>.

JEDELSKY, J.; MALY, M.; CORRAL, N. P. del; WIGLEY, G.; JANACKOVA, L.; JICHA, M. Air–liquid interactions in a pressure-swirl spray. **International Journal of Heat and Mass Transfer**, Elsevier Ltd, v. 121, p. 788–804, 6 2018. ISSN 00179310.

KAHLER, C. J.; SCHARNOWSKI, S.; CIERPKA, C. On the resolution limit of digital particle image velocimetry. **Experiments in Fluids**, v. 52, p. 1629–1639, 6 2012. ISSN 0723-4864.

KIM, Y.; KIM, W. I.; MIN, B.; SEO, J.; LEE, K. Experimental investigation of combustion characteristics of ethanol–gasoline blended fuel in a t-gdi engine. **Applied Thermal Engineering**, Elsevier Ltd, v. 208, 2 2022. ISSN 13594311.

LACASSAGNE, T.; VATTEVILLE, J.; DEGOUET, C.; El Hajem, M.; SIMOËNS, S. PTV measurements of oscillating grid turbulence in water and polymer solutions. **Experiments in Fluids**, Springer Berlin Heidelberg, v. 61, n. 7, p. 1–15, 2020. ISSN 14321114. Disponível em: <https://doi.org/10.1007/s00348-020-03000-x>.

LEFEBVRE, A. H.; MCDONELL, V. G. **Atomization and Sprays**. Second edition. | Boca Raton : Taylor & Francis, CRC Press, 2017.: CRC Press, 2017. ISBN 9781315120911. Disponível em: <https://www.taylorfrancis.com/books/9781498736268>.

LEI, Y. C.; TIEN, W. H.; DUNCAN, J.; PAUL, M.; PONCHAUT, N.; MOUTON, C.; DABIRI, D.; RÖSGEN, T.; HOVE, J. A vision-based hybrid particle tracking velocimetry (PTV) technique using a modified cascade correlation peak-finding method. **Experiments in Fluids**, v. 53, n. 5, p. 1251–1268, 2012. ISSN 07234864.

LIGHTFOOT, M. Fundamental classification of atomization processes. **Atomization and Sprays**, v. 19, p. 1065–1104, 2009. ISSN 1044-5110. Disponível em: <http://www.dl.begellhouse.com/journals/6a7c7e10642258cc,08fc39f53290f6f4,1d5bd05245c89850.html>.

MEI, R. Flow due to an oscillating sphere and an expression for unsteady drag on the sphere at finite reynolds number. **Journal of Fluid Mechanics**, v. 270, p. 133–174, **7** 1994. ISSN 0022-1120. Disponível em: <https://www.cambridge.org/core/product/identifier/S0022112094004222/type/journal_article>.

MELLING, A. **Tracer particles and seeding for particle image velocimetry**. 1997. 1406-1416 p.

MOURA, H. **Análise da qualidade de medidas F-PIV e da fluidodinâmica em coluna de bolhas utilizando invariantes caóticos**. Tese (Doutorado) — Universidade Estadual de Campinas, Campinas, jun 2017. Disponível em: <http://acervus.unicamp.br/index.asp?codigo_sophia=987553>.

OHMI, K.; LI, H.-Y. **Particle-tracking velocimetry with new algorithms**. 2000. 603-616 p. Disponível em: <http://iopscience.iop.org/0957-0233/11/6/303>.

PATEL, M.; LEGGETT, S. E.; LANDAUER, A. K.; WONG, I. Y.; FRANCK, C. Rapid, topology-based particle tracking for high-resolution measurements of large complex 3D motion fields. **Scientific Reports**, Springer US, v. 8, n. 1, p. 1–14, 2018. ISSN 20452322. Disponível em: <http://dx.doi.org/10.1038/s41598-018-23488-y>.

PECORA, C.
Particle Tracking Velocimetry: A Review, 2018.

QI, G. Q.; NATHAN, G. J.; KELSO, R. M. Ptv measurement of drag coefficient of fibrous particles with large aspect ratio. **Powder Technology**, Elsevier B.V., v. 229, p. 261–269, 2012. ISSN 1873328X.

RAFFEL, M.; WILLERT, C. E.; SCARANO, F.; KäHLER, C. J.; WERELEY, S. T.; KOMPENHANS, J. **Particle Image Velocimetry A Practical Guide Third Edition**. [S.l.: s.n.], 2018.

RAFFEL, M.; WILLERT, C. E.; WERELEY, S. T.; KOMPENHANS, J. **Particle Image Velocimetry**. Berlin, Heidelberg: Springer Berlin Heidelberg, 2007. ISBN 978-3-540-72307-3. Disponível em: <http://link.springer.com/10.1007/978-3-540-72308-0>.

RAYLEIGH, L. On the stability, or instability, of certain fluid motions. **Proceedings of the London Mathematical Society**, s1-11, p. 57–72, 11 1879. ISSN 1460244X. Disponível em: <http://doi.wiley.com/10.1112/plms/s1-11.1.57>.

SANTOS, A. S.; GILIO, L.; HALMENSCHLAGER, V.; DINIZ, T. B.; ALMEIDA, A. N. Flexible-fuel automobiles and CO2 emissions in Brazil: Parametric and semiparametric analysis using panel data. **Habitat International**, Elsevier, v. 71, n. November 2017, p. 147–155, 2018. ISSN 01973975. Disponível em: <https://doi.org/10.1016/j.habitatint.2017.11.014>.

SCHANZ, D.; SCHRöDER, A.; GESEMANN, S.; MICHAELIS, D.; WIENEKE, B. **'Shake The Box': A highly efficient and accurate Tomographic Particle Tracking Velocimetry (TOMO-PTV) method using prediction of particle positions**. 2013. 1-13 p.

SCHARNOWSKI, S.; BROSS, M.; KäHLER, C. J. Accurate turbulence level estimations using piv/ptv. **Experiments in Fluids**, Springer Verlag, v. 60, 1 2019. ISSN 07234864.

SHAVIT, U.; LOWE, R. J.; STEINBUCK, J. V. Intensity capping: A simple method to improve cross-correlation piv results. **Experiments in Fluids**, v. 42, p. 225–240, 2 2007. ISSN 07234864.

SOLOMON, C.; BRECKON, T. **Fundamentals of Digital Image Processing: A practical approach with examples in Matlab**. [S.l.]: John Wiley & Sons, 2011.

STIEHL, R.; SCHORR, J.; KRüGER, C.; DREIZLER, A.; BöHM, B. In-cylinder flow and fuel spray interactions in a stratified spray-guided gasoline engine investigated by high-speed laser imaging techniques. In: . [S.l.: s.n.], 2013. v. 91, p. 431–450. ISSN 13866184.

TANG, T.; DENIZ, E.; KHOKHA, M. K.; TAGARE, H. D. Gaussian process post-processing for particle tracking velocimetry. **Biomedical Optics Express**, The Optical Society, v. 10, p. 3196, 7 2019. ISSN 2156-7085.

TEIXEIRA, M. **U.S., Brazil see room for global ethanol growth before transition to EVs**. 2020. Disponível em: <https://br.reuters.com/article/us-ethanol-outlook-emissions/u-s-brazil-see-room-for-global-ethanol-growth-before-transition-to-evs-idUKKBN27F2JU>.

TODARO, R. H. **Otimização de medidas PIV na interação de um spray de etanol com o ar circundante em uma câmara de fluxo contínuo**. 2020.

TODARO, R. H.; PACÍFICO, A. L.; AMARAL, R. D. L.; KRIEGER, C. G. F. OPTIMIZATION OF PIV PROCESSING IN THE INVESTIGATION OF AN ISOTHERMAL ETHANOL SPRAY CHAMBER. **Brazilian Congress of Thermal Sciences and Engineering**, 2020.

WESTERWEEL, J.; ELSINGA, G. E.; ADRIAN, R. J. Particle Image Velocimetry for Complex and Turbulent Flows. **Annual Review of Fluid Mechanics**, v. 45, n. 1, p. 409–436, 2013. ISSN 0066-4189.

WESTERWEEL, J.; SCARANO, F. Universal outlier detection for piv data. **Experiments in Fluids**, v. 39, p. 1096–1100, 2005. ISSN 07234864.

WIERZBA, A. **Experiments in Fluids Deformation and breakup of liquid drops in at nearly critical Weber numbers**. 1993. 59-64 p.

YAMAMOTO, F.; UEMURA, T.; TIAN, Z. H.; OHMI, K. Three-Dimensional PTV Based on Binary Cross-Correlation Method. Algorithm of Particle Identification. **JSME International Journal Series B**, v. 36, n. 2, p. 279–284, 1993. ISSN 1340-8054. Disponível em: <http://www.mendeley.com/research/ geology-volcanic-history-eruptive-style-yakedake-volcano-group-central-japan/http: //www.jstage.jst.go.jp/article/jsmeb1993/36/2/36_2_279/_article>.

YAN, J.; CHOU, S. K.; CHEN, B.; SUN, F.; JIA, H.; YANG, J. Clean, affordable and reliable energy systems for low carbon city transition. **Applied Energy**, v. 194, p. 305–309, 2017. ISSN 03062619.

YANG, B.; WANG, Y.; LIU, J. Piv measurements of two phase velocity fields in aeolian sediment transport using fluorescent tracer particles. **Measurement: Journal of the International Measurement Confederation**, v. 44, p. 708–716, 5 2011. ISSN 02632241.

YEOM, J. Diagnosis of the behavior characteristics of the evaporative diesel spray by using images analysis. **Journal of Mechanical Science and Technology**, v. 22, p. 1785–1792, 9 2008. ISSN 1738494X.

ZABEU, C. B.

Investigações de estratégias de injeção e ignição de etanol em câmara de combustão de volume constante., 4 2019. Disponível em: <http://www.teses.usp.br/teses/disponiveis/3/3150/tde-31012019-072349/>.

ZHANG, M.; XU, M.; HUNG, D. L. Simultaneous two-phase flow measurement of spray mixing process by means of high-speed two-color piv. **Measurement Science and Technology**, v. 25, 2014. ISSN 13616501.